

ABSTRACT

DILWITH, JASON ROBERT. Feasibility Study of Laser Ablation using Long Pulsed 300W, CW Single Mode Fiber Laser. (Under the direction of Dr. Juei-Feng Tu)

Many applications now require micro sized holes that are difficult to produce with conventional methods. The entrance of lasers in the industry has brought about a better method for producing these holes. However the ultra-short pulse lasers that are normally used are extremely expensive and require many pulses to remove the material due to the small amount of energy they deposit. The objective of this research is to examine the feasibility of laser ablation using a 300W, CW Single Mode fiber laser which has high continuous power output for each pulse and has excellent beam quality. The results show that laser ablation occurs when a 100mm lens is used with pulse durations at 40 μ s or below. Using one 18 μ s pulse, a blind hole of 43.6 μ m in diameter and 23.6 μ m in depth with an aspect ratio of 0.54 can be created with little heat affected zone. This performance is comparable to nanosecond lasers, but with much higher hole depth per pulse. It was also found that the pulse duration must be short enough so that the ablating effect of the initial spike of an enhanced pulse is not nullified due to melting. At longer pulse durations (50 μ s or more), raised surfaces are created instead of holes.

**FEASIBILITY STUDY OF LASER ABLATION USING LONG PULSED 300W,
CW SINGLE MODE FIBER LASER**

by

JASON ROBERT DILWITH

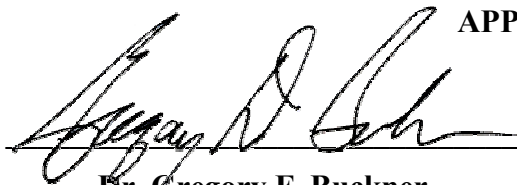
**A thesis submitted to the Graduate Faculty of
North Carolina State University
in partial fulfillment of the
requirements for the Degree of
Master of Science**

MECHANICAL AND AEROSPACE ENGINEERING

Raleigh, NC

2005

APPROVED BY:



Dr. Gregory F. Buckner
Advisory Committee Member



Dr. Eric C. Klang
Advisory Committee Member



5-19-2005

Dr. Juei F. Tu
Advisory Committee Chairman

I dedicate this to all the people who have helped me on the way including family and friends as I would not be the person today nor have accomplished the things I have if it wasn't for you.

Biography

Jason Dilwith was born in Albany, NY and grew up in the town of Ravena 10 miles south of the capitol. He enrolled in the Hudson Valley Community College Engineering Science program where he studied for two years. He then transferred into the Mechanical Engineering program at NC State University. In May of 2003 he earned his Bachelors degree and then enrolled into the Masters Mechanical Engineering program. After his first semester he joined the laser research group of Dr. J. Tu. In May 2005 Jason earned his MSME degree at NC State University and will move on to a mechanical engineering position he has accepted in NY with Tyco Healthcare.

ACKNOWLEDGEMENTS

I'd like to thank all of the people who have helped me throughout my research. In particular I would like to thank Dr. Tu for his guidance and especially his patience as he was a tremendous help during the process. I would like to thank my committee members, Dr. Buckner, Dr. Klang, and Dr. Ramasubramanian, for taking time out of their days to review my thesis and attend my defense where they gave good suggestions on how to better the presentation and thesis. I would also like to thank Dr. Ramasubramanian for the use of his digital oscilloscope that was critical for troubleshooting and obtaining the results for my research. I am extremely grateful for research colleagues, Ryan Dennis, Ray Harp, Alex Paleocrassas, Alex York, and S.J. Park, since they were an integral part of the research process and have helped me throughout it. Obtaining the profile data for my tested specimens would not have been possible without the help of Kara Folkert and the Precision Engineering Center to whom I owe much thanks to. I appreciate the help and suggestions from Mike Breedlove, and Skip Richardson, who helped me to prepare my specimens for testing. I'd also like to thank Jessica Brouker as she was incredibly supportive during my research and has helped me recognize all of the grammatical errors in my writing. I simply could not have done it without the help of these people.

Table of Contents

LIST OF FIGURES	vii
LIST OF TABLES	x
1 INTRODUCTION	1
2 PROBLEM STATEMENT	2
3 HYPOTHESIS	3
4 LITERATURE	4
4.1 Drilling Methods.....	4
4.2 Laser Parameters.....	6
4.3 Laser Ablation	9
4.4 Hole Characteristics.....	11
4.5 Theoretical Ablation Models	12
4.6 Experimental Papers.....	13
5 INITIAL FEASIBILITY CHECK	21
6 SPECIFIC RESEARCH PROBLEMS	23
7 APPROACHES	24
8 EXPERIMENTAL APPARATUS.....	25
9 EXPERIMENTAL PROCEDURE	33
10 RESULTS AND DISCUSSION.....	36
10.1 Initial Focal Tests	36
10.2 Relocation Focal Tests.....	39
10.3 100mm Lens Tests.....	44
10.4 20 μ s, 30 μ s, and 40 μ s Pulse Width Tests.....	47
10.5 Sub 20 μ s Pulse Tests	61
10.6 Results comparison.....	68
10.7 Benchmark Revisited.....	69
11 CONCLUSIONS.....	70
12 FUTURE WORK.....	71
13 REFERENCES	73
14 APPENDICES	77
14.1 Connecting Gemini Servo Drives, Linear Motors and PCI Motion Controller	77
14.2 Equipment Connection Images.....	85
14.3 Laser Images and Procedure.....	87
14.4 Laser Alignment Procedure	89

14.5	Simulink Models.....	91
14.6	Example DMC Script	97
14.7	Microscope Operation & Details	98
14.8	Zygo NewView 5000 Interferometric Microscope Details.....	100
14.9	Talysurf Stylus Profilometer Details	102
14.10	External Pulse Generator	103

LIST OF FIGURES

Figure 4.1: Statistics for laser systems.....	5
Figure 4.2: Reflectivity as a function of wavelength for several metals	6
Figure 4.3: Power modes of optical beams.....	7
Figure 4.4: Various Beam Modes	8
Figure 4.5: Gaussian Beam.....	8
Figure 4.6: Gaussian Beam Top View	8
Figure 4.7: Beam Qualities for Various Lasers	9
Figure 4.8: Diagram of Thermal Ablation	10
Figure 4.9: Schematic diagram of the vaporized plume	10
Figure 4.10: Side profile of a percussion drilled hole or “keyhole”	12
Figure 4.11 Schematic illustrating f.p.p.....	13
Figure 4.12: Diagram of parameters effect on the hole entrance diameter.....	15
Figure 4.13: Diagram of parameters effect on the hole taper	15
Figure 4.14: Diagram of parameters effect on hole circularity.....	16
Figure 4.15: Rene80 experiment-parameter effects plot.....	17
Figure 4.16: Typical optical micrographs of laser drilled array holes.....	18
Figure 4.17: Typical optical micrographs of spatter-free laser drilled array holes.....	18
Figure 4.18: SEM surface micrographs of laser drilled holes in ASCC coated alloy	18
Figure 4.19: Variation of entrance geometry of laser percussion drilled holes	19
Figure 4.20: Exit hole diameters as a function of material thickness	20
Figure 5.1: Estimated Enhanced pulse for Fiber Laser.....	21
Figure 7.1: Exit hole diameters as a function of material	24
Figure 8.1: Experimental Setup	25
Figure 8.2: Collimator.....	26
Figure 8.3: Optics Assembly.....	26
Figure 8.4: Assist gas nozzle	27
Figure 8.5: Solenoid valve	27
Figure 8.6: DMC Terminal	28

Figure 8.8: Simulink Model.....	29
Figure 8.9: Transport Delay Settings.....	30
Figure 8.10: Tektronix Oscilloscope.....	30
Figure 8.11: Oscilloscope Connection.....	31
Figure 8.12: 20 μ s Pulse	31
Figure 8.13: Zeiss Inverted Microscope	32
Figure 9.1: Focusing Test	33
Figure 9.2: 40mm posts.....	34
Figure 10.1: Hole created from 1ms pulse.....	36
Figure 10.2: Plot of Focus Test #1 Results.....	37
Figure 10.3: Undesired melting at non-focused position.....	37
Figure 10.4: Undesired surface at non-focused position	37
Figure 10.5: Holes created from varying pulse widths.....	38
Figure 10.6: Holes created from 50 μ s pulse after relocation.....	39
Figure 10.7: Refined focal test using 50 μ s pulse (after relocation).....	40
Figure 10.8: Zygo measurements of hole at 8.7mm focal position	41
Figure 10.9: Zygo measurements of hole at 8.9 mm focal position	42
Figure 10.10: Zygo measurements of hole at 9.1 mm focal position	43
Figure 10.11: Focusing test using new 100mm lens.....	44
Figure 10.12: Spot radius as a function of focusing depth for 150mm lens	45
Figure 10.13: Spot radius as a function of focusing depth	46
Figure 10.14: Spot Diameter as a function of focusing depth for 100mm lens.....	48
Figure 10.15: Spot images for 20 μ s test.....	49
Figure 10.16: Enlarged hole image for 20 μ s test , 40X objective.....	50
Figure 10.17: Zygo hole profile data for 20 μ s pulse width	51
Figure 10.18: Talysurf surface profile for 20 μ s pulse width hole	52
Figure 10.19: Spot images for 30 μ s test.....	53
Figure 10.20: Enlarged hole image for 30 μ s test, 40X objective	54
Figure 10.21: Zygo hole profile data for 30 μ s pulse width	55
Figure 10.22: Talysurf hole profile for 30 μ s pulse width.....	56
Figure 10.23: Spot images for 40 μ s test.....	57

Figure 10.24: Enlarged hole image for 40 μ s test, 40X objective	58
Figure 10.25: Zygo hole profile data for 40 μ s pulse width	58
Figure 10.26: Enhanced Pulse Analysis.....	59
Figure 10.27: Hole Characteristics Diagram for Various Pulse Width Tests.....	60
Figure 10.28: Enlarged Images for Sub 20ms Pulses	61
Figure 10.29: Depth Measurement for 20 μ s Pulse Test	62
Figure 10.30: 19 μ s Pulse	63
Figure 10.31: 18 μ s Pulse Results.....	63
Figure 10.32: 17 μ s Pulse	64
Figure 10.33: 16 μ s Pulse Results.....	64
Figure 10.34: Depth Measurement for 15 μ s Pulse Test	65
Figure 10.35: Plot of Hole Characteristics for Various Pulse Widths	66
Figure 10.36: Original Form of Enhanced Pulse	67
Figure 10.37: Predicted Form of Enhanced Pulse from Experimentation.....	67

LIST OF TABLES

Table 4.1: Drilling methods and parameters.....	4
Table 5.1: Typical Laser Parameters	22
Table 10.1: Summary of Initial Focal Tests.....	38
Table 10.2: Summary of successfully drilled holes	59
Table 10.3: Typical parameters for different laser systems	68

1 INTRODUCTION

Pushing the limits of technology, such as making devices faster, smaller, or lighter, has brought about many needs, one being the production of smaller accurate arrays of holes in various materials. This demand has been brought about by a variety of useful applications such as automotive fuel injectors, chemical and textile processing nozzles, medical needles, etc. (Feifer, 1989) One of the most prominent examples would be in the aerospace field where cooling holes need to be formed for nozzle guide vanes, combustion rings and engine blades.

There are many methods for drilling holes in materials. Some of which are completely mechanical, some are non-mechanical, and others can be a hybrid between the two.

Research in laser drilling has become a point of interest; in particular ultra-short pulsed lasers have been the main tool for laser micro drilling applications. However, ultra-short pulse lasers can only provide very little energy output, typically less than 10 J/cm^2 .

Therefore each pulse can only remove a very small amount of material, usually only a few nanometers. Due to the fact that the repetition rates of these lasers are limited, on average less than 10 kHz, the productivity is low. The shortcomings of these types of lasers leads to the research of new methods with improved performance.

2 PROBLEM STATEMENT

Conventionally, laser systems tend to be application specific. For example, kW CW high power lasers are used for high speed welding while ultra-short pulse lasers are used for laser ablation. It is therefore desirable to explore the feasibility of laser ablation using a 300W, CW single-mode fiber laser designed for macro cutting and welding to extend its processing capabilities.

3 HYPOTHESIS

Using a 300W, single-mode fiber laser, various materials can be drilled to provide micro holes with higher aspect ratios. This can be achieved by 1) focusing the laser beam to a very small spot size as a direct result of the high beam quality the fiber laser possesses. 2) Utilizing the higher output power due to the initial spike of a modulated pulse.

4 LITERATURE

Drilling at extremely small scales is used in a variety of applications from cooling holes in turbines to applications in the biomedical field. (Ready, 1997) For example the cooling of turbine blades is a very important area since the demand for higher efficiency turbines are growing which leads to the need for higher inlet temperatures. These higher temperatures require extra cooling in the blades to keep them within safety standards. Creating arrays of extremely small holes can help increase the heat transfer from the blades to provide greater longevity for the turbines. Another example where extremely small holes are needed is in the biomedical field for producing smaller needles that can be used in various applications where larger needles would be obtrusive. The automobile industry is another large field in which small precise holes are needed for devices such as fuel injectors. Some other applications which present a need for fast accurate drilling are inkjet printers, pcb manufacturing, and controlled leaks.

4.1 Drilling Methods

There are various ways to go about, and produce these desired holes. Some of the most common devices used for drilling applications are listed in the table below:

Name	Minimum Hole Diameter	Speed	Method	Maximum Aspect Ratio
ECD	0.40mm	Medium	Non-mechanical	200
ECM	0.50mm	Medium	Non-mechanical	80
EDM	0.02mm	Slow	Non-mechanical	100
Laser	<0.01mm	Fast	Non-mechanical	200 (50*)
Mechanical (Bits)	~1mm	Slow	Mechanical	120
Water-jet	~1.5mm	~Fast	**Mechanical	25

**applies direct pressure to material (Tu, 1999)

Table 4.1: Drilling methods and parameters

From looking at the table above it can be seen that mechanical methods are greatly limited in the size of the hole they can produce. Coupled with this fact and other disadvantages of mechanical processes, they will not meet the requirements for the applications needed. Mechanical drilling's main disadvantage is "tool wear" and its lack of speed. After a certain number of cycles the mechanical goes through, the "bits" must be replaced either from them being broken or due to them being dulled and will not

effectively cut anymore. In the case of Water-Jet drilling, the process is fast, but can not produce as small holes as the other applications. Both of these mechanical processes exhibit unwanted stress on material since their method of removal is by force, this can lead to other types of defects in the material. Electrochemical machine (ECM), and electrochemical drilling (ECD) do not provide fast processing times and do not have the capability to produce small diameter holes. Electro-discharge machine produces smaller holes than its counterparts, but has a very slow processing time, and therefore will be disregarded. A common problem between all of the electrical techniques is that to achieve the temperatures needed for material removal of such small holes, requires the electrodes to have high amperage pass through them which often leads to the electrodes constantly having to be replaced, thus limiting the minimum hole diameter that they can achieve. Therefore laser drilling appears to be the most promising method for the drilling applications needed since it is non-mechanical, can drill extremely small holes, and has a fast processing time. As can be see in figure 4.1 there are many types of lasers used in machining materials, though there are two many types of lasers commonly used, that of CO₂ lasers and Nd:YAG lasers. Usually, because of their wavelengths and other properties, Nd:YAG lasers are used to drill metals while CO₂ lasers are used to drill non-metals.

Lasers	Wavelength (μm)	Operating regimes	Typical applications
CO ₂	10.6	Continuous, pulsed, TEA	Welding, drilling, heat treating
Nd:YAG	1.06, 0.532	Continuous, pulsed	Welding, drilling, trimming, marking
Ruby	0.6943	Pulsed	Spot welding, drilling
Nd:glass	1.06	Pulsed	Spot welding, drilling
Alexandrite	0.72–0.78	Pulsed	Drilling
Copper vapor	0.511, 0.578	Pulsed	Drilling
Excimer	0.249	Pulsed	Micromachining, ablation, semiconductor processing
Argon	0.488, 0.5145	Continuous	Semiconductor processing

Figure 4.1: Statistics for laser systems (Ready, 1997)

One of these factors is reflectivity which has a large impact in how much energy is absorbed by the material. As shown in the chart below, the operating wavelength of a CO₂ laser is at 10.6μm which is towards the peak reflectivity for the various metals.

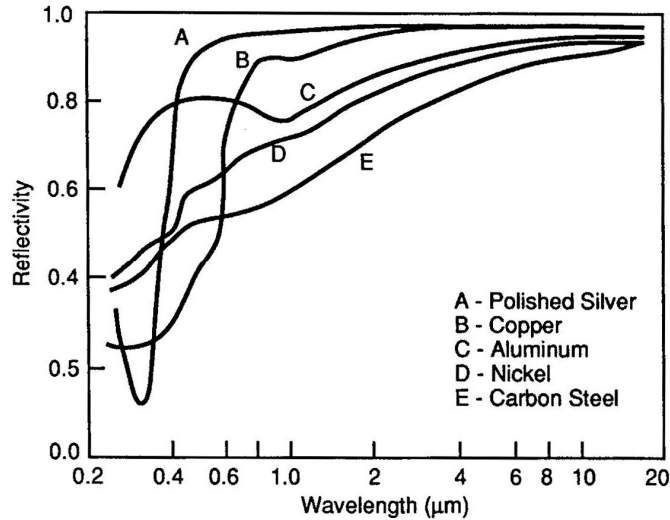


Figure 4.2: Reflectivity as a function of wavelength for several metals. (Ready, 1997)

However it can be seen that at 1.06μm, the operating wavelength of a Nd:YAG laser, the reflectivity for some metals drops considerably. To better demonstrate this phenomenon, steel will absorb about 10% of the light from a CO₂ laser, but will absorb around 40% from a Nd:YAG laser.

The lasers that are the main point of interest in laser drilling research are referred to as “ultra-short pulse” lasers. These lasers compress the laser into pulses with extremely small duration and high peak powers. Though these lasers provide great benefits over conventional methods, they still contain downsides that may be improved upon.

4.2 Laser Parameters

4.2.1 Operation States

To gain a better understanding of laser drilling, the general process and characteristics of lasers can now be discussed. First, the drilling process can be carried out through two main types of laser operation modes, continuous or pulsed. (Charschan, 1993) The continuous mode (CW) is when the laser is held at a constant output over a specified length of time as shown in figure 4.3, while the pulsed modes can be split up into different categories.

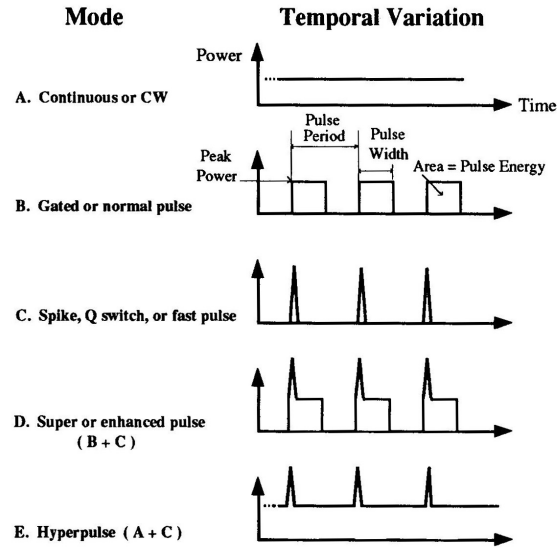


Figure 4.3: Power modes of optical beams (Charschan, 1993)

The normal pulse mode is defined as the time variation of power achieved by simple modulation of the excitation power to the active medium or by the external attenuation of a CW beam. A normal pulse denotes the same type of output power for a pulse-only laser, and its peak power can be significantly larger. A Q-switched pulse denotes a short-duration, high-peak-power pulse. It is obtained by storing energy in the active medium and releasing it by means of fast optical switching inside the resonator. An enhanced pulse is the combination of a high-power spike pulse on the leading edge of a normal pulse while the hyperpulse is the combination of a train of power spike pulses superimposed on a CW beam.

4.2.2 Beam modes

Other characteristics of a laser besides its operation state also affect the ability to process materials. One very important aspect is the beam mode of the laser. Beam modes are expressed by a TEM_{xy} number. The xy value describes the number of gaps within the cross section of the beam. Figure 4.4 shows some examples of beam modes where the TEM_{00} mode is called “single mode”. The higher the order of the mode the more difficult it is to focus due to the beam no longer coming from a virtual point. (Steen, 2003) Therefore single mode provides the greatest focusability and would be the best choice for laser drilling since small round holes are the objective.



Figure 4.4: Various Beam Modes (Ready, 1997)

4.2.3 Beam Profile

The beam profile of a laser is how the power is distributed over the beam. The Gaussian beam profile shown in figure 4.5 is derived from the mathematically calculated Gaussian curve. A Gaussian profile has the highest power density located at the center of the beam. This provides better focusing whereas the higher power density at the center of the beam allows for smaller holes to be created.

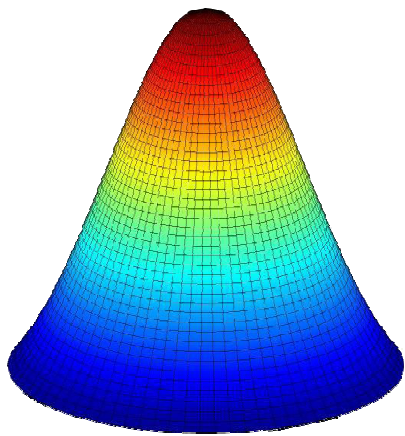


Figure 4.5: Gaussian Beam (Dennis, 2003)

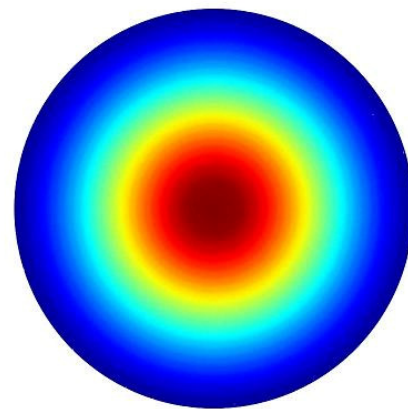


Figure 4.6: Gaussian Beam Top View (Dennis, 2003)

Finally the beam quality also plays a significant role in the ability to process materials. The beam quality is a measure of how close the beam profile is to a Gaussian profile or more specifically how close their divergences are. A perfect Gaussian beam has a beam quality of $M^2 = 1.0$. The beam quality directly affects the focusability of the laser beam. For instance a laser with a low beam quality, say $M^2 = 20$, would not be able to achieve nearly as small of a diameter as a laser with a beam quality of $M^2 = 1.1$. Figure

4.7 shows a plot of beam qualities for various lasers. As can be seen from the plot the Lamp and Diode Pumped lasers have much higher beam qualities than that of the 300W fiber laser used in this research.

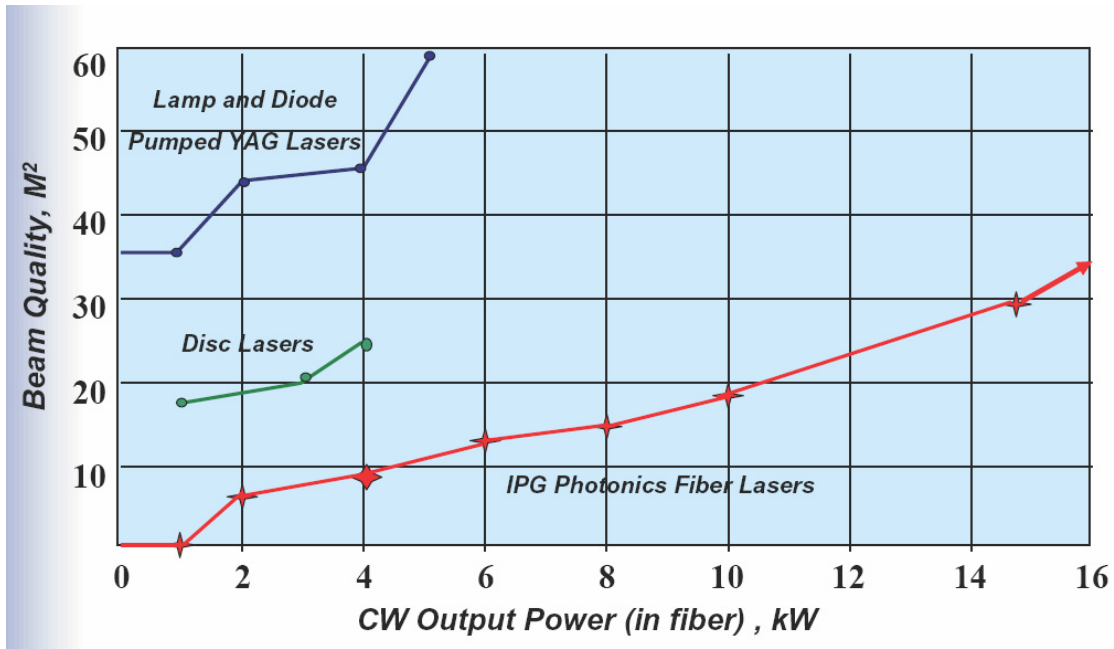


Figure 4.7: Beam Qualities for Various Lasers (IPG)

4.3 Laser Ablation

4.3.1 Thermal Ablation

Laser drilling is accomplished by the mechanism of ablation. There are two main categories of laser ablation. The first is thermal ablation in which the laser interacts with the surface of the specimen creating a heated area. This creates a molten pool of metal which with time expands into a “keyhole.” As the molten pool is continually irradiated part of the molten material then vaporizes and if hot enough, forms opaque plasma (or ionized gas). (Charschan, 1993) The exiting vapor then creates a recoil pressure which pushes the melt radially outward from the center of the beam as shown in figure 4.8.

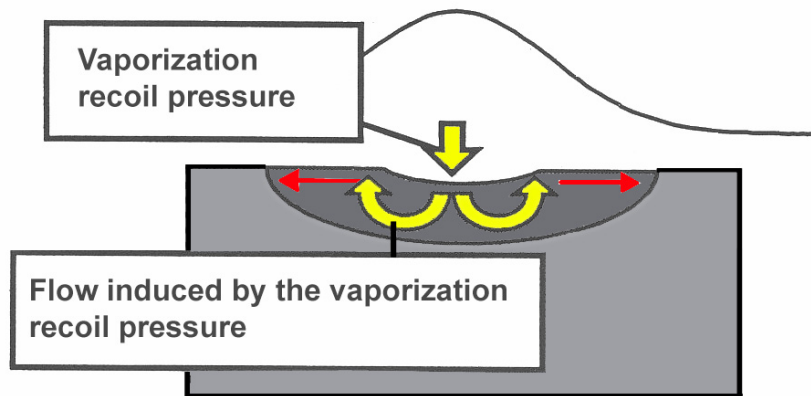


Figure 4.8: Diagram of Thermal Ablation (Murayama et al., 1998)

As seen in the figure an indentation in the material is created from the melt moving outward. After the laser pulse is completed the melted material will cool and some will solidify on perimeter of the indentation. This is referred to as a recast layer show in figure 4.10. Cooling of the vaporized plume can also contribute to the recast layer however most of the vaporized metal is carried away by an inert assist gas. A simple diagram of the vaporized plume caused by ablation is shown below in figure 4.9.

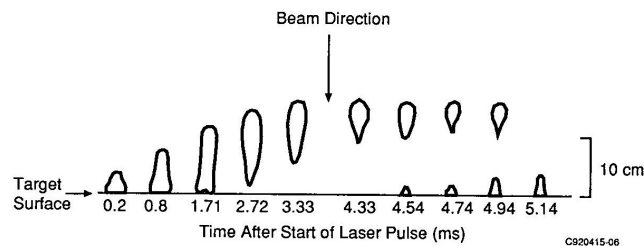


Figure 4.9: Schematic diagram of the vaporized plume of material formed by a high power carbon dioxide laser beam focused on an aluminum alloy. (Charschan, 1993)

The plume of vaporized metal and plasma is also blown away because the plasma will absorb the laser, therefore shielding it from the specimen's surface. Blowing this away will allow the laser to have a greater effect on the material.

4.3.2 Non-thermal Ablation

The second category of laser ablation is non-thermal or "cold" ablation. Non-thermal ablation is indicative of extremely small pulse times, usually between 10^{-11} to 10^{-12} seconds and smaller. The short pulse time is small enough to prevent heat conduction through the material, thus no melting occurs. Instead the laser interaction results in direct

bond breaking. Since no melting occurs there is no recast layer and little to no heat affected zone. (Steen, 2003)

4.3.3 Ablation Parameters

Though there are many facets that must be considered to promote ablation there are 3 main factors when considering ultra-short pulse lasers. The first is peak power density or peak power per unit area, measured in W/cm^2 . Having a high enough peak power density will allow for ablation to occur. Typically the peak power density is in the GW/cm^2 range. The pulse duration also has a considerable impact on the ability to cause ablation. Ultra-short pulse lasers have a fixed amount of energy they can deliver per pulse. Therefore if the pulse duration is lengthened the peak power produced will be significantly less. Commonly short-pulse lasers use pulse durations in the nanosecond, picosecond and femtosecond ranges. Lastly the repetition rate of the laser will control the production rate for producing holes. Having a low repetition rate will increase the time needed for producing the desired hole depths. A low repetition rate will also allow for all of the heat not used for ablation to leave the ablation zone and allow for cooling. If the repetition rate is high enough the heat can be retained and the ablation will be more efficient. (Friedrich, 1998)

4.4 Hole Characteristics

There are three general methods for drilling holes with lasers: percussion, trepanning, and helical drilling. (Tu, 1999) Percussion drilling is when the focal spot remains fixed which is used to drill the smallest of holes possible. Trepanning is used to drill holes larger than the spot size of the laser by rotating the focal spot into a circular path where breakthrough to the other side of the material is reached in one revolution. Very similar to trepanning, helical drilling does the same, but uses several revolutions to achieve breakthrough. A diagram of the basic geometry is shown in figure 4.10 below using a percussion method.

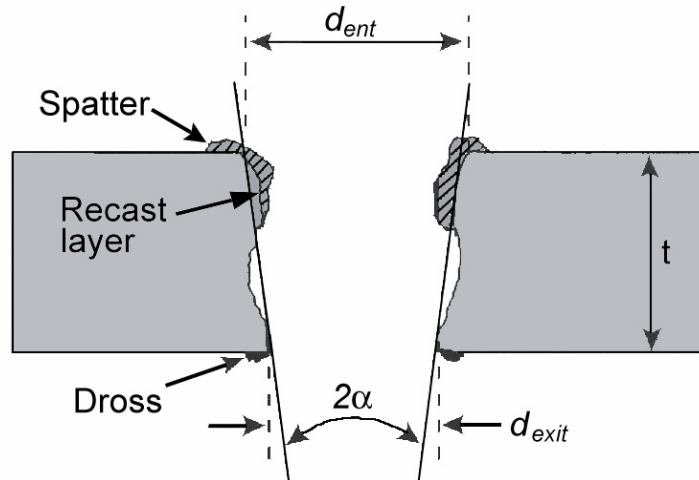


Figure 4.10: Side profile of a percussion drilled hole or “keyhole” (Tu, 1999)

Holes associated with laser drilling are commonly labeled into general categories. A Bore is considered to be greater than 25.4 mm in diameter, while a large hole is 12.7-25.4 mm, a small hole is 1.0-3.2 mm and a micro hole is less than 1.0 mm in diameter. (Tu, 1999) Scales are also a common way of referring to certain types of hole sizes such as: macro-scale being greater than 1mm, meso-scale between 0.1mm and 1mm, micro-scale between 0.1 μ m to 100 μ m and nano-scale being between 0.1nm to 100nm. (Crafer, 1993) Most research reviewed in this paper will refer to the micro-scale or below since these are the scales at which provide the most difficulty for the current conventional methods of drilling.

4.5 *Theoretical Ablation Models*

Many years have been spent modeling laser ablation from the most simple 2D heat transfer models to the very complicated molecular dynamic models. Since time is very limited for this research only an experimental approach will be undertaken as no improvements on these models would be possible. However these papers were reviewed to gain a better understanding of process parameters and to compare future work with these simulations. The work of (Murayama et al, 1998) assumes a Gaussian distribution to produce the temperature and velocity profiles within the molten pool. With this they are able to determine at what time vaporization begins and ends and to track the movement of the molten material. Other models aim at determining the drilling velocity

and drilling depth. One particular model looks at the mechanics within the hole to determine these values for long pulsed (100 μ s) lasers. (Zweig, 1991) Another study by (Ohmura et al, 1996) uses molecular dynamics to track the atomic behavior during laser ablation. With this model a better understanding of the individual steps can be achieved as well as predicting the trajectories for the vaporized atoms.

4.6 *Experimental Papers*

To further explore the capabilities of laser drilling reviews were made of research that has already been conducted in the matter. This will allow new techniques to be performed without redundancy. Two of the most important characteristics that must be examined in laser percussion drilling are hole taper and circularity (i.e. the roundness of the hole). A study was performed to determine the relationship between six controllable variables on these two factors. (Ghoreishi *et al*, 2002) The variables were laser peak power, laser pulse width, pulse frequency, number of pulses, assist gas pressure and focal plane position. To reduce the complexity and number of experiments required to properly test the parameters, a central composite design (CCD) in conjunction with response surface method (RSM) were used to analyze the system. Comparisons were made between 304 stainless steel and mild steel drilled with a 400 W pulsed Nd:YAG laser emitting at 1.06 μ m. CCD was used so that each variable did not have to be individually tested to see its effects on the system and it was also used to determine interaction effects between independent variables. One of the variables, focal plane position (f.p.p) was considered zero when it was set on the material's surface and positive and negative above and below the surface as shown in figure 4.11.

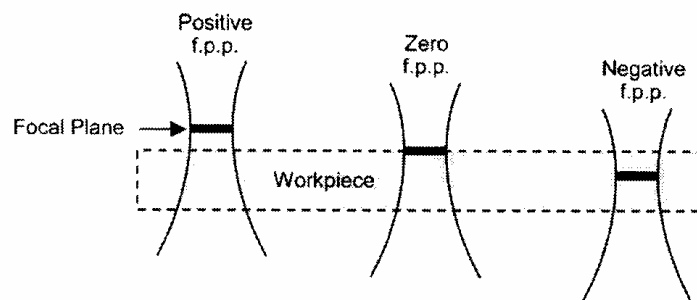


Figure 4.11: Schematic illustrating f.p.p. (Ghoreishi et al, 2002)

The equivalent entrance diameter, taper and ratio of minimum to maximum Feret's diameter were selected as outputs in order to analyze the process performance. (Where the Feret's diameter is the distance between two tangents on opposite sides of the hole, parallel to some fixed direction) The first response can be considered as nominal hole diameter, the second taper, with the third being circularity. Minimum and maximum diameters were experimentally measure for each hole in 3° steps. Spatter on top of the material was removed by abrasive blasting to insure accurate results during image processing without presenting any damage to the hole characteristics. In the case of hole entrance diameter it was found that the laser peak power and laser pulse width had the most significant effect on the model and increasing either would increase the entrance diameter. It was also determined that there were several interaction effects between the remaining variable. For instance with a positive f.p.p., increasing the assist gas pressure and number of pulses produced smaller holes while again increasing assist gas pressure, but decreasing the pulse frequency would also produce smaller holes. Considering all the results it was determined that at a lower peak power, shorter pulse width, positive f.p.p., higher assist gas pressure, larger number of pulses and lower pulse frequency produces smaller hole entrance diameter. When the tests were performed on mild steel it was found that the number of pulses and pulse frequency had no significant effect on the hole diameter. For the examination of hole taper the main effects of peak power and pulse width were again found to be significant while f.p.p. was found to be highly significant. The interactions between f.p.p. with the number of pulses and assist gas pressure were determined to be very significant. The optimal results to reduce taper were found using positive f.p.p. and increasing peak power, number of pulses, assist gas pressure, and having a moderate pulse width. Pulse frequency did not have any significant effect on hole taper. When drilling mild steel the only main effect is the pulse width. Lastly hole circularity effects were analyzed where it was obtained that the only significant effects were that of f.p.p., pulse frequency, number of pulses and pulse width. To produce the greatest circularity the combination of negative f.p.p., lower pulse frequency, larger number of pulses and moderate pulse width were used. Pulses after the laser beam break through allows molten material to leave from the hole exit and removes scars from the hole entrance, thus increasing circularity. For mild steel the pulse frequency has no

significant effect. There was found to be no relationship between hole entrance diameter, hole taper, and hole circularity, therefore in drilling stainless steel optimum parameter settings should be obtained in order to achieve the great circularity with the least hole taper. A summary of each of the three responses examined considering the six independent variables is shown below for mild steel and stainless steel (figures 4.12-4.14).

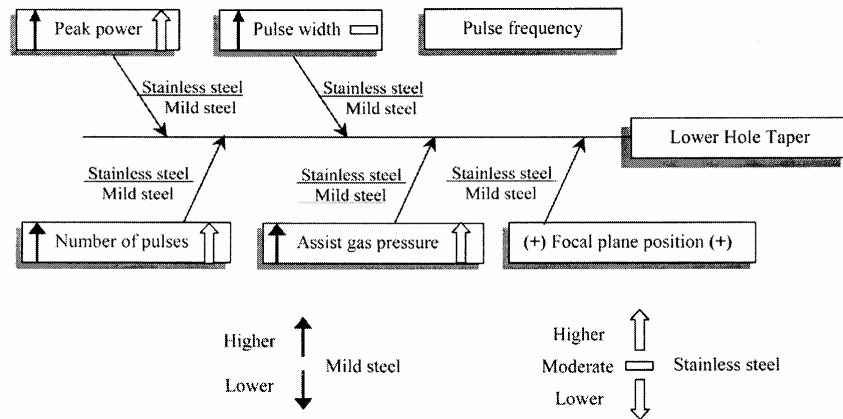


Figure 4.12: Diagram of parameters effect on the hole entrance diameter for stainless steel and mild steel (Ghoreishi *et al*, 2002)

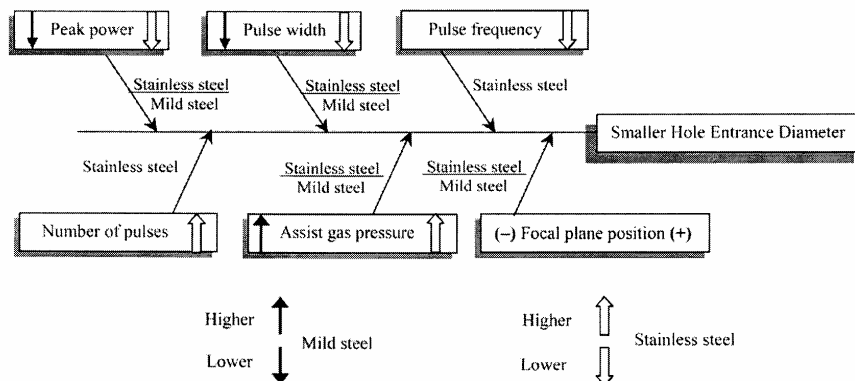


Figure 4.13: Diagram of parameters effect on the hole taper for stainless steel and mild steel (Ghoreishi *et al*, 2002)

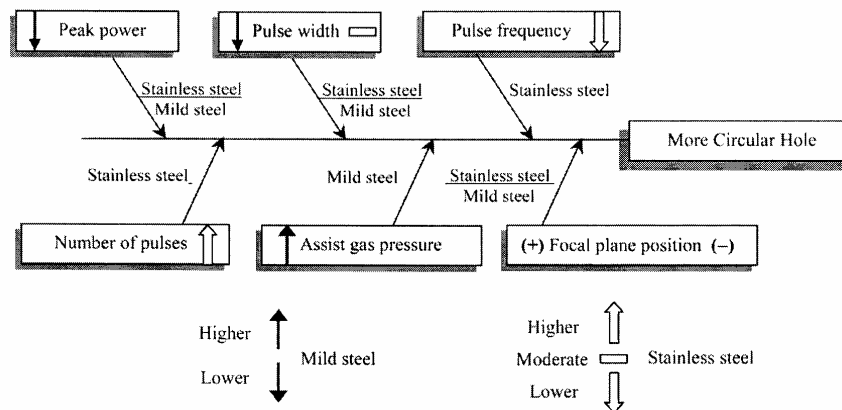


Figure 4.14: Diagram of parameters effect on hole circularity for stainless steel and mild steel (Ghoreishi *et al*, 2002)

Similar to the study above where certain variables were examined to determine their effect on particular hole characteristics, Corcoran *et al* studied the variables effects on microcracking and remelt layers. (Corcoran *et al*, 2001) Experiments were performed using a Nd:YAG laser system with Oxygen as the assist gas on Rene80 substrate with a thermal barrier coating (TBC). Pulse energy, assist gas pressure, pulse shape, pulse width and TBC density were the varied parameters while the output variables were remelt layer thickness, microcracking depth and delamination of the TBC layer. Figure 4.15 shows the summary of the results for each variable. Of greatest concern for this research are the variables that effects remelt layer thickness and microcracking depth. It was found that a high pulse energy reduced the level of microcracking though it increased the amount of remelt material, an apparent interaction effect. Reduction in pulse width reduced the amount of microcracking while a treble pulse shape proved to be best for preventing microcracking. Finally having a higher assist gas pressure proved to minimize all of the output variables

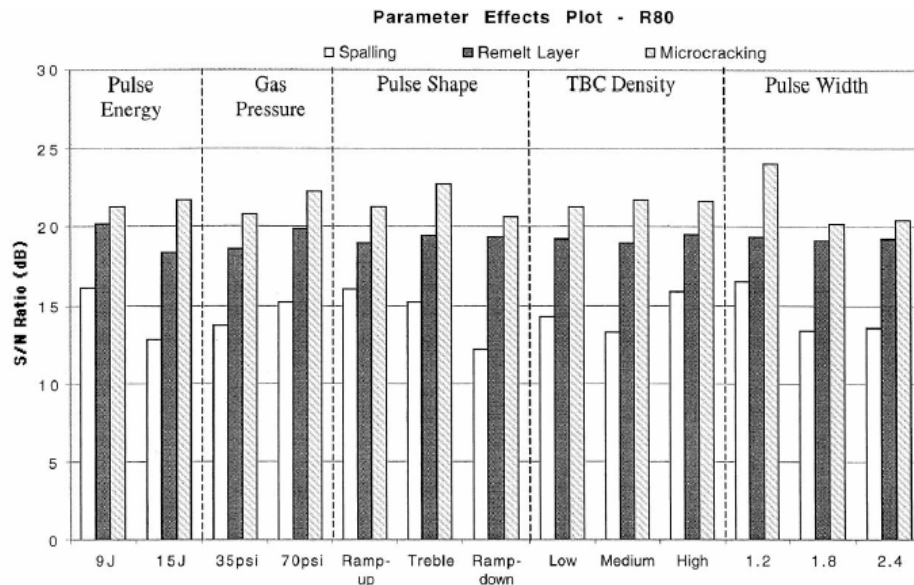


Figure 4.15: Rene80 experiment-parameter effects plot. (Corcoran *et al*, 2001)

One of the largest defects associated with laser drilling is spattering in which molten liquid re-solidifies on the material's surface. One proposed method of preventing this was to apply a specially developed anti-spatter composite coating (ASCC) to the material's surface before the drilling process. (Ng and Li, 2002) Where the ASCC contains a mixture of ceramic filler particles embedded in a silicone elastomer matrix. Testing was performed using a fibre-optic delivered 400W Nd:YAG laser, with the substrate being Nimonic 263 alloy sheet (commonly used material in gas turbine rings and casings). The effectiveness of the coating was analyzed to determine its ability to prevent spatter in closely spaced arrays of holes with four different coaxial assist gases (i.e. O₂, air, N₂, and Ar). The ASCC was applied to the material surface at a thickness of 0.4mm and was cured at an elevated temperature to reduce the curing time to 45 min. Figure 4.16 shows each of the samples drilled without the ASCC coating which reveals the significant amount of spatter that was deposited onto the material surface. Considerable overlapping of adjacent spatter was noted between holes, which was determined to lead

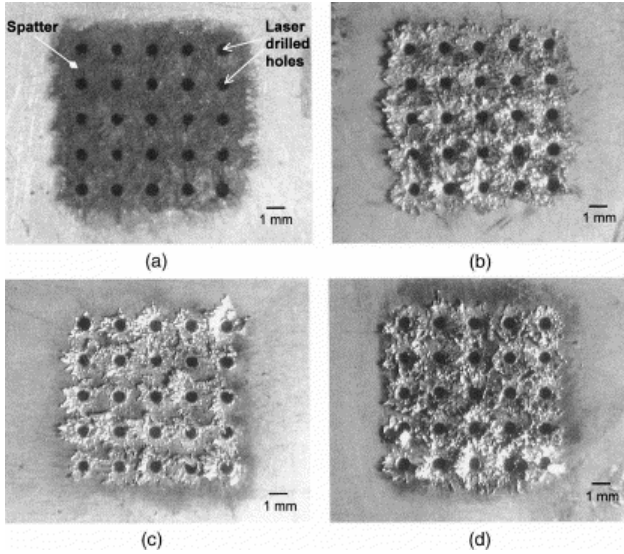


Figure 4.16: Typical optical micrographs of laser drilled array holes (2 mm hole pitch) in uncoated Nimonic 263 alloy using (a) O₂, (b) air, (c) N₂ and (d) Ar assist gases. (Ng and Li, 2002)

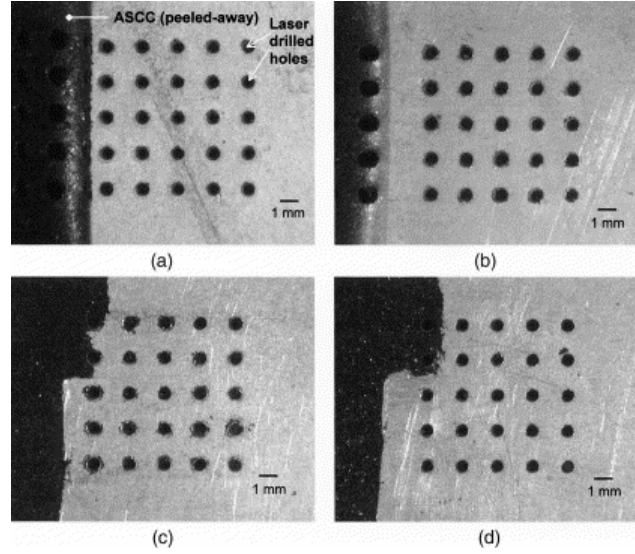


Figure 4.17: Typical optical micrographs of spatter-free laser drilled array holes (2 mm hole pitch) in Nimonic 263 alloy, coated with ASCC prior to laser drilling with (a) O₂, (b) air, (c) N₂ and (d) Ar assist gases. (Ng and Li, 2002)

to an increase in spatter bonding strength. In addition, it was found that when using N₂ and Ar assist gases increased spatter overlapping, thus increasing the spatter bonding strength further. Bonding was increased to such a degree that complete removal might not be possible without causing undesirable surface modification. Additional drawbacks of the increase in spatter were found to affect the consistency and repeatability of the process. Figure 4.17 shows the test pieces that employed the ASCC with the coating peeled away after the drilling process was completed. It's clearly seen how the ASCC coating prevents spatter for all for assist gases used. Optical microscopy revealed that holes drilled with Ar as the assist gas possessed extremely smooth hole periphery, while those drilled with O₂, air and N₂ assist gases showed a gradual deterioration, respectively.

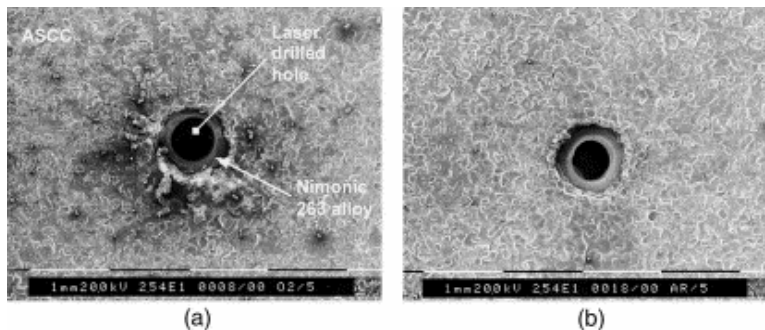


Figure 4.18: SEM surface micrographs of laser drilled holes in ASCC coated Nimonic 263 substrate alloy with (a) O₂ and (b) Ar assist gases. (Ng and Li, 2002)

It was also noted that using Ar as the assist gas provided minimal spattering on the ASCC surface itself when compared to O₂ as the assist gas (shown in figure 4.18). It was also found that the entrance diameter variation reduced from 8% to 3% using the ASCC providing a greater repeatability. (Low *et al*, 2000) Other research has been performed to reduce spattering in ceramics by Guo *et al*. They have proposed a method for preventing spattering and microcracks in ceramics by direct drilling of a gelcast alumina green body that can be adapted for drilling of various materials. (Guo *et al*, 2002)

Repeatability is an important factor when examining laser drilling. If hole parameters are not easily repeated, laser drilling's implementation into industrial applications will be severely limited. The characteristic of melt ejection has a great affect on hole geometry in percussion drilling, and thus affects repeatability as well. A prime example of this concern is shown below where each hole was drilled with the same parameters, but did

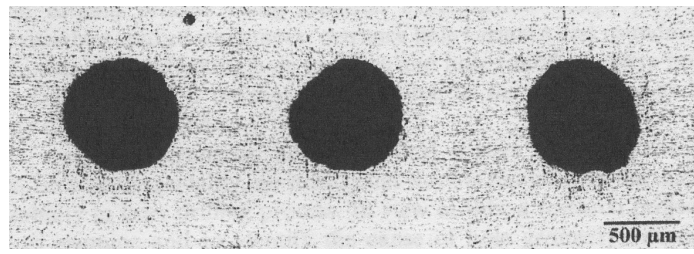


Figure 4.19: Variation of entrance geometry of laser percussion drilled holes under the same operating parameter setting. (Low and Li, 2000, 2003)

not produce the same hole geometry. To determine the optimal parameters for maximizing repeatability a study was performed using a 400W Nd:YAG laser to drill 35 holes for each set of test parameters. (Low and Li, 2000, 2003) The stainless-steel sheets were shot blasted to remove any imperfections and allow for a uniform test surface. After drilling the material was again shot blasted and then polished with silicone carbon papers to remove any splatter. It was found that higher peak power and shorter pulse width produced the greatest repeatability. At a higher peak power, the melt distribution is more uniform and less susceptible to the influence of the gas glow. With a shorter pulse width there is less reaction time between the liquid melt and the parent material, therefore less erosion to the periphery of the hole.

Much of the focus on this research will be aimed at the beam quality provided by the fiber laser being used. This particular laser has a higher beam quality than previous laser systems and has a near Gaussian profile. A higher value for the beam quality allows for greater focusing of the beam, therefore smaller spot sizes. To demonstrate the effect that beam quality has on drilling, specifically exit hole diameter and drilling depth, Rodden *et al* performed experiments using a Nd:YAG laser system by varying the beam quality. (Rodden *et al*, 2002) The results showed that with the poorer beam equality (i.e. $M^2=4.2$) a larger exit hole diameter is produced.

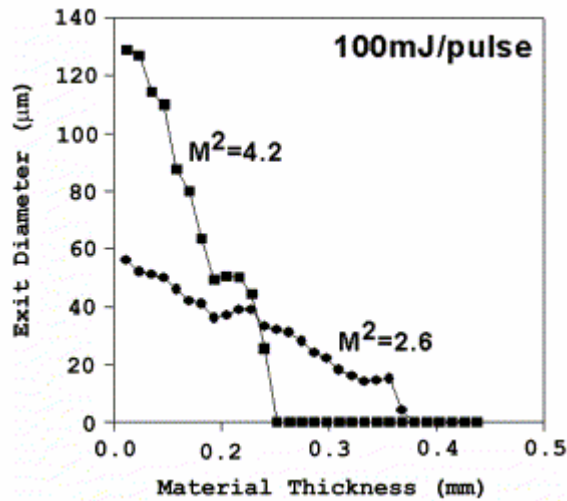


Figure 4.20: Exit hole diameters as a function of material thickness for difference beam qualities (Rodden *et al*, 2002)

In the graph of figure 4.20 it can be seen that the poorer beam quality produces the larger exit hole diameter except when in the unstable region where the poorer beam quality is not able to penetrate the material being drilled. The larger exit hole diameter is a product of the reduced ability to focus the beam with a less Gaussian spatial profile to a small spot size. The graph also shows that the higher beam quality also increases drilling depth. The poorer beam quality directly affects the drilling depth by the lower intensity in the less tightly focused beam.

5 INITIAL FEASIBILITY CHECK

To determine the initial feasibility of causing ablation with a 300W Single Mode CW fiber laser the ablation parameters peak power density, pulse duration, and repetition rate were revisited. The peak power density depends on both the peak power and area of the spot. The peak power for the 300W laser is fixed, therefore this aspect can't be changed. On the other hand the spot size of the beam depends on focusing. Using a 150mm focusing optic the focused spot sized will be 10.8 μ m. Know this the peak power density will be:

$$\text{Peak Power Density} = \frac{\text{Peak Power}}{\text{area}} = \frac{300W}{\frac{\pi}{4}(10.8 \times 10^{-4} \text{ cm})^2} = 0.327 \times 10^9 \text{ W/cm}^2 = 0.327 \text{ GW/cm}^2$$

Most lasers cause ablation at peak power densities larger than $\sim 1 \text{ GW/cm}^2$, therefore this value is slightly low. However this is not too far off and other tweaking may be possible to raise the peak power density. The pulse duration of the fiber laser was found to be a minimum of 15 μ s. This shows that the mechanism for drilling will be in thermal ablation regime as discussed earlier. The repetition rate for this fiber laser is 25 kHz, which is in the reasonable range for laser drilling. Further adjustments to the laser may allow for these parameters to be altered so it appears that there is a good chance for causing ablation with this type of laser.

From later discussions with the manufacturer of the 300W Fiber laser, IPG, it was determined that the current setup could actually produce an enhanced pulse instead of the

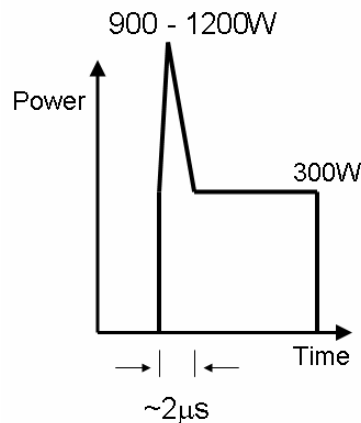


Figure 5.1: Estimated Enhanced pulse for Fiber Laser (IPG, 2003))

standard square pulse. The initial spike in power was estimated to be at least 3 – 4 times the rated power of the laser. The duration of the initial spike was also estimated to be about 2 μ s as well. With this new information the peak power density could be recalculated to determine the impact this initial spike in power will have on the system.

$$\text{Peak Power Density} = \frac{\text{Peak Power}}{\text{area}} = \frac{1200W}{\frac{\pi}{4}(10.8 \times 10^{-4} \text{ cm})^2} = 1.31 \times 10^9 \text{ W/cm}^2 = 1.31 \text{ GW/cm}^2$$

As can be seen from the above equation the peak power density increases from 0.327 GW/cm² to 1.31 GW/cm². It now appears that there is an even stronger possibility for causing ablation with this fiber laser since the peak power density is in the GW/cm² range. Table 5.1 below shows that the power density is now close to that of a typical nanosecond laser. The process parameters of the nanosecond laser can be compared to the fiber laser more easily since they both are in the thermal ablation regime. Both the picosecond and femtosecond lasers are in the non-thermal ablation regime, therefore only their processing capabilities will be compared.

	YLR-300	Nd: YAG	Ti:Sapphire	Ti:Sapphire
	150mm lens	Nano	Pico	Femto
Pulse Width (sec) :	5.00E-05	3.80E-08	3.50E-11	1.30E-13
Energy (J) :	1.62E-02	6.00E-04	1.00E-04	7.50E-04
Peak Power (W) :	1200	15,789	2,857,143	5,769,230,769
Wavelength (nm) :	1075	355	1064	800
Spot Size (μ m) :	10.8	30	40	150
Fluence (J/cm ²) :	17,684	85	150	0.5
Power Density (GW/cm ²) :	1.310	2.23	227.4	32,647
Removal Rate :		1.5 μ m/pulse	0.3 μ m/pulse	0.1 μ m/pulse
Repetition Rate :	20 kHz	10kHz	100kHz	5kHz

Table 5.1: Typical Laser Parameters

6 SPECIFIC RESEARCH PROBLEMS

Though it is predicted that laser drilling will provide a better means of drilling than conventional methods, there still are inherent problems or questions that must be addressed. Accuracy and repeatability of drilled holes are highly significant problems that must be examined. Hole diameter must be a highly controlled variable and needs to be a repeatable process with very little error depending on the application. To allow things to be repeatable the testing equipment and procedures must be consistent and the variables need to be minimized when possible.

Reducing the heat-affected zone is also an important aspect which is one of the possible benefits over conventional drilling. Speed must be maximized since one of the laser's largest contributions to the field of drilling is their capability to process holes faster than conventional methods. One of the largest drawbacks of laser drilling, taper, must be minimized, as well as surface defects produced by the process. Higher aspect ratios can produce difficulties in maintaining the correct hole geometry, therefore this aspect must be monitored.

7 APPROACHES

The researches objectives listed below.

- Ability of the laser to drill holes
- Minimize the hole diameter
- Maximize the aspect ratio
- Compare attainable results with ultra-short pulse lasers capabilities

A benchmark (figure 7.1) that was used for comparison was the series of holes drilled in a 25mm x 19mm piece of sheet steel with a thickness of 137 μ m. The array of holes was created with a picosecond laser operating at 1064nm with a pulse width of 13ps. The exit hole was measured to be about 100 μ m in diameter. Therefore one of the goals will be to see if the 300W fiber laser can match these results.

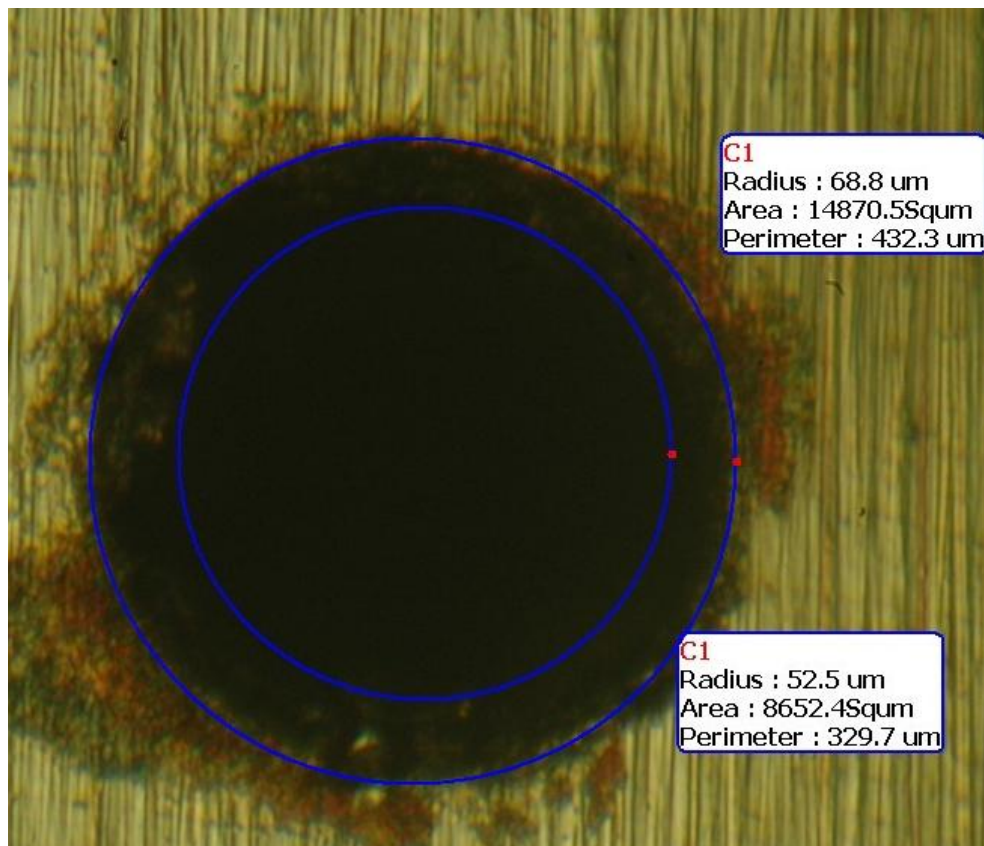


Figure 7.1: Exit hole diameters as a function of material

8 EXPERIMENTAL APPARATUS

The laser used in these experiments is a 300W CW Ytterbium Single mode Fiber Laser (IPG YLR-300). It has a beam quality of 1.04, and wavelength of 1075nm. The overall experimental setup is shown below in figure 8.1. The aluminum structure and all associated equipment is located on pneumatic optical table which isolates vibrations.

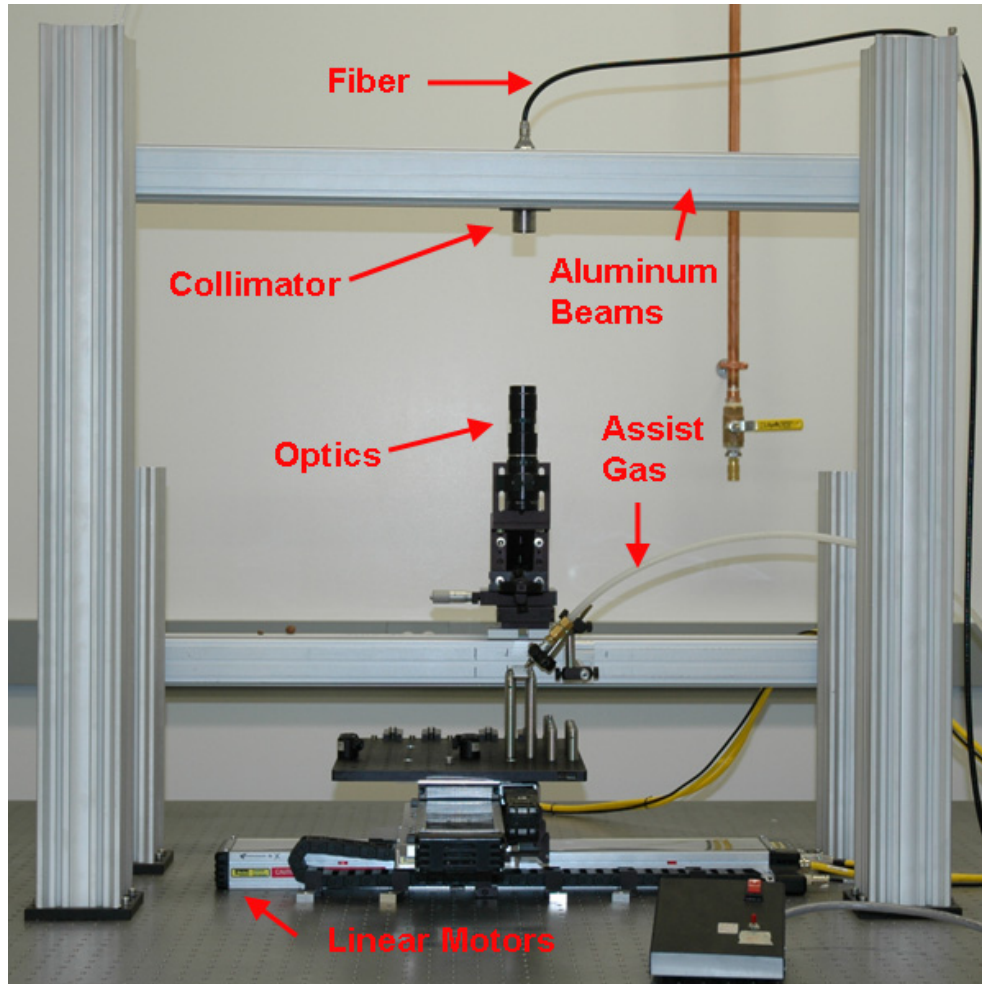


Figure 8.1: Experimental Setup

A set of 404LXR Parker linear motors are used in a xy configuration to move the specimens during experiments. The encoders have a $0.5\mu\text{m}$ resolution and the motors have a 400mm range of travel. A M6 tapped breadboard is mounted to the top of the linear motors for specimen fixturing. The laser's collimator is attached to the upper aluminum beam as shown in figure 8.2.



Figure 8.2: Collimator

To focus the collimated laser, a beam expander set to 5x was used along with a 150mm or 100mm Gradium focusing optic. To position the focusing optic and beam expander, three linear slides were used to provide motion in the x, y, and z coordinates, as shown in figure 8.3.

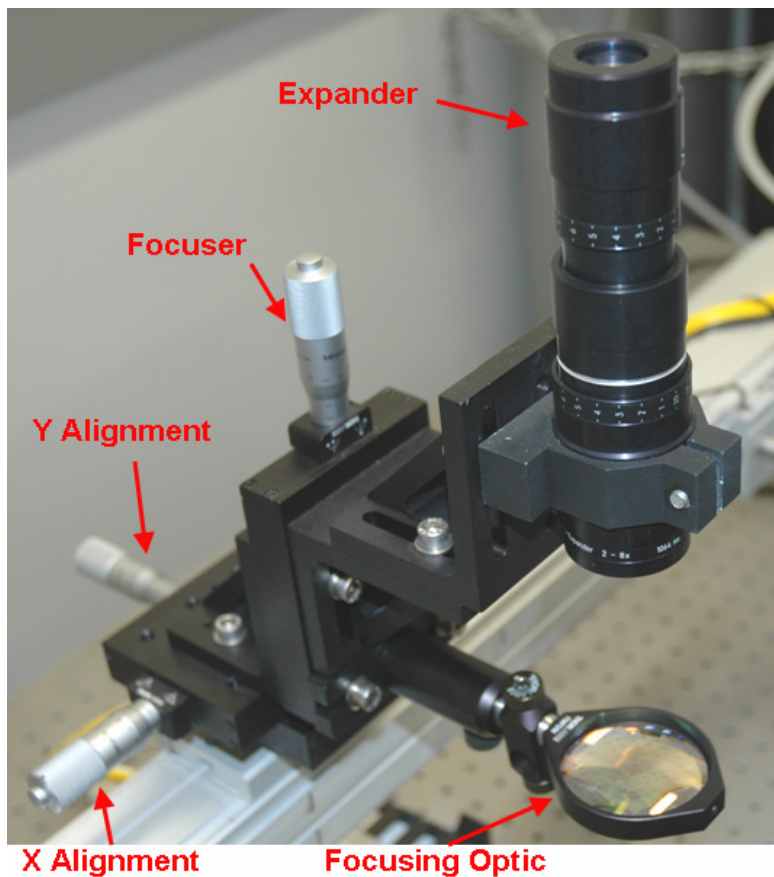


Figure 8.3: Optics Assembly

Polyurethane pneumatic tubing was used to direct Helium assist gas to a nozzle (figure 8.4) pointed at the specimen. The Helium is supplied from a 2000psi tank that passes through a regulator to step down the pressure. The pneumatic line is then connected to a 12V solenoid operated pneumatic valve which feeds the gas to the nozzle (figure 8.5).



Figure 8.4: Assist gas nozzle



Figure 8.5: Solenoid valve

Two computers were used to control the laser and linear motors. The first computer, named servocontrol, was equipped with a Galil DMC-1832 motion controller, along with DMC terminal software. This computer directed the motion of the linear motors and also triggered events in Simulink models. Figure 8.6 shows the DMC terminal where the scripts are written and individual commands can be issued. Scripts are written in the right hand pane and can be downloaded using the file menu. Individual commands may be issued in the top left hand pane, while the bottom left hand pane outputs errors and assorted messages.

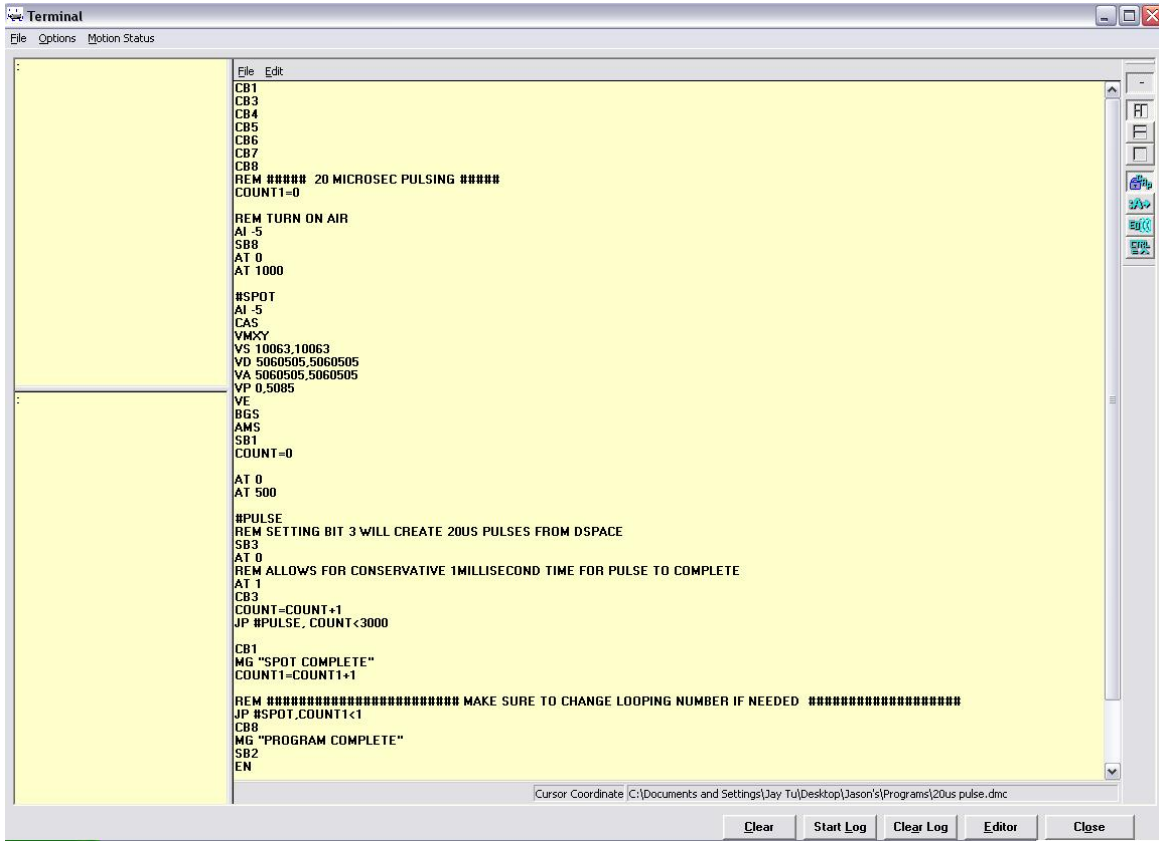


Figure 8.6: DMC Terminal

The second computer, named dataacquisition, was equipped with a Dspace DS1104 R&D controller board that utilized Matlab for data acquisition and control. The dataacquisition computer directly controlled the laser through the external control interface port (figure 8.7).



Figure 8.7: Laser Interface

This external control was made possible by a Simulink model (figure 8.8, see appendix 14.5 for detailed information) that took input commands from the motion controller and relayed specified power schemes corresponding to the input. The Simulink model also allowed for control of the solenoid valve for the Helium assist gas. Pulses were created

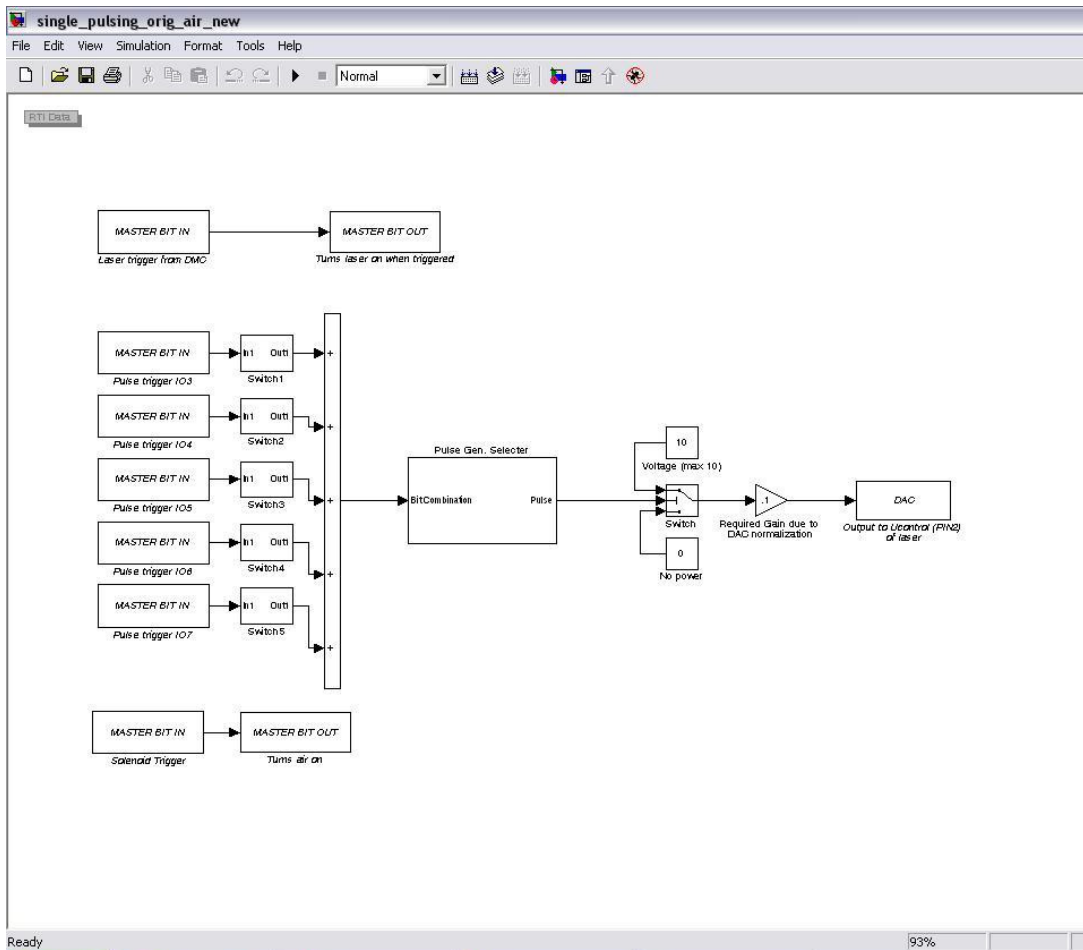


Figure 8.8: Simulink Model

in Simulink by modifying an edge detector. When the edge detector receives an external input from the servocontrol computer it outputs a pulse with an amplitude of 1, indicating the detection of a rising edge. The edge detector was then modified to alter the pulse width of the output by using a transport delay set to the desired pulse time (figure 8.9).

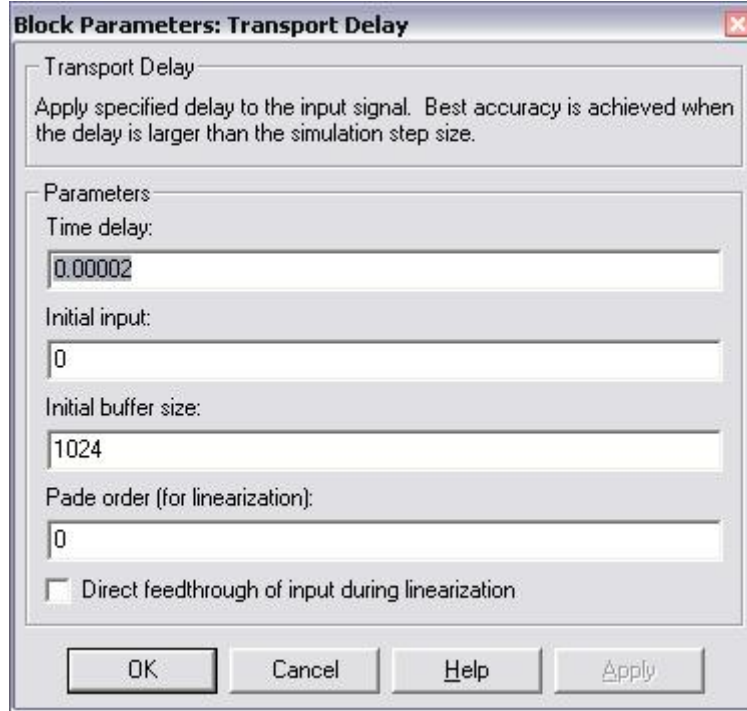


Figure 8.9: Transport Delay Settings

For this instance the time delay of 0.00002 would produce a $20\mu\text{s}$ pulse. To verify that the desired pulsing was being sent to the laser a Tektronix TDS 3012B oscilloscope was used courtesy of Dr. Ramasubramanian.

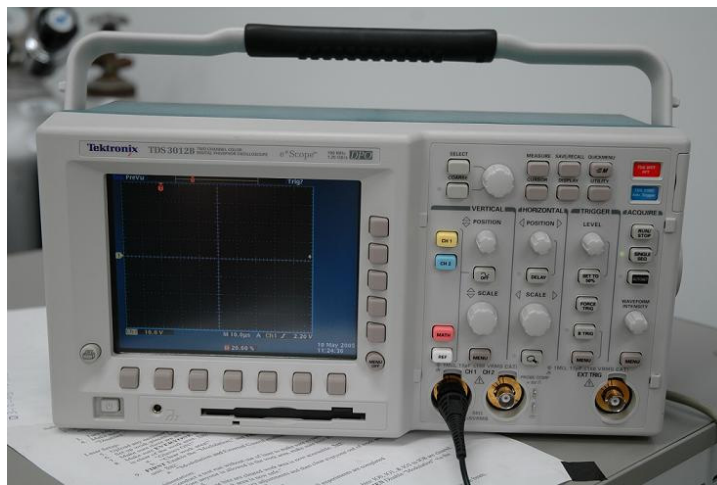


Figure 8.10: Tektronix Oscilloscope

The oscilloscope was connected to the power control output from the Dspace control panel to measure the signal being sent. The laser was then directed to output a specified pulse width while the oscilloscope captured the actual signal being sent. As can be seen in figure 8.12, when the laser was directed to the signal did indeed measure $20\mu\text{s}$ with an amplitude of 10V which would provide 100% power to the laser. All other pulsing schemes were verified with this procedure.



Figure 8.11: Oscilloscope Connection

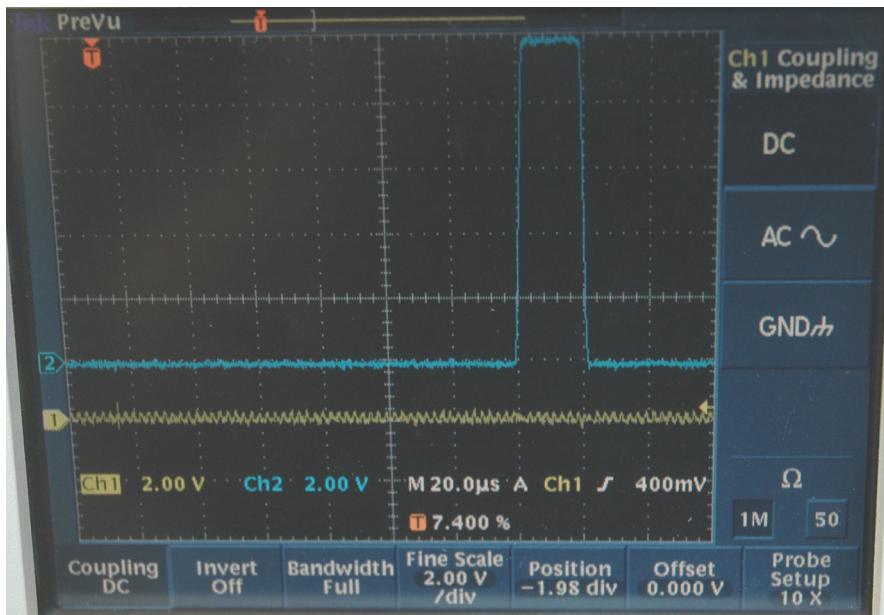


Figure 8.12: $20\mu\text{s}$ Pulse

A Zeiss microscope (figure 8.13) with 2.5x, 8x, 16x, 40x, and 80x objectives were used to examine the specimens. The camera port provided an extra 32x magnification; therefore the 16x objective would provide a total magnification of 480x. The camera used to capture images from the lower section of the microscope was a Nikon D70. Images were taken at the highest resolution of 3008 X 2000 with a 1/5th second shutter speed to allow plenty of light through.



Figure 8.13: Zeiss Inverted Microscope

Surface plots and data were acquired with two different instruments. The first provided a 2D cross-section of the holes, called a Talysurf stylus profilometer. The second instrument, the Zygo NewView 5000 Interferometric Microscope, supplied a 3D plot of the surface along with a 2D cross-section as well. (detailed information in appendices 14.8-14.9)

9 EXPERIMENTAL PROCEDURE

Before any experimentation could be done the laser has to be properly aligned as this can be a significant source of error if not done properly (See appendix 14.4). Using the equation below and using a beam expander set to 5x and a 150mm Gradium focusing optic, the approximate minimal spot size is 10.8 microns.

$$Spot\ Size = \frac{150mm}{25mm * 5} (9\ microns) = 10.8microns$$

where 25mm is the focal length of the collimator, *5 is the magnification produced by the expander and 9microns is the fiber diameter.

This however is only an approximation because the lasers wavelength of $1.075\mu m$ is slightly out of the range for the focusing optic used. Therefore the proper focal distance for minimizing the spot size must be found. This is done experimentally by angling an aluminum plate and welding up the length of the plate which allows for the laser to contact the specimen at different heights. A simple diagram of the test is shown below in figure 9.1. Refer to (Paleocrassas, 2005) for a detailed description and analysis of the tests.

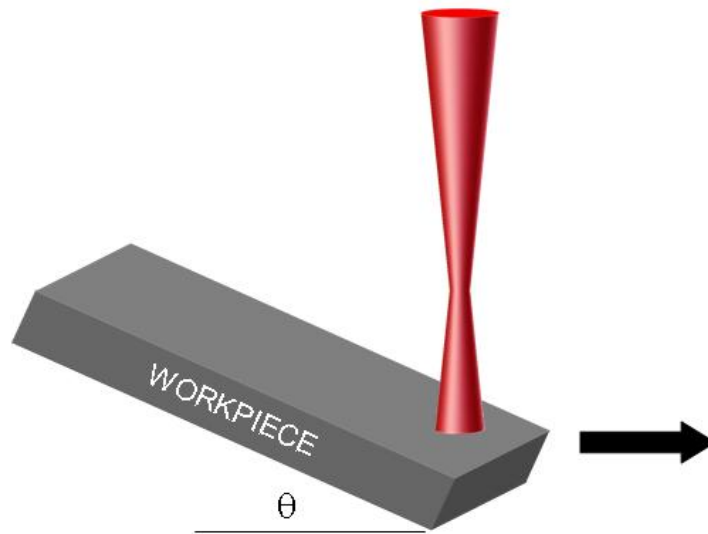


Figure 9.1: Focusing Test



Figure 9.2: 40mm posts

The test piece is then examined to determine at which height the laser had the most effect on the piece. Upon examination there should be an obvious point at which the laser penetrates the material the most, therefore the height from the mounting plate is recorded at this point along with the vertical position of the optics assembly. This provides an estimation for the focal distance, but further tests must be performed around this approximate focal distance to determine the precise height the material must be for optimal drilling. To do this, 8-40mm posts are fixed to the breadboard and fitted with M4 machine screws and washers in the configuration shown in figure 9.2. Tightening the bolts along the 2cm wide strip of steel allows for any warping of the material to be removed yielding a flat specimen needed for accurate results. Now that piece will be at a uniform height over its entire length, different focal distances can be examined. Knowing the height of the specimen from the table, the optics assembly is positioned so that the laser will be focused above the material. The laser is then fired at different locations along the length of the part while lowering the optic assembly in 0.25mm increments. The focal positions used should be centered around the approximate optimal focal position found earlier. Next examine and measure the drilled holes under the microscope. The drilled areas are brought into focus using the 16x objective on the microscope along with the DIC adjustments to provide better height differentials. Images are taken from the bottom portion of the microscope using the Nikon D70 digital camera in manual mode with a 1/5 second shutter speed. The images can then be imported into

the Motic software where their size is adjusted to 50%. The software is then set to measure with the 16x objective and 50% image size. Circles are then sized to the holes which provide the needed diameters. Plotting the diameters of the holes and noting where the smallest diameter was achieved with the characteristics needed shows where the optimal focus was obtained. Again this is still somewhat of a coarse measurement so the experiment is repeated centering the range around the new optimal focal position and decreasing the increment from 0.25mm to 0.10mm. Repeating the microscope measurement will yield the final value for the optimal focal position. Before conducting any of these experiments, a Simulink model must be created and compiled along with an appropriate DMC script to issue the commands for the laser, assist gas, and motors.

Once the optimal focal position and other process parameters are found, multiple pulses can then be created. A new DMC script is created to issue multiple pulses with rests of 50 μ s in between each pulse to allow for the laser build up enough energy.

10 RESULTS AND DISCUSSION

10.1 Initial Focal Tests

The first test run was to estimate the focal distance from the optics assembly when using the 150mm Gadium lens. The coarse welding focus test was performed and upon examining the plate the optimal penetration for welding was found to be 39.7mm up from base breadboard plate at a focusing position of 11mm on the optics assembly. Now that this was know the focusing tests could then be performed by drilling on a flat surface. The material being examined here is 316 stainless steel sheets with a nominal thickness of 0.95mm and a thickness tolerance of about ± 0.1 mm. Therefore using 40mm posts and a material thickness of about 0.95mm would require the optics assembly to be at 9.75mm on the vertical positioner. To be conservative, a range from 7mm to 12mm was chosen for the focal position of the system during the new focus test. Holes were created in specimens for each focal position in the range at increments of 0.25mm. This first focal test utilized a single 1ms pulse for each position while all tests were performed with the laser at 100% power. The results were examined with the Zeiss Microscope using the 16x objective and pictures were taken of each hole.

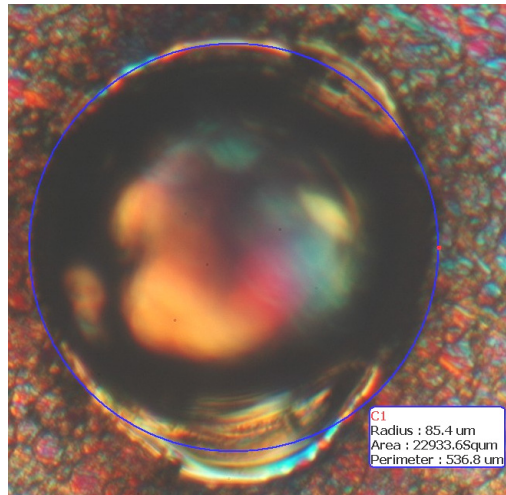


Figure 10.1: Hole created from 1ms pulse

The diameter of every hole was then measured with the Motic software. The image in figure 10.1 shows the hole created at the 9.5mm focal position. This position proved to be the most optimal for drilling over the given range since it produced the smallest

diameter and greatest penetration. The radius of the hole was measured as $85.4\mu\text{m}$, or a diameter of $170.8\mu\text{m}$. Figure 10.2 shows a plot of each hole's diameter as a function of the focal position. As can be seen from the plot the diameters drastically change in the positions around the optimal focal position, increasing almost 75%.

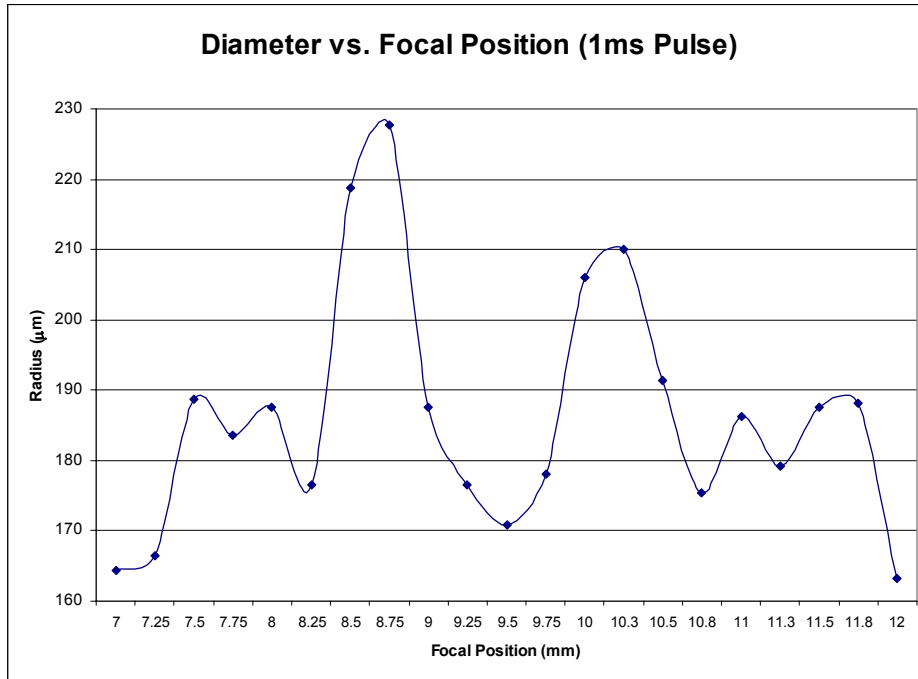


Figure 10.2: Plot of Focus Test #1 Results

Though the outer focal positions appear to have smaller diameters than the optimally focused position, the hole's characteristics are not what is desired. Shown below in figure 10.3 is one of these holes created which are actually raised surfaces. The focal positions in between the extremes and the optimal provide holes with a lot of melting which is also undesired.

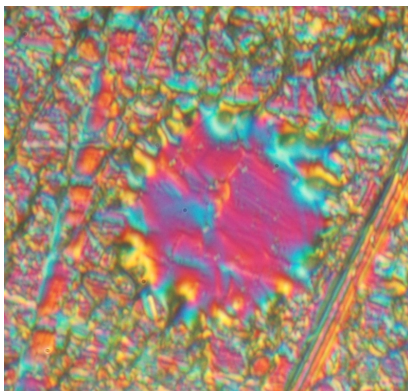


Figure 10.3: Undesired melting at non-focused position

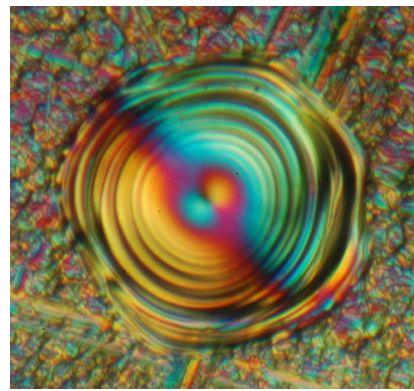


Figure 10.4: Undesired surface at non-focused position

Further tests were performed to validate the repeatability of this optimal position and to verify that it would be the same for smaller pulse widths. Table 10.1 shows a summary of the tests performed. As can be seen from the table, the various pulse width schemes all agreed upon the same position of 9.5mm for the focusing optic. The tests also revealed that the diameters of the holes created stayed around 40 μ m for all 50 μ s pulse width tests, but drastically increased with increasing pulse time. A plot of the tests over the focal range is shown in Figure 10.5. The graph shows that the curves for the 50 μ s pulsing closely mimic each other in magnitude and general shape even when increasing the pulse number while the larger pulse width curves are off in magnitude, but still have similar shapes. The plot shows that a change in less than 1mm of the focal position can produce a significant change in radius, therefore revealing how crucial the focal position is.

Focus Test #	Pulse Width (μ s)	# of Pulses	Optimal Focal Position (mm)	Diameter of Hole (μ m)
1	1000	1	9.5	170.8
2	50	1	9.5	82.6
3	50	2	9.5	80.6
4	50	4	9.5	82.6
5	100	1	9.5	99.2

Table 10.1: Summary of Initial Focal Tests

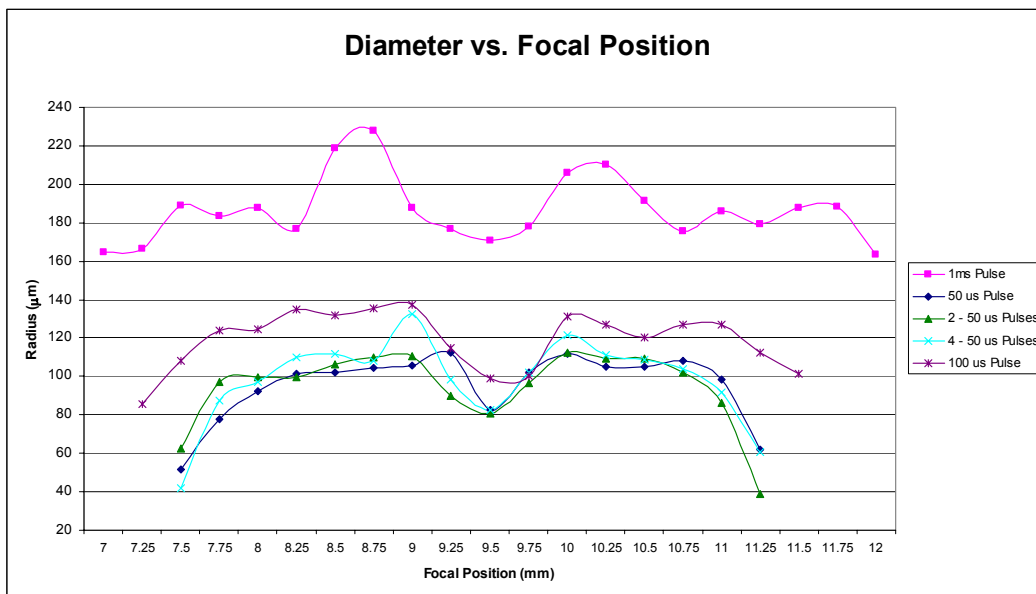


Figure 10.5: Holes created from varying pulse widths

Though it is obvious that increasing the pulse width will increase the hole diameter, there are two other factors that must be considered to show the benefits of using the smallest pulse time. Reducing the pulse width can effectively reduce the HAZ since there is less time for the laser to react with the specimen, thus reducing conduction. The second factor of importance is that even though the laser being used is for continuous power, the beginning of the each pulse can produce a spike in output power given enough rest time, called an enhanced pulse. Therefore if the pulse width is reduced and the number of pulses is increased, the impact of this power spike can be emphasized. The magnitude of this power spike has been estimated by the manufacturer to be between 900 to 1200 Watts.

10.2 Relocation Focal Tests

Before all the experimental testing was finished, the laser and all associated equipment had to be relocated to a new lab. This created a need for retesting the optimal focal position since the new setup of the equipment could produce discrepancies when compared to previous results. As expected the first test performed revealed that the optimal focal position had changed from the original value of 9.5mm. A new 50 μ m pulse test was performed to determine the new optimal focal position for drilling. Figure 10.6 shows that the new optimal focal position was found to be somewhere around 8.75mm.

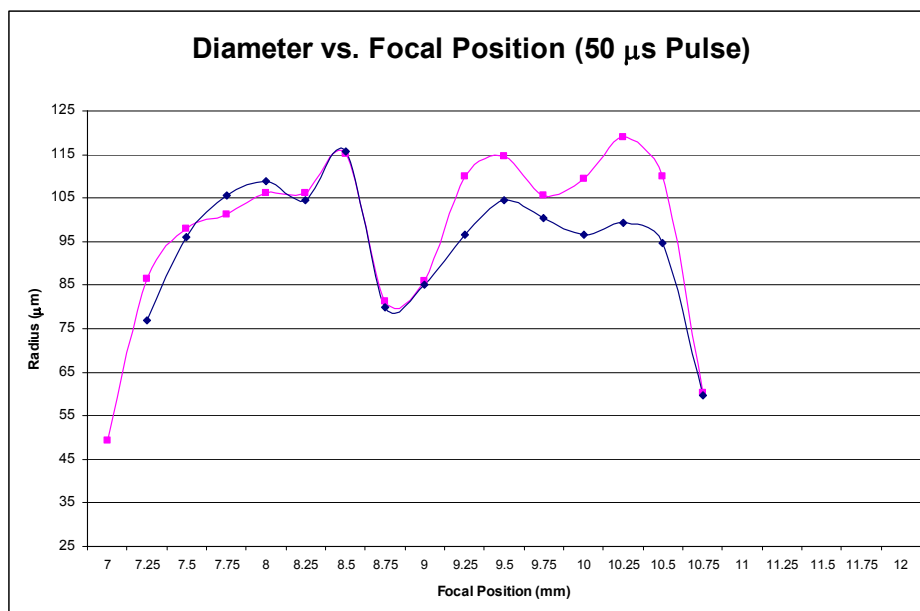


Figure 10.6: Holes created from 50 μ s pulse after relocation

To find a more accurate value for the new optimal focal position, more tests were performed using smaller increments. This time a range of 8mm to 10mm was chosen with 0.10mm increments. These tests showed that the new focal position was actually at 8.9mm. Figure 10.7 shows a nice smooth curve around the focal position resulting in the smallest diameter of 79.4 μ m. The test was repeated several times to verify the new focal position

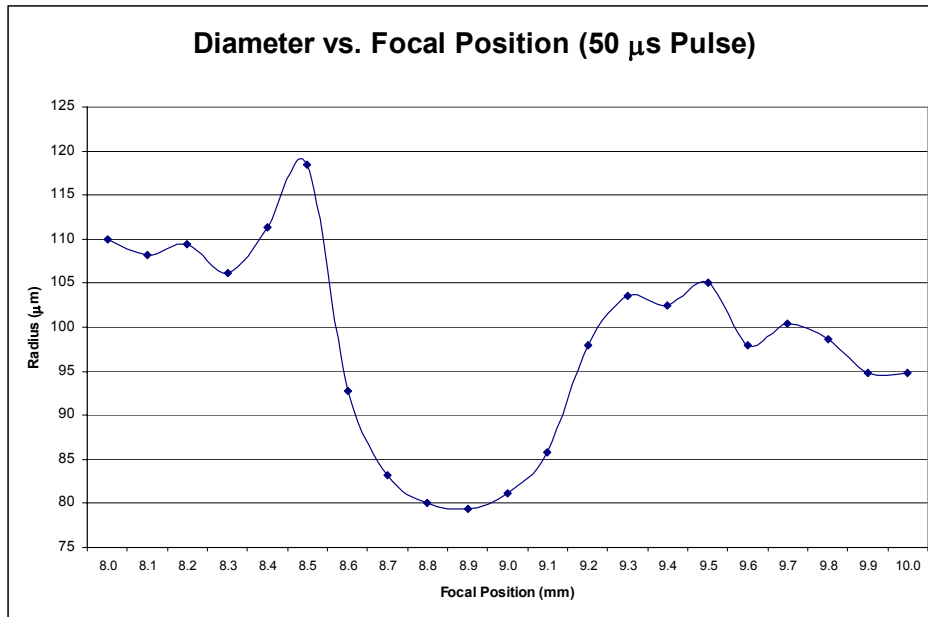


Figure 10.7: Refined focal test using 50 μ s pulse (after relocation)

Now that the proper focusing was found it was time to take a closer look at the holes being created to determine the depth of the holes. To accomplish this the specimen was brought to the Precision Engineering center where they have several instruments for measuring surface profiles. Holes at three different focal positions were chosen for the measurement, 8.7mm, 8.9mm, and 9.1mm. These were chosen to see the difference in the material removal rate (MMR) when the laser was focused on the surface and when it was focused into and out of the surface. The first instrument used to determine the surface profile was the Zygo NewView 5000 Interferometric Microscope. This provided 2D and 3D profiles of the surface. Figure 10.8 shows the measurement of the hole at the 8.7mm focal position. To much surprise the measurement showed that there was a raised surface and not a hole at all. The measurement was taken again several times and

verified this discovery. The height of the raised surface was measured at about $8\mu\text{m}$, therefore was very significant when compared to the hole diameter.

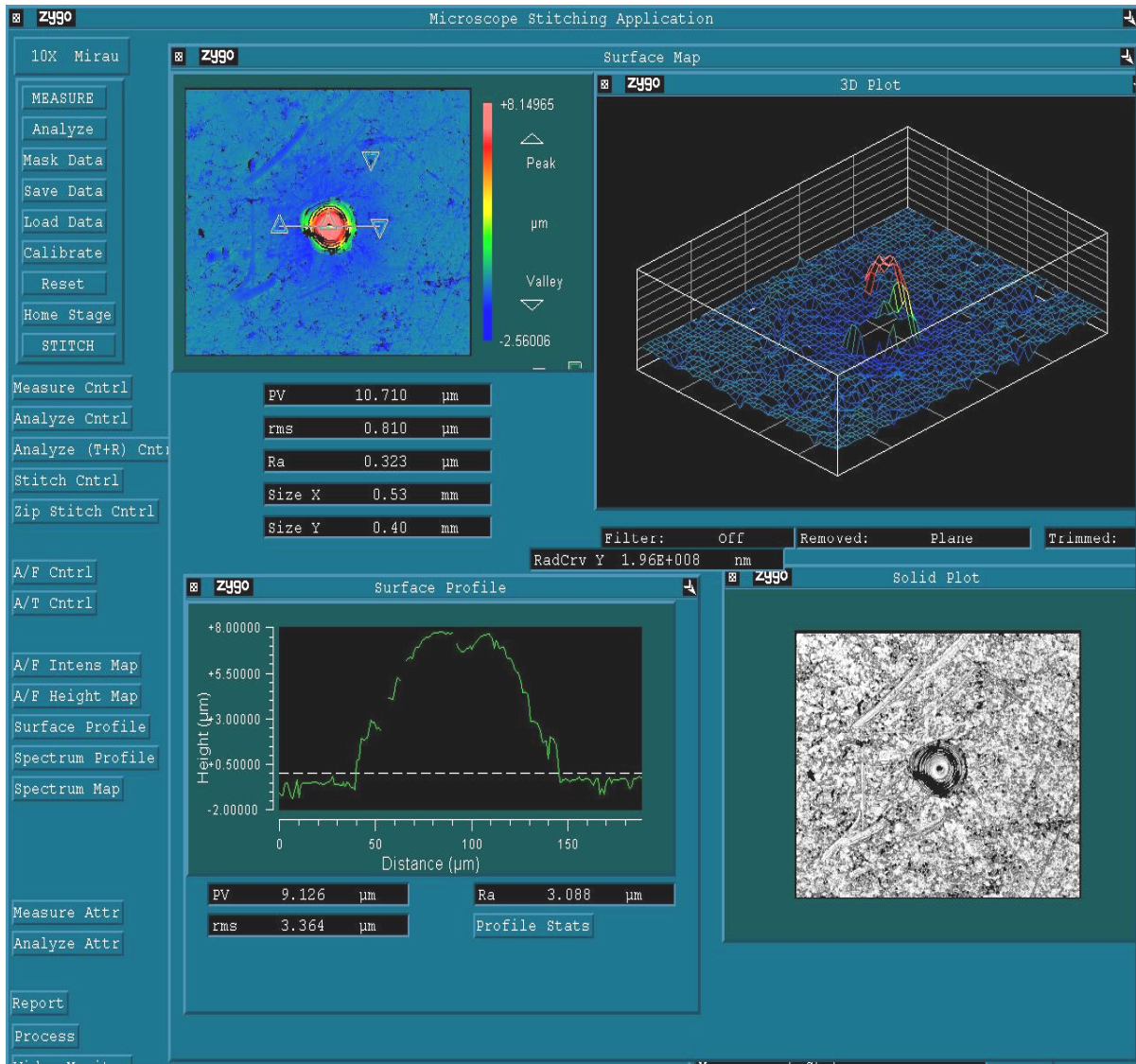


Figure 10.8: Zygo measurements of hole at 8.7mm focal position

The same measurement was then done for the optimally focused hole at 8.9mm. This measurement did not come out as clear (figure 10.9) due to poor reflectivity from the measurement area which the Interferometer depends on. It can still be seen though that there is again a raised surface instead of an indentation. Though the diameter was smaller this time, the height of the peak was even larger at $15\mu\text{m}$.

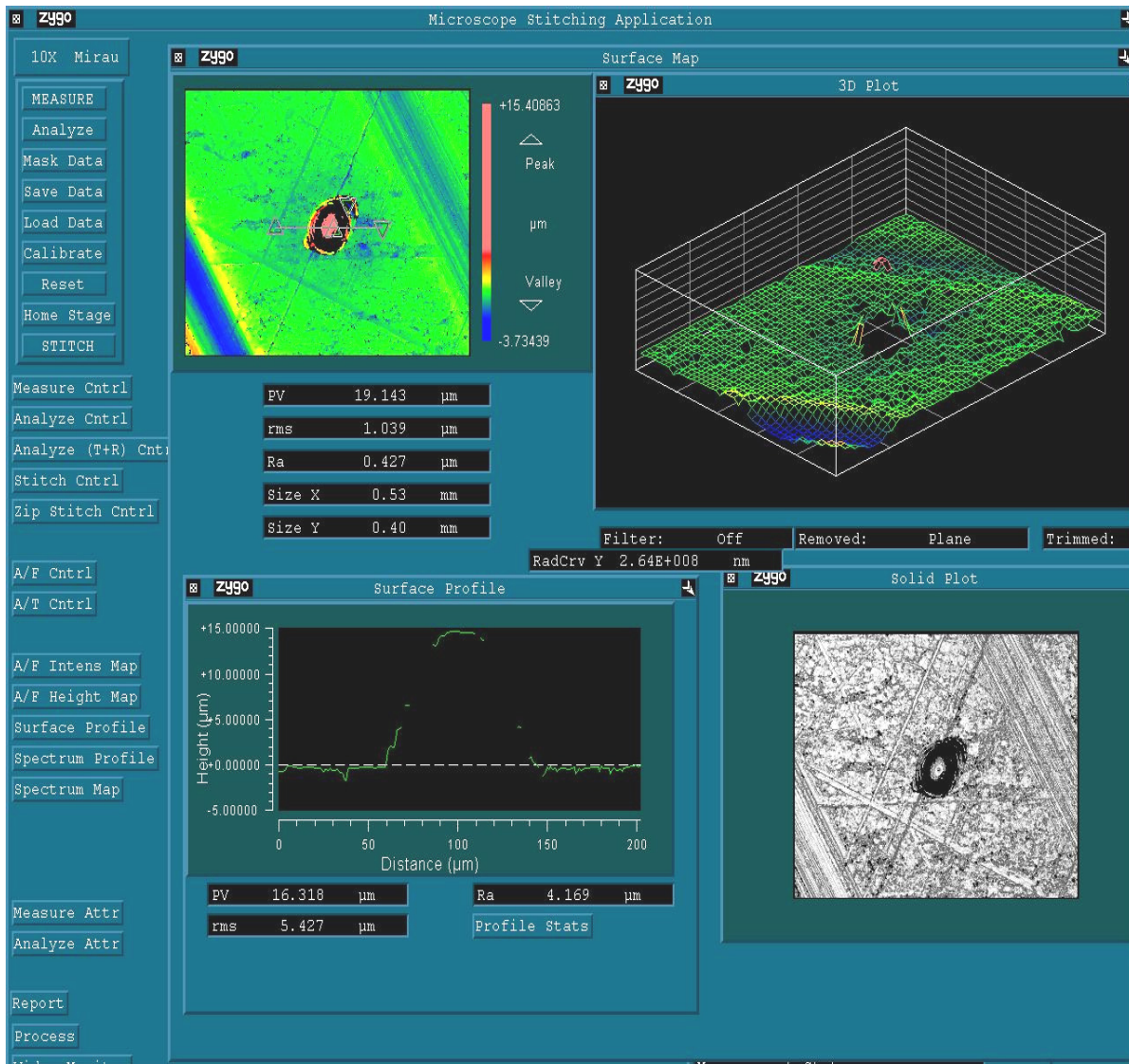


Figure 10.9: Zygo measurements of hole at 8.9 mm focal position

Finally the last hole at a focal position of 9.1mm was checked to determine if it had the same characteristics as the first two holes. Again figure 10.10 shows that the raised surface was around 15 μm high while the diameter increased as it was expected to.

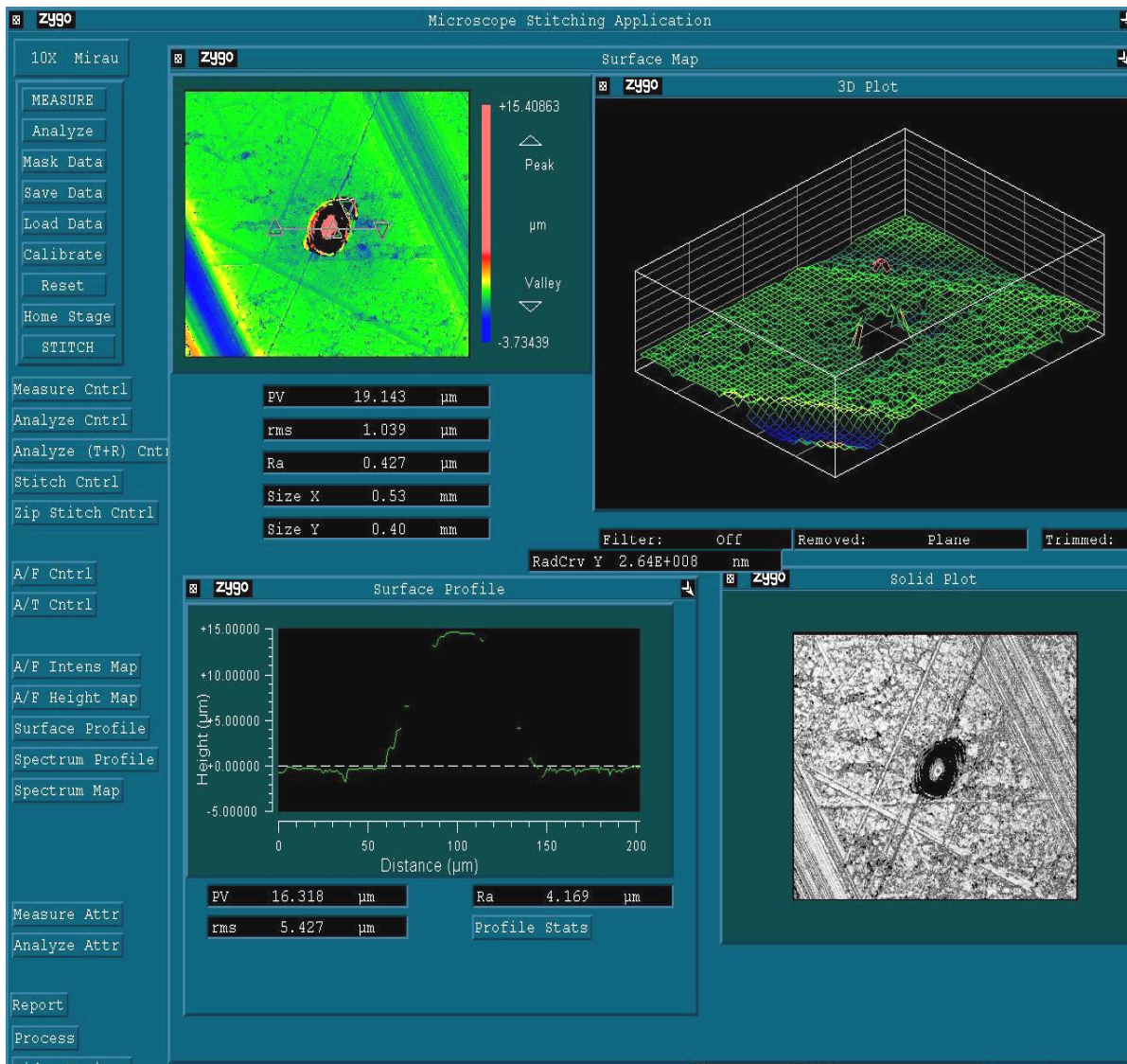


Figure 10.10: Zygo measurements of hole at 9.1 mm focal position

From the results of these tests it was obvious that there was some inherently wrong. It was apparent that the power density was most likely not high enough to cause ablation and was therefore really creating spot welds. Using the 150mm lens provided a spot size of $10.8\mu\text{m}$, thus the power density could be calculated as:

$$\text{Power Density} = \frac{\text{Power}}{\text{area}} = \frac{1200W}{\frac{\pi}{4}(10.8 \times 10^{-4} \text{ cm})^2} = 1.31 \times 10^8 \text{ W/cm}^2 = 1.31 \text{ GW/cm}^2$$

10.3 100mm Lens Tests

To increase the power density the 150mm focusing optic was replaced with a 100mm lens. This decreased the spot size to:

$$\text{Spot Size} = \frac{100\text{mm}}{25\text{mm} * 5} (9 \text{ microns}) = 7.2\text{microns}$$

The decrease in spot size raised the power density to:

$$\text{Power Density} = \frac{\text{Power}}{\text{area}} = \frac{1200W}{\frac{\pi}{4} (7.2 \times 10^{-4} \text{ cm})^2} = 2.947 \times 10^8 W/cm^2 = 2.947 GW/cm^2$$

The reduction in spot size allowed for the power density to increase by 225% which is now higher than the power density given in Table 5.1 for the nanosecond laser. Due to the change in focal length of the lens, the 40mm posts that raised the specimen to the correct height had to be replaced by 100mm posts. The aluminum beam that held the optics assembly also had to be readjusted since the vertical positioner of the assembly was out of range at the new focal distance. These changes created the need for new focusing tests to be performed. The 50 μs (figure 10.11) tested showed that the new focal position was about 11.50mm.

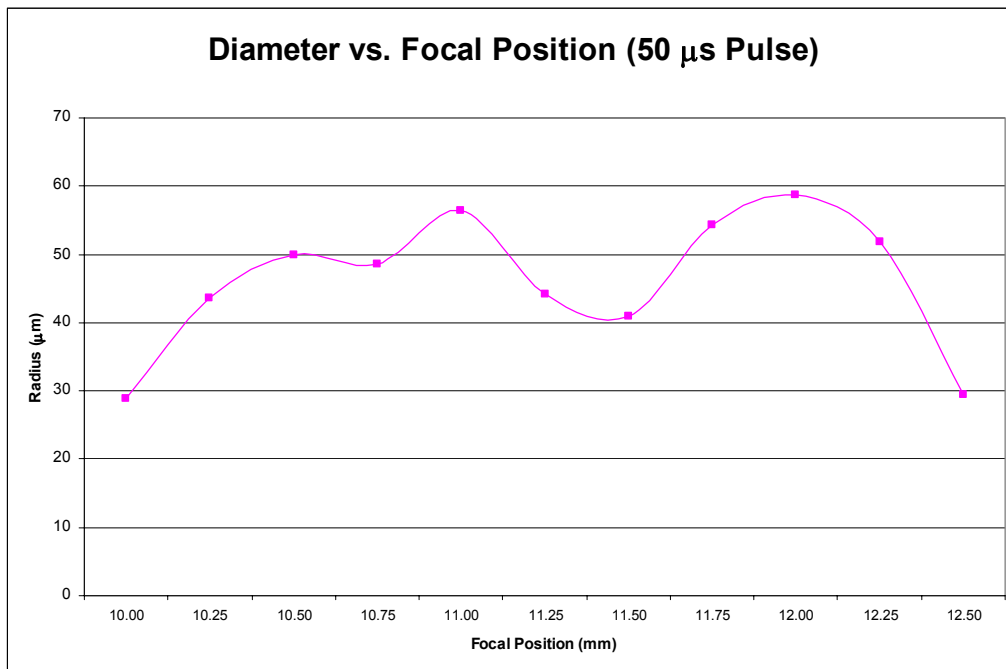


Figure 10.11: Focusing test using new 100mm lens

A more refined test showed that the focal position was actually at 11.60mm for the specimen. The addition of the new 100mm optic made focusing even more important than before because the laser beam converges more drastically, therefore the same change in focusing depth produces greater change in spot size. An experimental study was done with this laser to determine the spot size at different focal depths. (Paleocrassas, 2005) Figure 10.12 shows the plot of the spot radius as a function of focal depth for the previous 150mm lens. This was produced assuming that the beam is symmetric, constant power is being supplied and that the smallest spot radius is 5.4 μ m.

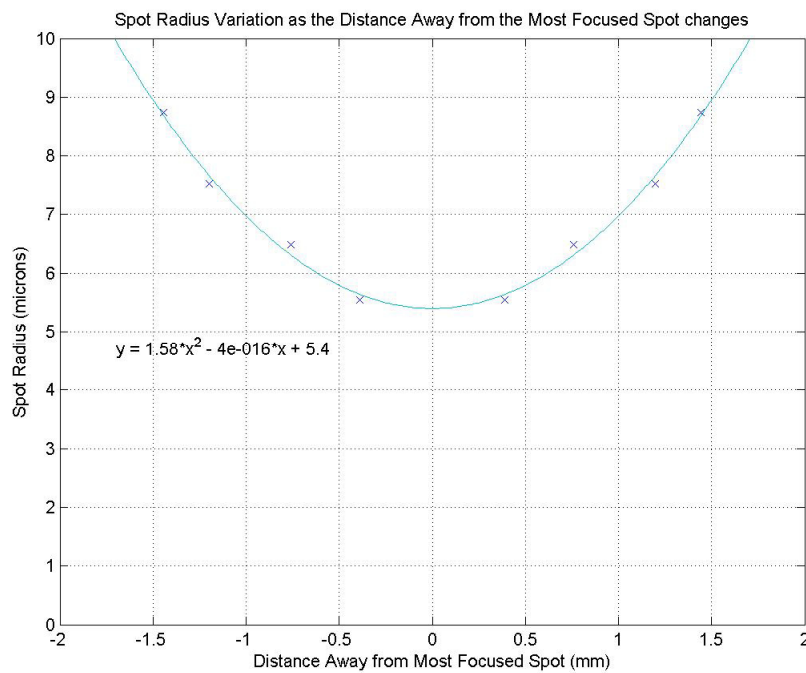


Figure 10.12: Spot radius as a function of focusing depth for 150mm lens (Paleocrassas, 2005)

Therefore a change in just 1mm would produce radius of:

$$R = 1.58 \cdot x^2 - 4 \times 10^{-16} \cdot x + 5.4 = 1.58 \cdot 1^2 - 4 \times 10^{-16} \cdot 1 + 5.4 = 6.98 \mu\text{m}$$

From this it can be seen that the diameter would have changed from 10.8 μ m to 13.96 μ m.

The power density would then change from 1.31 GW/cm² to:

$$\text{Power Density} = \frac{\text{Power}}{\text{area}} = \frac{1200W}{\frac{\pi}{4} (13.96 \times 10^{-4} \text{ cm})^2} = 0.784 \times 10^8 \text{ W/cm}^2 = 0.784 \text{ GW/cm}^2$$

Otherwise a 40% decrease in power density.

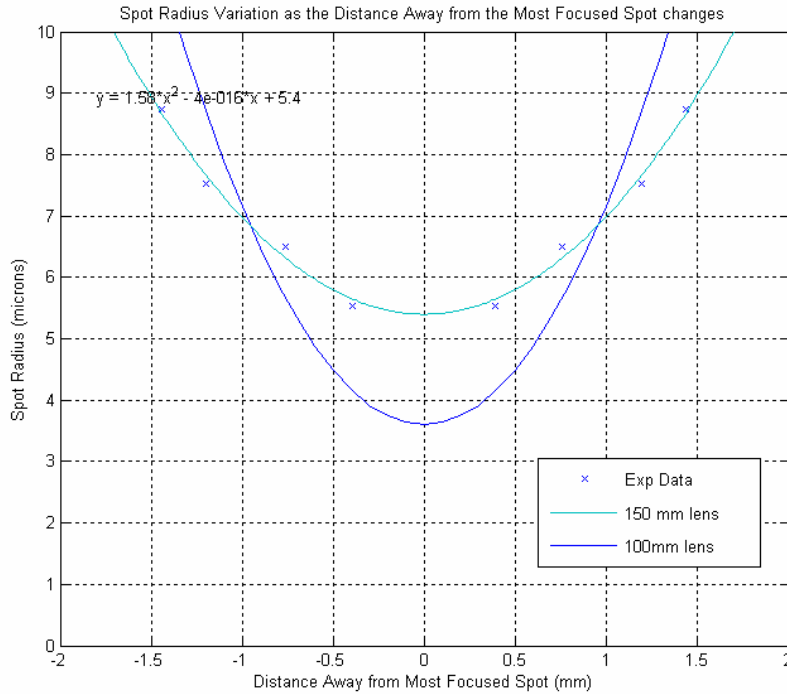


Figure 10.13: Spot radius as a function of focusing depth

If the same is done for the 100mm focusing lens the plot would then appear as it does in figure 10.13. Now a 1mm change in focal depth will produce a change in radius of:

$$R = 3.555 \cdot x^2 - 9 \times 10^{-16} \cdot x + 3.6 = 3.555 \cdot 1^2 - 9 \times 10^{-16} \cdot 1 + 3.6 = 7.15 \mu\text{m}$$

From this it can be seen that the spot diameter would change from $7.2 \mu\text{m}$ to $14.3 \mu\text{m}$.

The power density would then change from $2.947 \text{ GW}/\text{cm}^2$ to:

$$\text{Power Density} = \frac{\text{Power}}{\text{area}} = \frac{1200W}{\frac{\pi}{4} (14.3 \times 10^{-4} \text{ cm})^2} = 0.747 \times 10^8 \text{ W}/\text{cm}^2 = 0.747 \text{ GW}/\text{cm}^2$$

Otherwise a 75% decrease in power density. Knowing that focusing is so critical now great care was taken to ensure the specimen was flat as possible and the tests we repeated several times to verify the results. After repeated tests and observation of the holes under the microscope it was still apparent that they were raised surfaces instead of indentions. This was done by noticing that the middle of the apparent holes came into focus first when moving the objective towards the piece.

10.4 *20 μ s, 30 μ s, and 40 μ s Pulse Width Tests*

Since the efforts thus far had not produced holes, the ablation parameters were revisited. Comparing the current power density of 2.947 MW/cm^2 with the power density for the typical nanosecond laser power density of 2.23 GW/cm^2 , it appears that the current power density should be more than sufficient. Therefore the ablation parameter that is left to be examined is the pulse duration. As it was mentioned earlier the pulses produced by this laser are referred to as an enhanced pulse that is the combination of a spike pulse and a normal square pulse. The width of the initial spike pulse was estimated to be around 2-3 μ s. Since this spiking phenomenon is one of the main interests of these experiments it was recognized that the current pulsing scheme of 50 μ s might be too large compared to the width of the spike in power. Therefore to place more emphasis on this spike the overall pulse width had to be shortened beyond 50 μ s. Previously this had been the limit of the Simulink model, but a workaround for this limitation was found so that 20 μ s pulse times were possible. A new set of focal tests were done for 20 μ s, 30 μ s, and 40 μ s. Though the focal position was already found to be at 11.60mm the irregularities in the part warranted a range of focal positions to be tested. This also allowed for examination of the characteristics for the spots created around the optimal focus as well. The plot in figure 10.14 shows a summary of the tests comparing the different pulse widths.

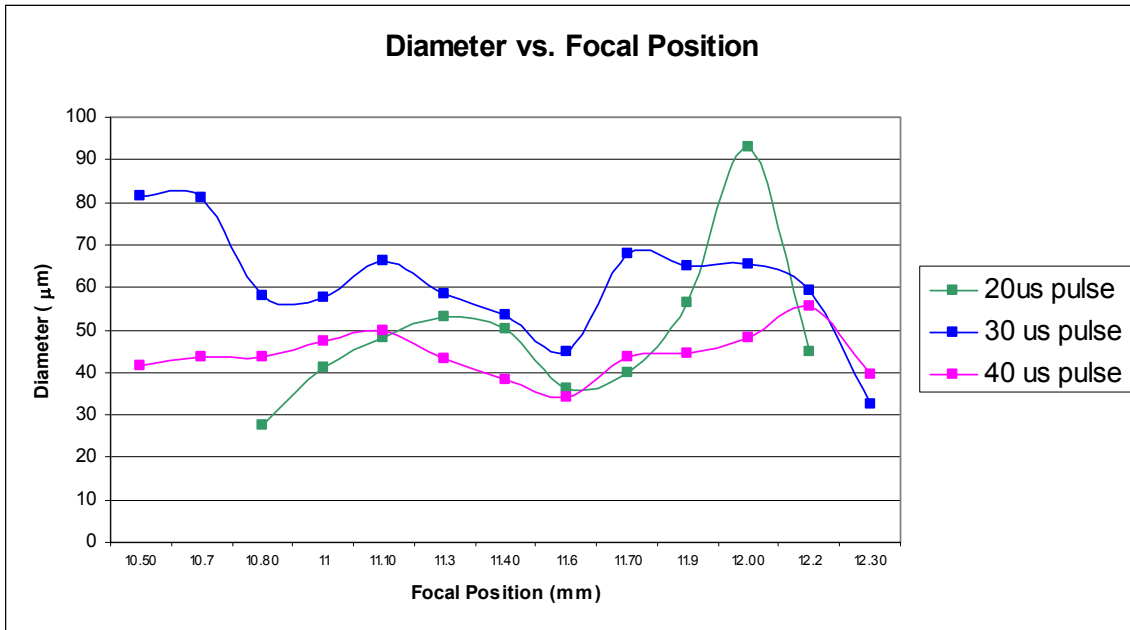


Figure 10.14: Spot Diameter as a function of focusing depth for 100mm lens

The 40μs, 30μs, and 20μs pulsing tests all verified that the optimal focus was obtained at a focal position of 11.60mm. When examining the 20μs pulsing test it was quickly realized that an actual indentation was formed instead of a raised surface. However this was not at the smallest diameter spot. The actual hole was achieved at the next spot location (figure 10.15) with a diameter of 40.1μm which suggests that the optimal focus may lie in between these two locations. Retesting showed that the discrepancy was most likely do to the specimen not being held flat.

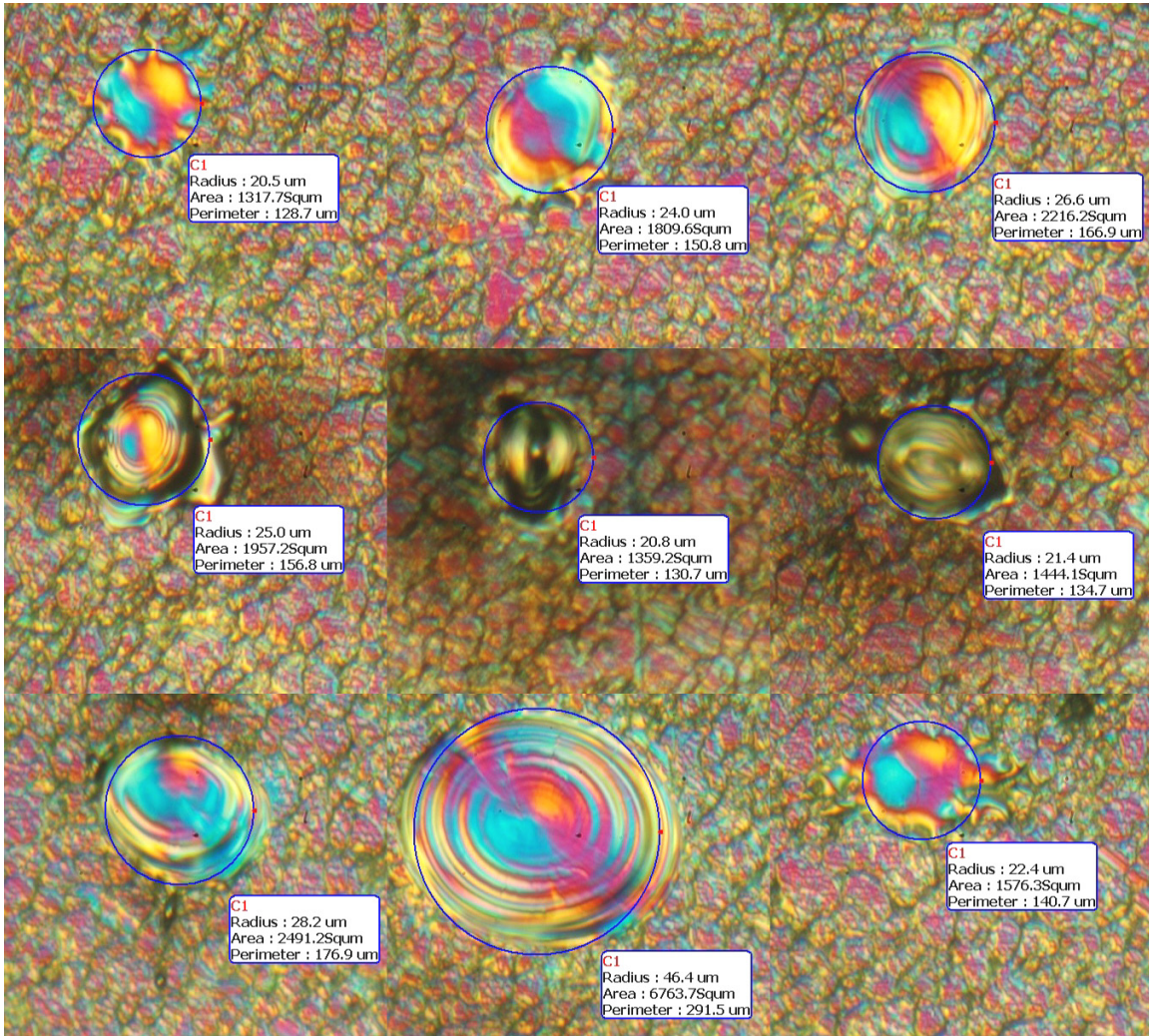


Figure 10.15: Spot images for 20us test, starting with the top left and going left to right in each row

Figure 10.16 shows the highly magnified hole produced at a 20 μ s pulse. The microscope was roughly calibrated by re-measuring the previous spots that created raised surfaces. Since the height of these were known the ticks on the focusing wheel of the microscope wheel were calibrated by focusing on top of the raised surface and counting the number of ticks it took to get the specimen's surface. The known height of the surface was then divided by the number of ticks to get the height difference for each tick on the focusing wheel. With this the hole was estimated to have a depth of about 22 μ m.



Figure 10.16: Enlarged hole image for 20us test , 40X objective

The hole was then tested using the Zygo NewView 5000 Interferometric Microscope. Though the 2D profile in figure 10.17 did not come out very detailed it does show that the bottom of the hole is over 23 μ m in depth.

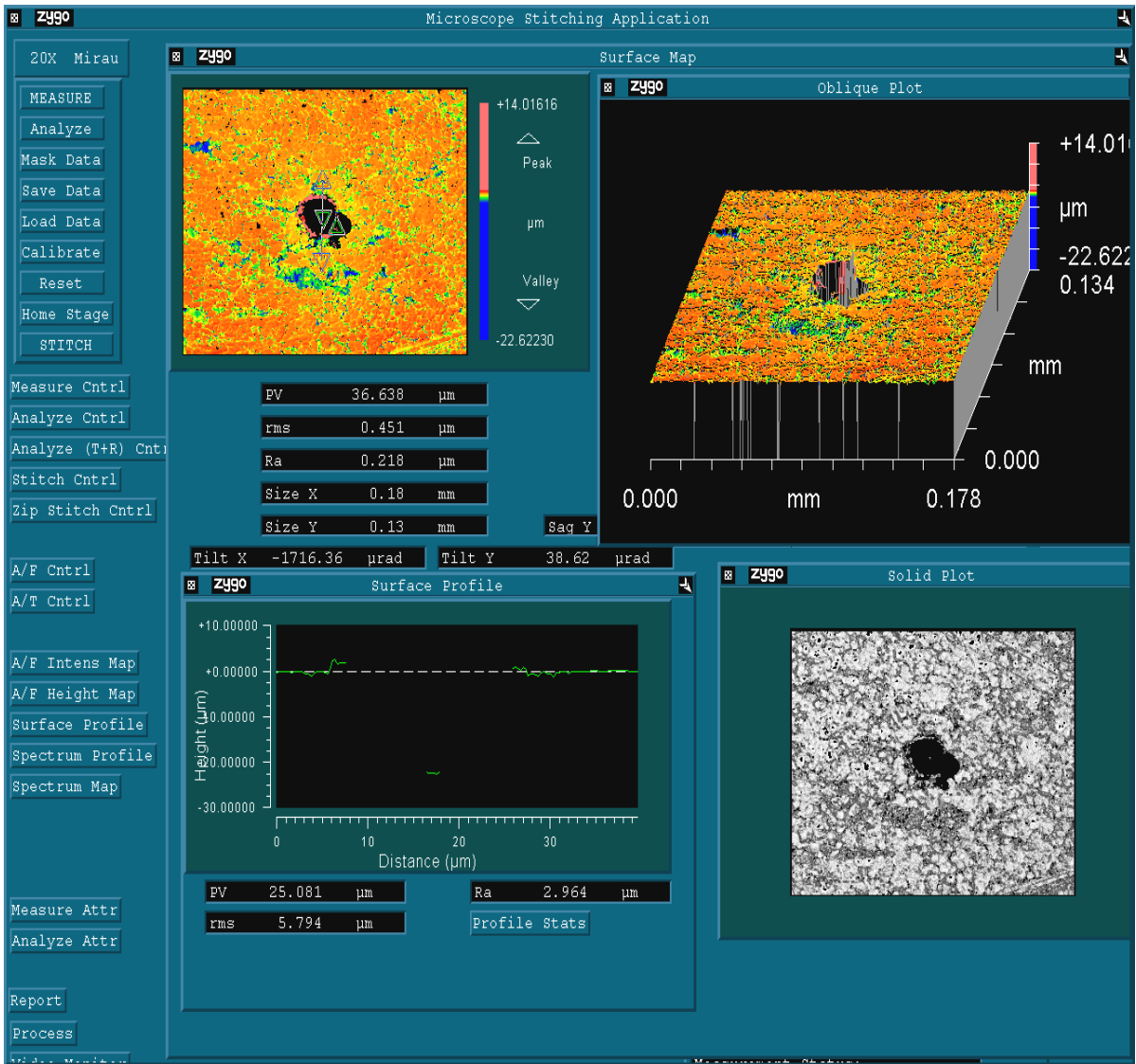


Figure 10.17: Zygo hole profile data for 20 μs pulse width

The spot was then tested with the Talysurf Stylus Profilometer as well to verify the results. The results (figure 10.18) from this test also showed that there was at least a 20 μm deep hole though the diameter was different most likely because the stylus did not pass directly through the center of the hole.

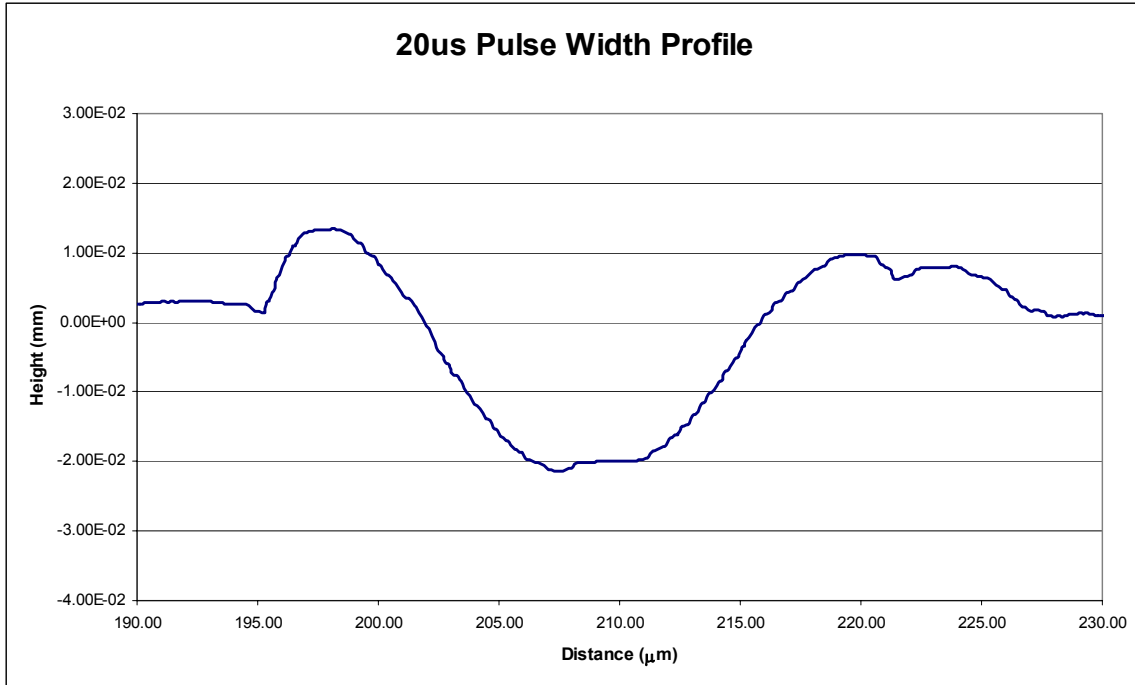


Figure 10.18: Talysurf surface profile for 20μs pulse width hole

The 30μs pulsing test also produced a hole, but this time it did occur at the optimal focal position. Figure 10.19 shows the partial results of this with the center image being the spot where the actual hole was created.

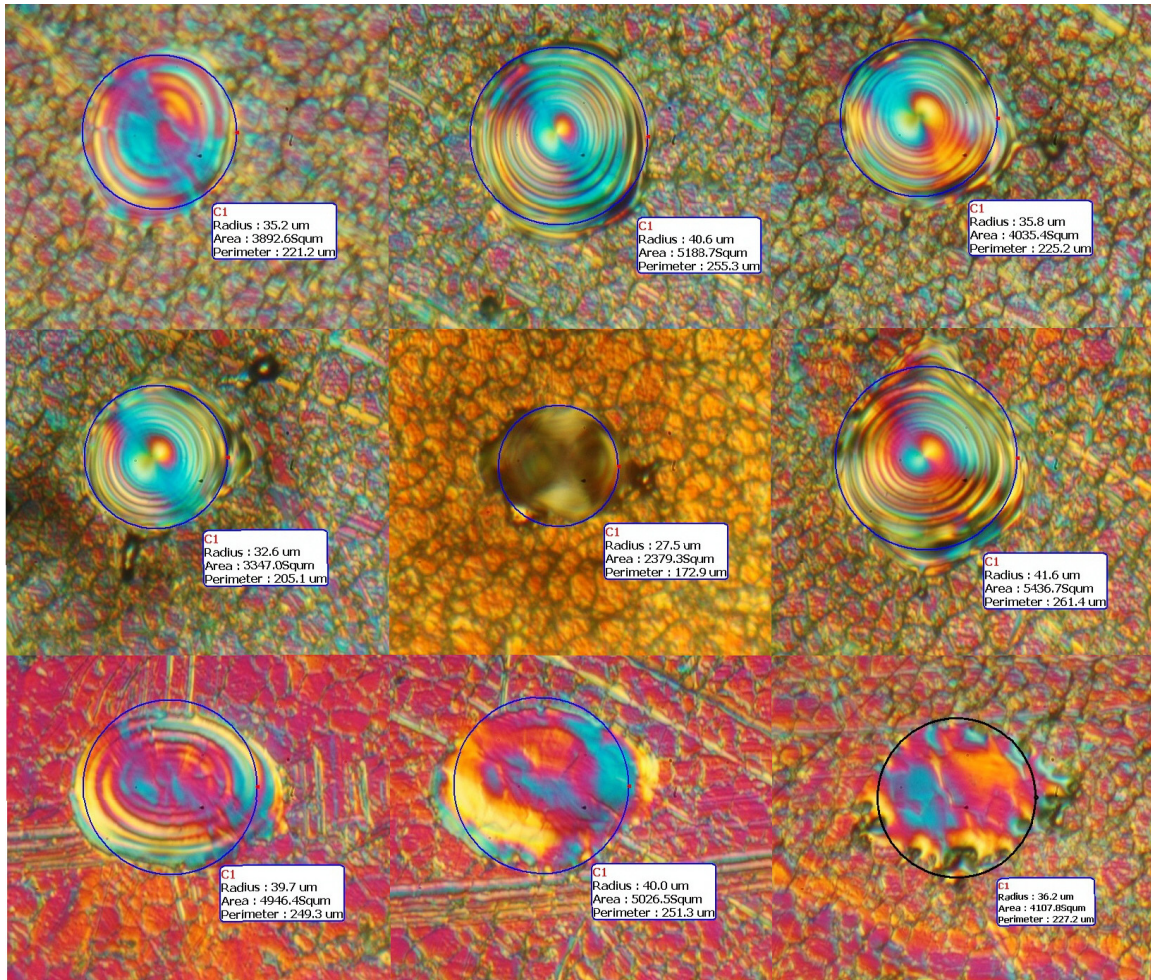


Figure 10.19: Spot images for 30us test, starting with the top left and going left to right in each row

The enlarged view of the hole is shown in figure 10.20 and the hole depth was estimated by the microscope to be about 20μm.

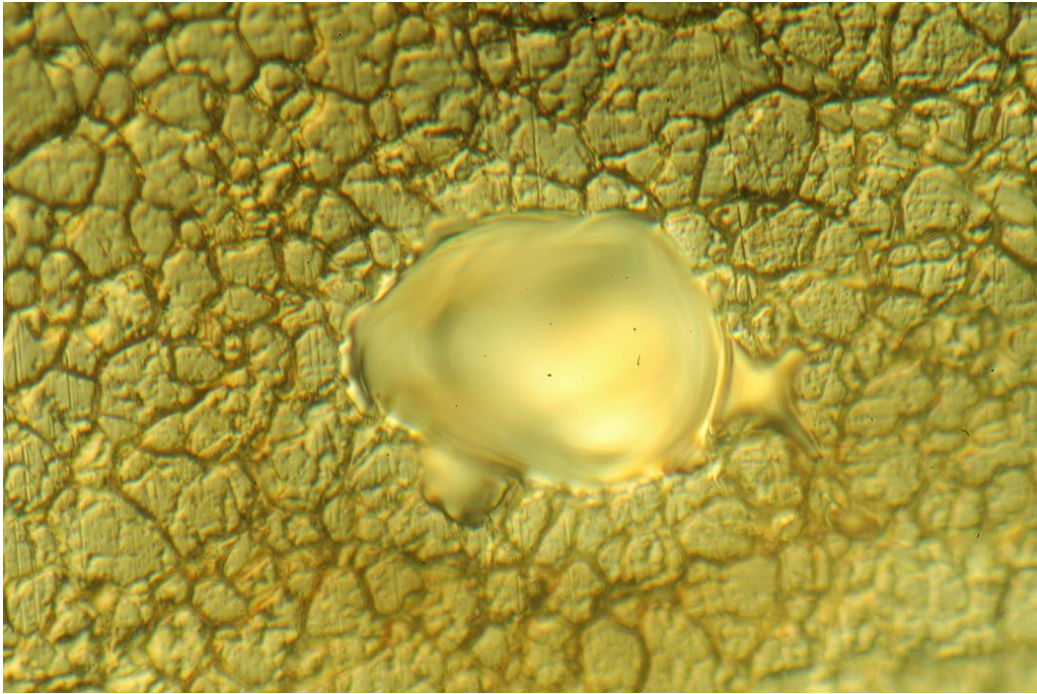


Figure 10.20: Enlarged hole image for 30 μ s test, 40X objective

The Zygo Interferometric Microscope was then used to measure the 3D hole profile. This time the profile was slightly more detailed showing more of the contour. The hole depth shown in figure 10.21 was about 19 μ m while the hole diameter was approximately 60 μ m. The measured diameter from the microscope was close to this at 55 μ m. The discrepancy between the two is most likely due to the difficulty of measuring non-round holes on the microscope. To validate these measurements the Talysurf profilometer was used once again. Figure 10.22 gives the profile plot in which it also discloses that the hole depth is a little over 18 μ m with a diameter of about 60 μ m.

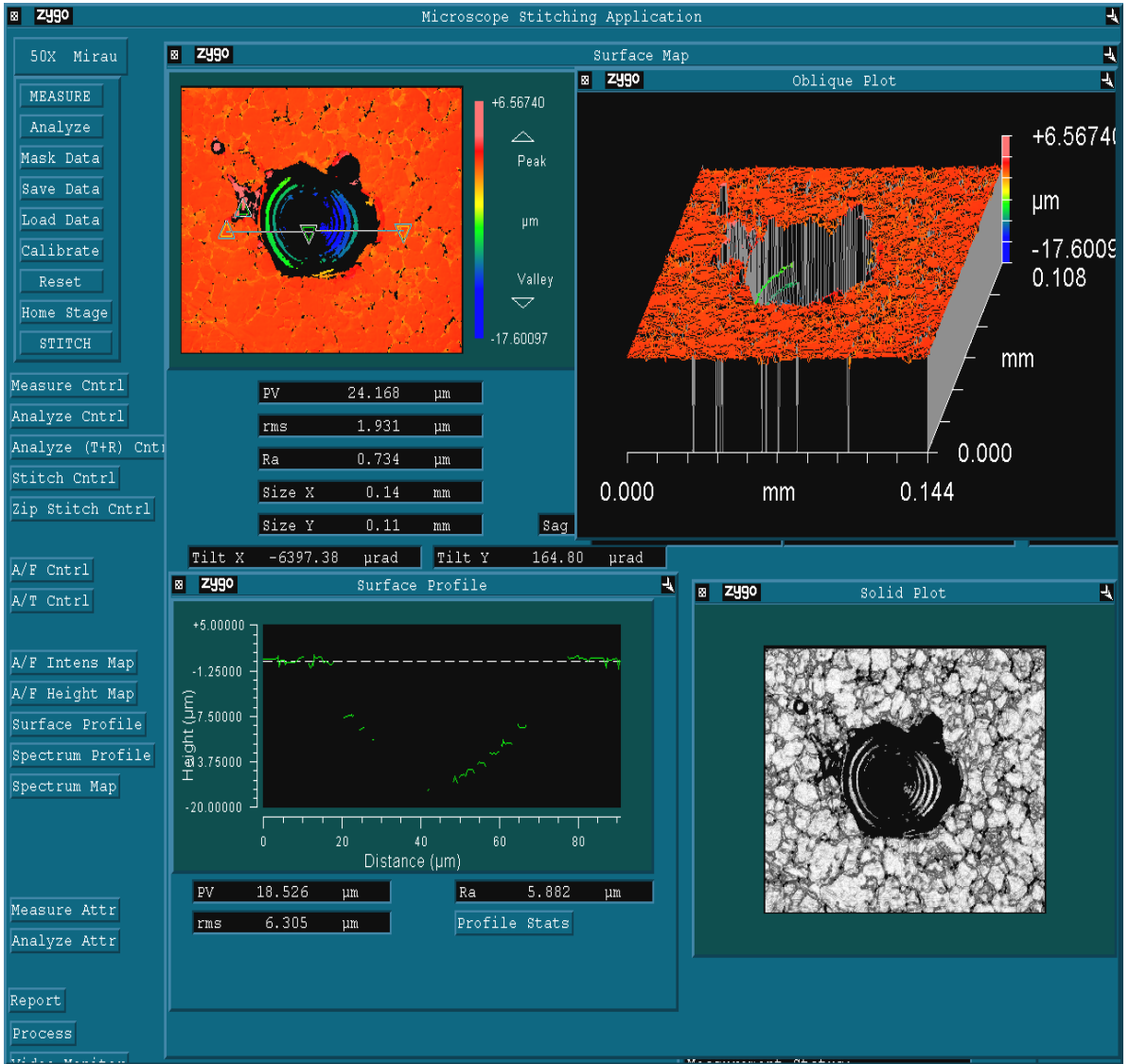


Figure 10.21: Zygo hole profile data for 30 μs pulse width

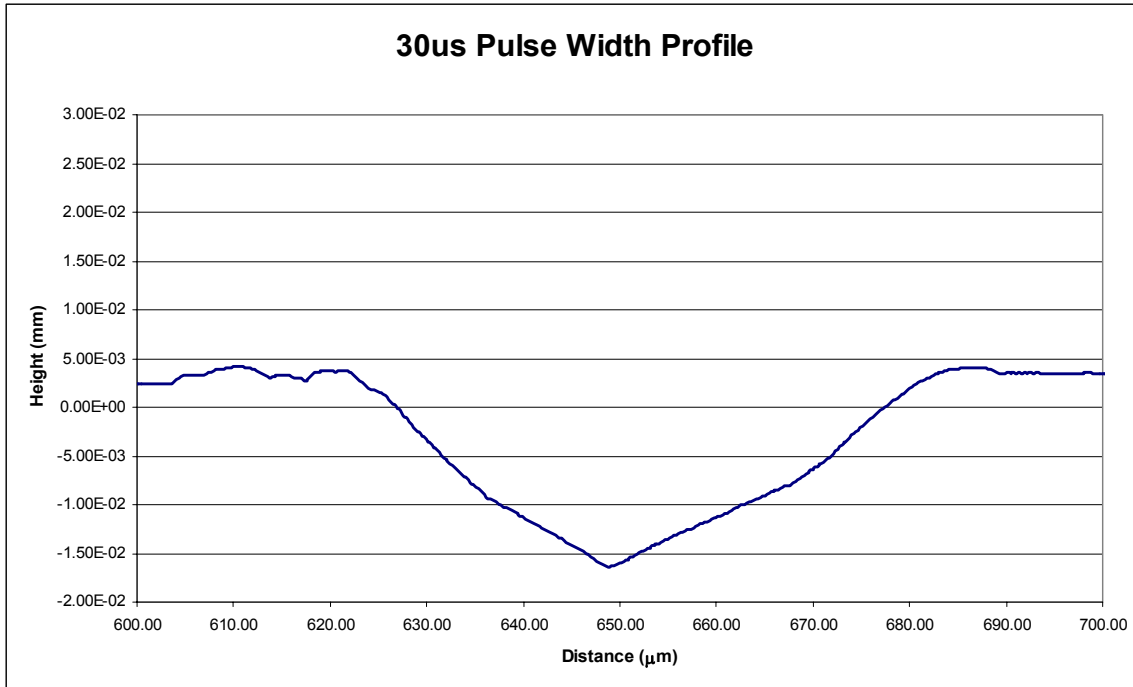


Figure 10.22: Talysurf hole profile for 30μs pulse width

Finally the 40μs pulsing test was examined and as in the 20μs test it also revealed that the optimal focal position did not produced the hole. Further testing would have to be committed to determine whether focusing into the plane is more effective, but this most likely is due to a problem in the fixturing not holding the piece perfectly flat. As can be seen from figure 10.23 the larger pulse width created significantly larger holes, though the roundness of them was better than the smaller pulse width tests. It is expected though that after multiple pulses the smaller pulse width schemes will produce holes of equal roundness. Figure 10.24 shows an enlarged image of the nicely rounded hole produced. The Zygo Interferometer was then used to measure the holes profile. It was hoped that the larger hole with a less steep profile would yield more detailed results, but this was not the case. There was enough data though to estimate the hole depth to be 18μm. From figure 10.25 the hole's diameter appears to be around 42μm which is close to the microscope's value of 45.0μm. Many attempts were made to measure the hole on the Talysurf stylus profilometer, but were not successful. Nonetheless there was enough data from the Zygo Interferometer to analyze.

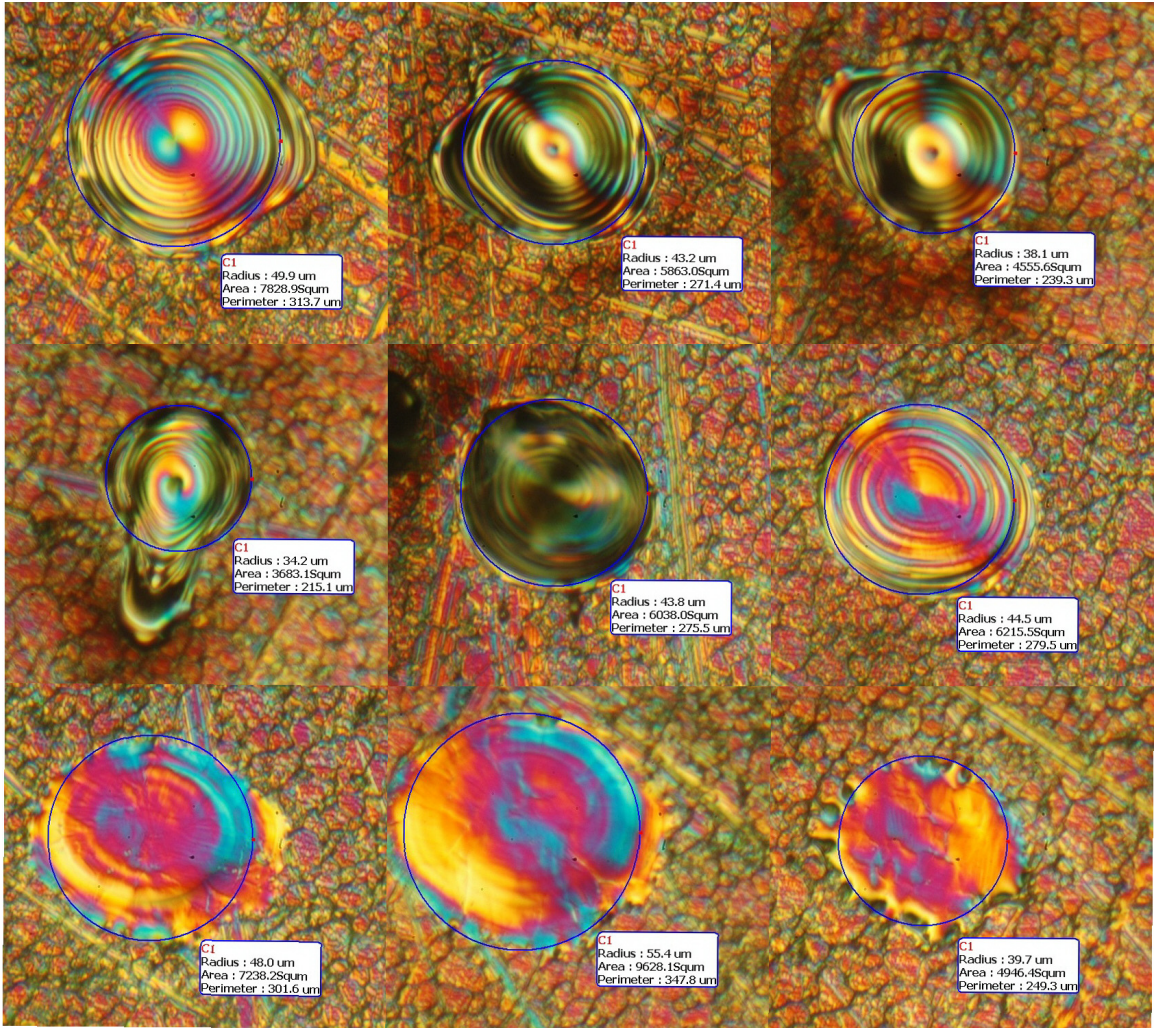


Figure 10.23: Spot images for 40us test, starting with the top left and going from left to right in each row

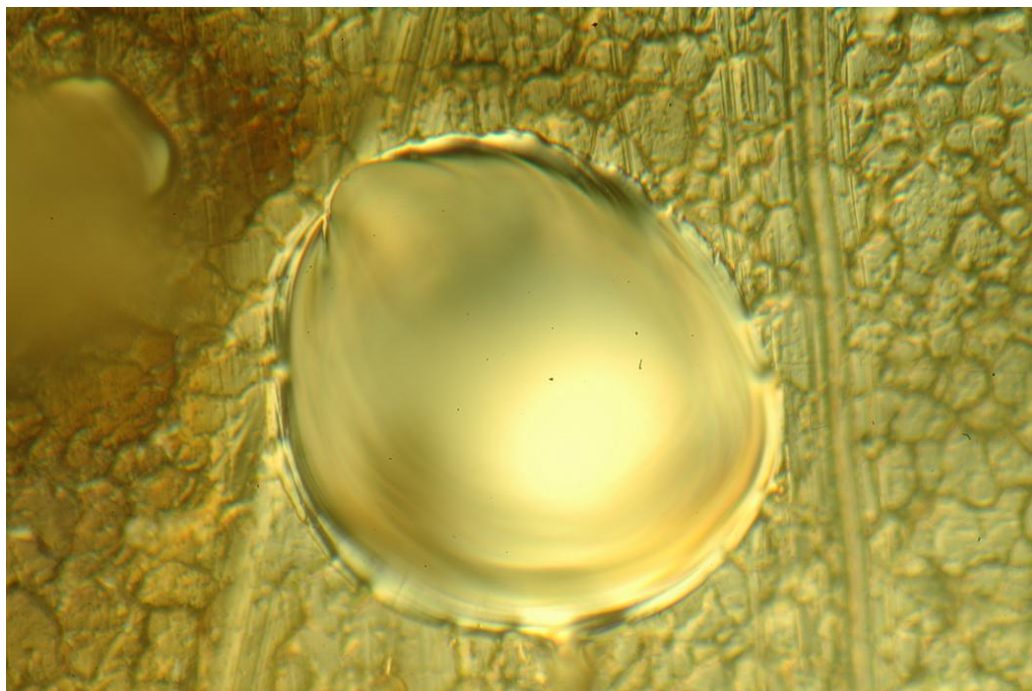


Figure 10.24: Enlarged hole image for 40µs test, 40X objective

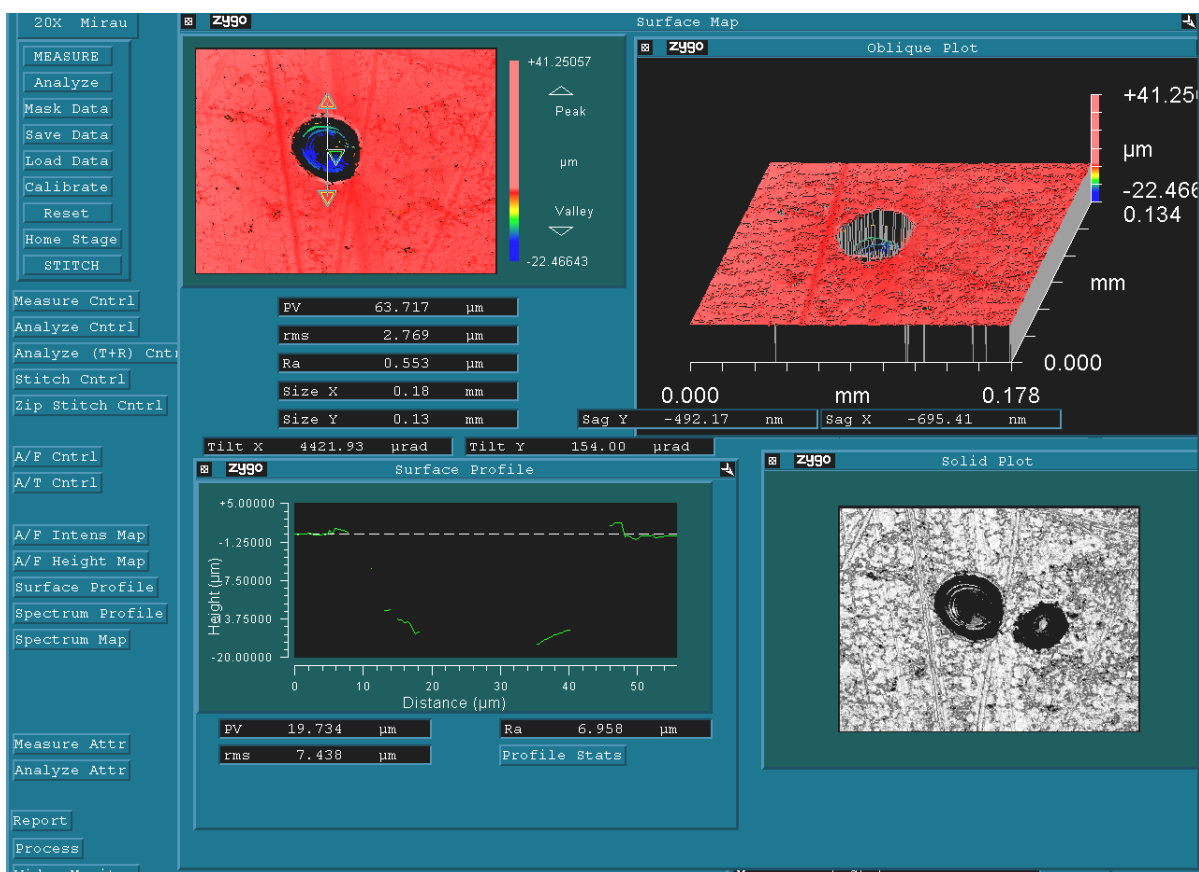


Figure 10.25: Zygo hole profile data for 40µs pulse width

A summary of the results is shown in table 10.2.

Pulse Width (μm)	Diameter (μm)	Depth (μm)
20	40.1	~24
30	45.0	~19
40	43.8	~18

Table 10.2: Summary of successfully drilled holes

It's fairly obvious from the results that the $20\mu\text{s}$ pulsing would be the best out of these choices. The first reason would be that it produced the smallest diameter hole. The second reason is that it produced the greatest depth and therefore had the highest material removal rate (MRR). Both of the results are most likely due to the shorter pulse time allowing for less conduction. It appears that the larger pulse widths allowed for more heat conduction through the surrounding area which caused melting instead of ablation, thus some of the molten material re-deposited in the hole. It is now even more evident that the initial spike in power of the laser is what is causing the ablation where the rest of the pulse at 300W is resulting in melting (figure 10.26).

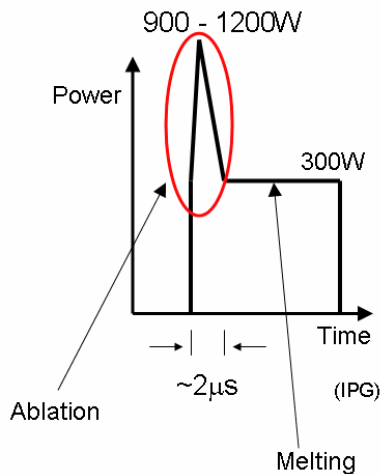


Figure 10.26: Enhanced Pulse Analysis (IPG)

Figure 10.27 shows a summary of the hole characteristics created for each of the pulse durations. These are not to scale and the characteristics are exaggerated to help demonstrate their differences. The $20\mu\text{s}$ pulse showed that it produced the smallest diameter hole with the greatest depth. However from the enlarged images it showed that

it also produced the largest recast layer. Moving onto the 30 μ s pulse it produced a larger diameter whole, smaller depth and had less of a recast layer. The smaller depth and recast layer suggests that the longer pulse allowed for more melting around the perimeter of the hole which reduced the recast layer and slightly enlarged the diameter.

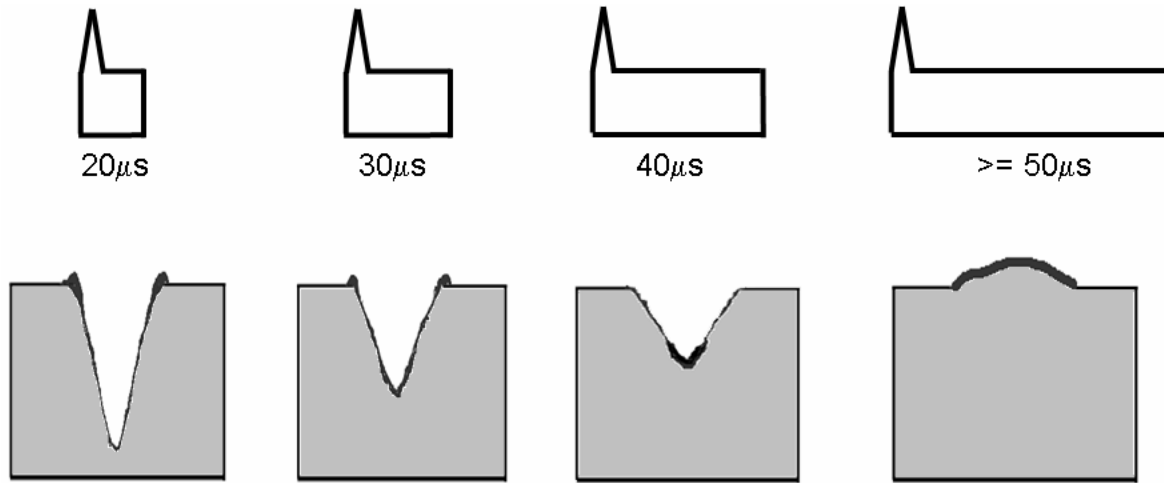


Figure 10.27: Hole Characteristics Diagram for Various Pulse Width Tests (Not to scale)

The melted material then re-deposited in the hole and in turn reduced the depth of the indentation. The same can be seen for the 40 μ s pulse test where even less of a recast layer was found and hole produced had a smaller depth. Finally for pulse widths of 50 μ s no hole was produced because of the excessive melting that occurred, creating liquid voids. After cooling, these voids created an area of less dense material which resulted in a bump instead of an indentation. These effects can be seen from the profile data in figures 10.9, 10.17, 10.18, 10.21, 10.22, and 10.25.

Some of these trends have been observed by similar research in that thresholds were found to exist for the removal of material. (Yashikar,2002) The threshold for this setup was found to be somewhere in between 50 μ s and 40 μ s at which there will be minimal to no material removal. This study also showed the same trend in increasing crater depth with decreasing pulse time and confirmed that there is a limit to the effectiveness of reducing pulse width.

10.5 Sub 20 μ s Pulse Tests

To determine the effect of reducing the pulse width beyond 20 μ s an external pulse generator circuit was created. Due to software limitations pulses under 20 μ s were not possible with the current setup, but using the circuit shown in appendix 14.10, pulse widths of 3.7 μ s and larger were achievable. An initial test was done with using a 10 μ s pulse width. When the piece was examined it was determined that there was no mark made, possibly suggesting a limitation for the laser. A new test was performed at the optimally focused position using pulse widths from 20 μ s down to 10 μ s. Marks were found on the specimen for pulse durations of 15 μ s and larger. Figure 28 shows the enlarged images of the holes created in the specimen. The holes were created over a marker line to increase visibility, thus the reason for the difference in contrast between the specimen surface and the indentions.

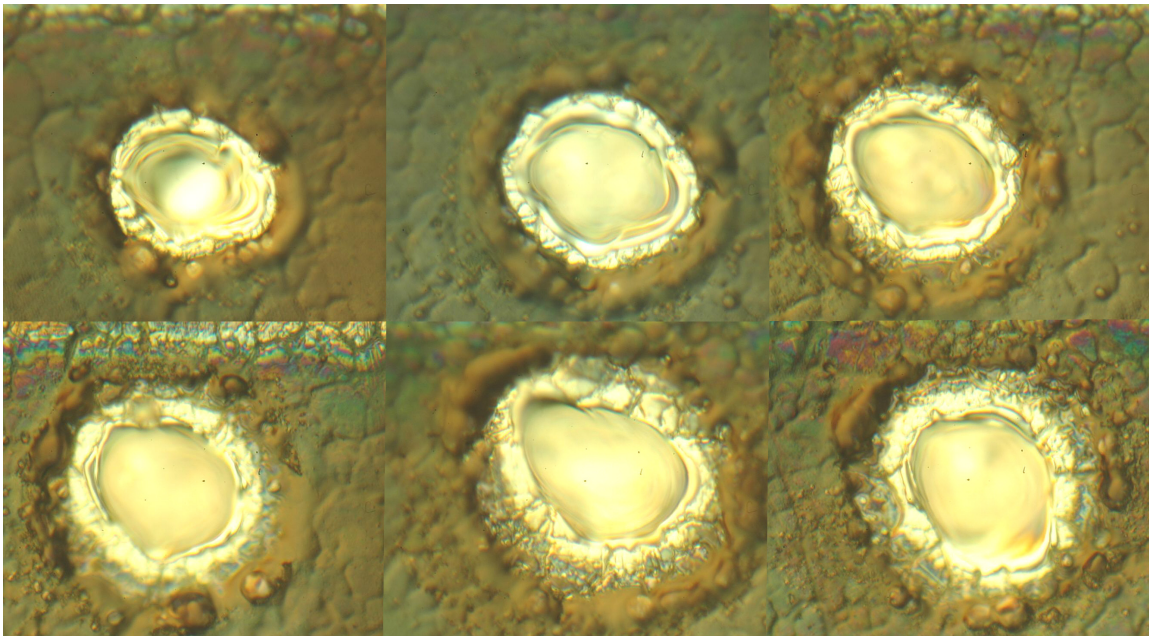


Figure 10.28: Enlarged Images for Sub 20ms Pulses (Shortest from left to right starting with top)

The blind holes that were produced were measured on the microscope and brought to the precision engineering center where once again where they were measured by the Zygo NewView 5000 Interferometric microscope. The Zygo Images are shown in figures 10.29-10.34. Due to the incompleteness of the plots and the magnification used on the

Interferometer the diameters can not be accurately be read from the figures, only the depths. Note that the small depth in the results for the 18 μ s pulse test (figure 10.31) was corrected using repeated tests and the calibrated microscope. This was most likely due to a focusing error in the area where the 18 μ s pulse was performed.

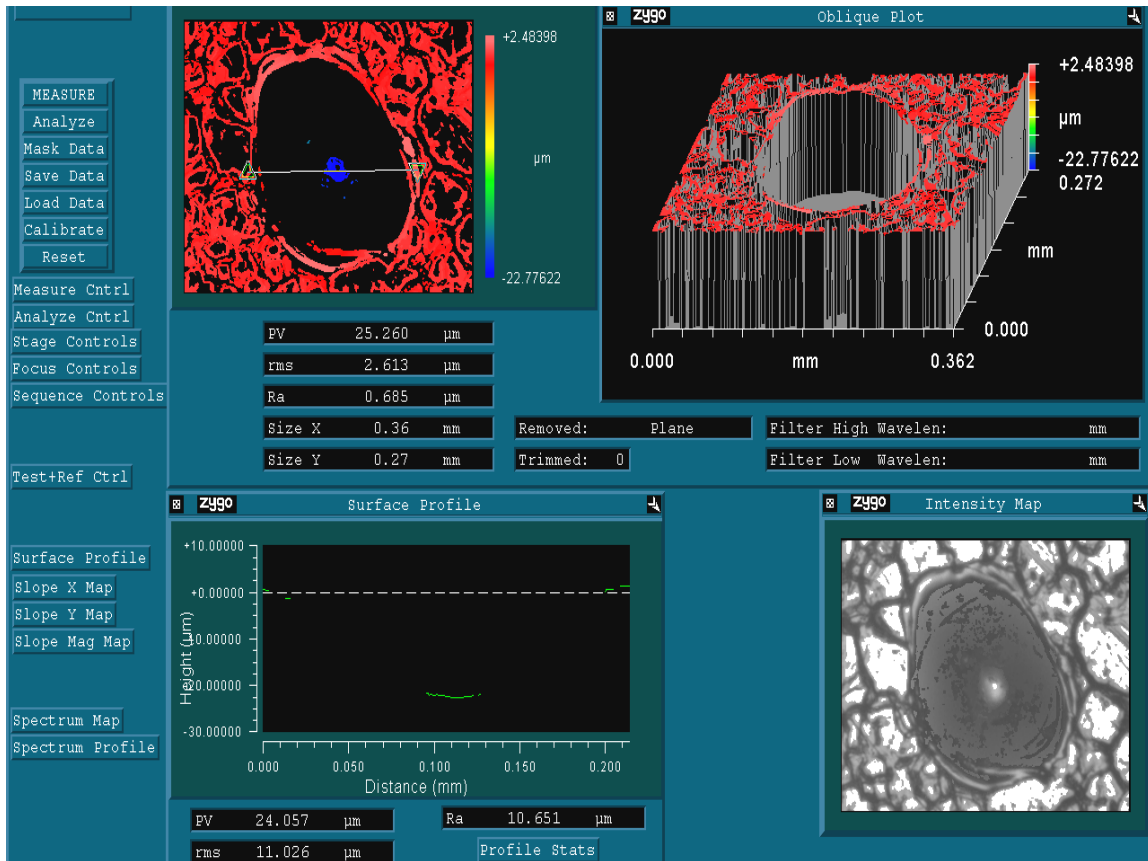


Figure 10.29: Depth Measurement for 20 μ s Pulse Test

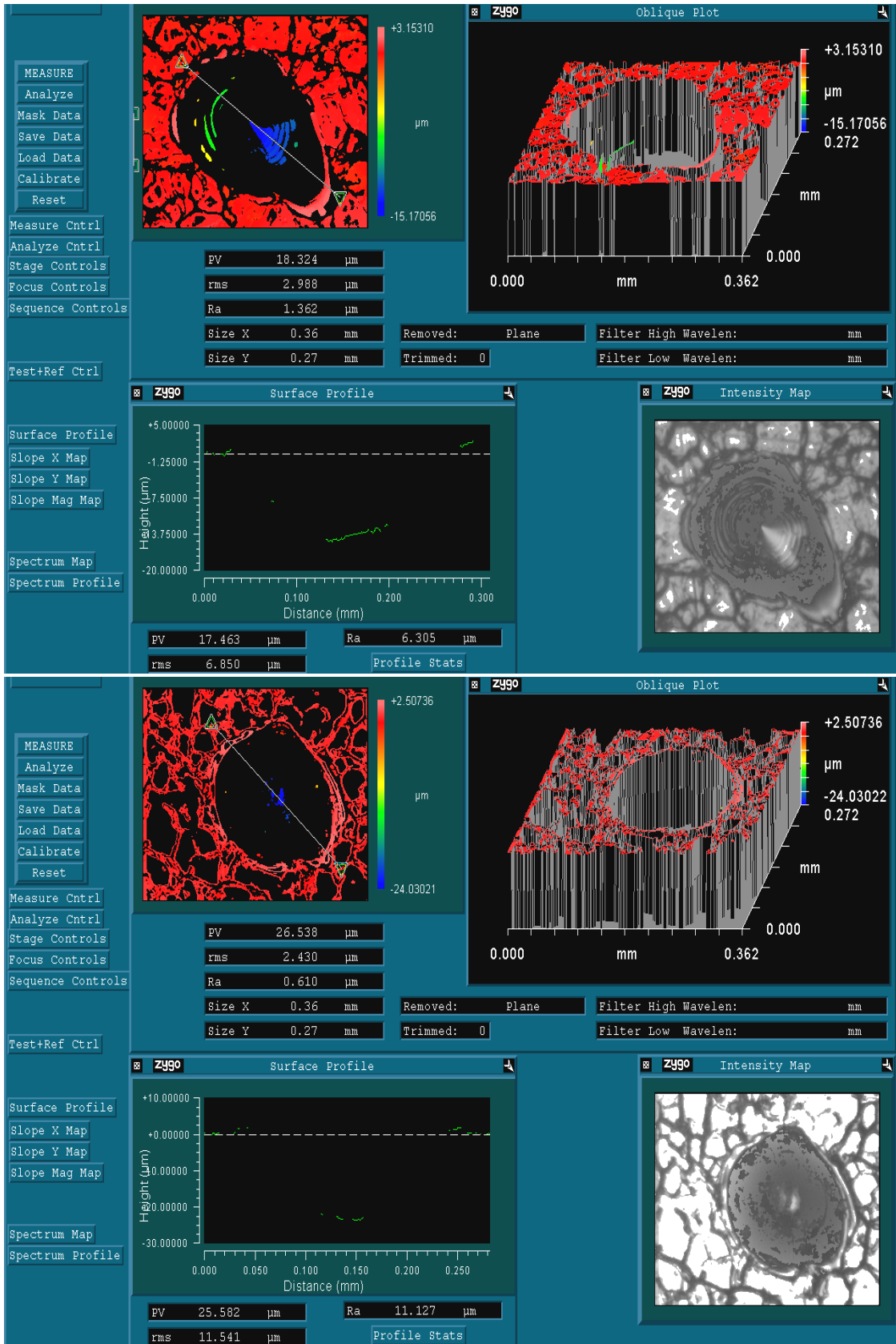


Figure 10.30: Top – 19µs Pulse

Figure 10.31: Bottom – 18µs Pulse Results

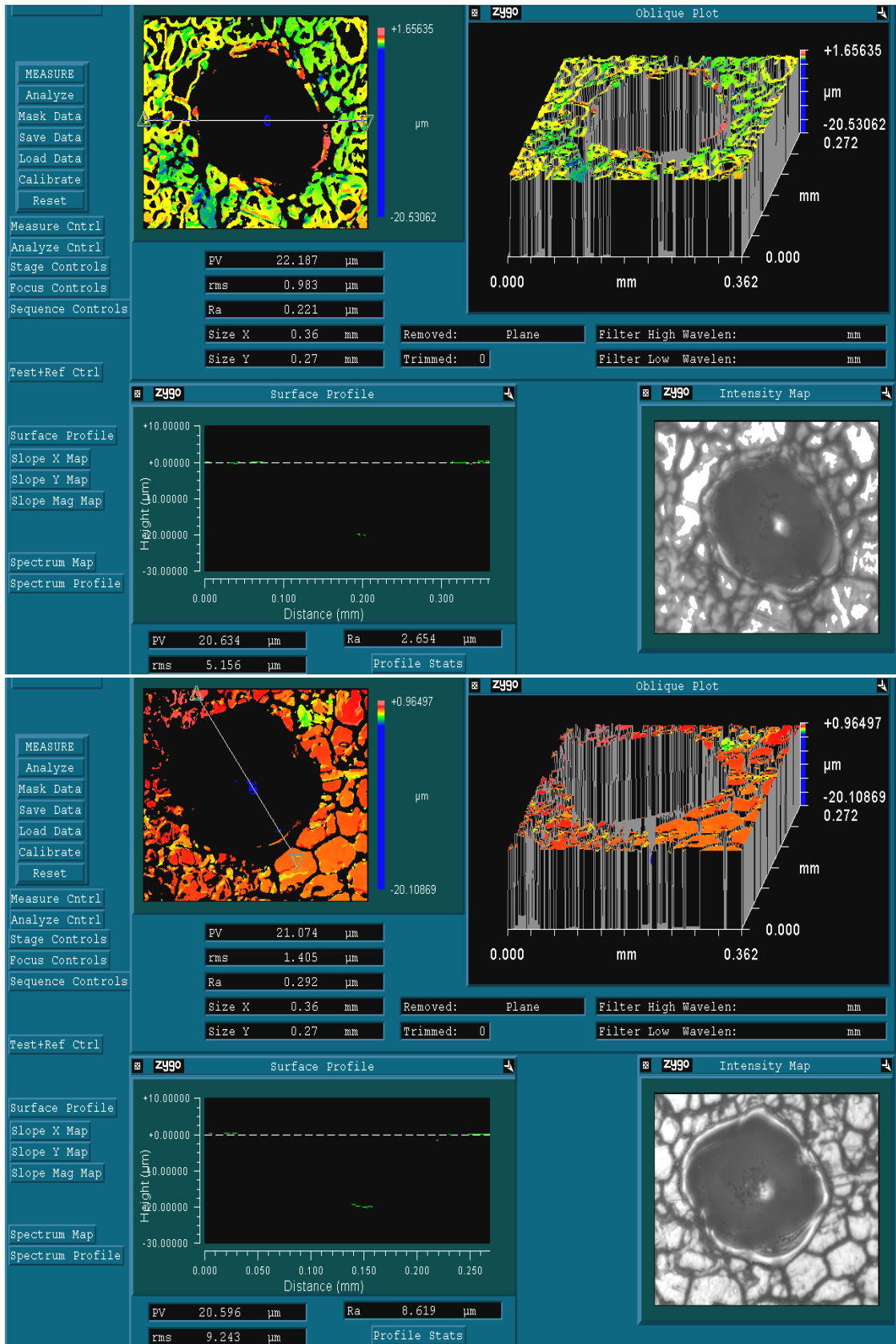


Figure 10.32: Top – 17µs Pulse

Figure 10.33: Bottom – 16µs Pulse Results

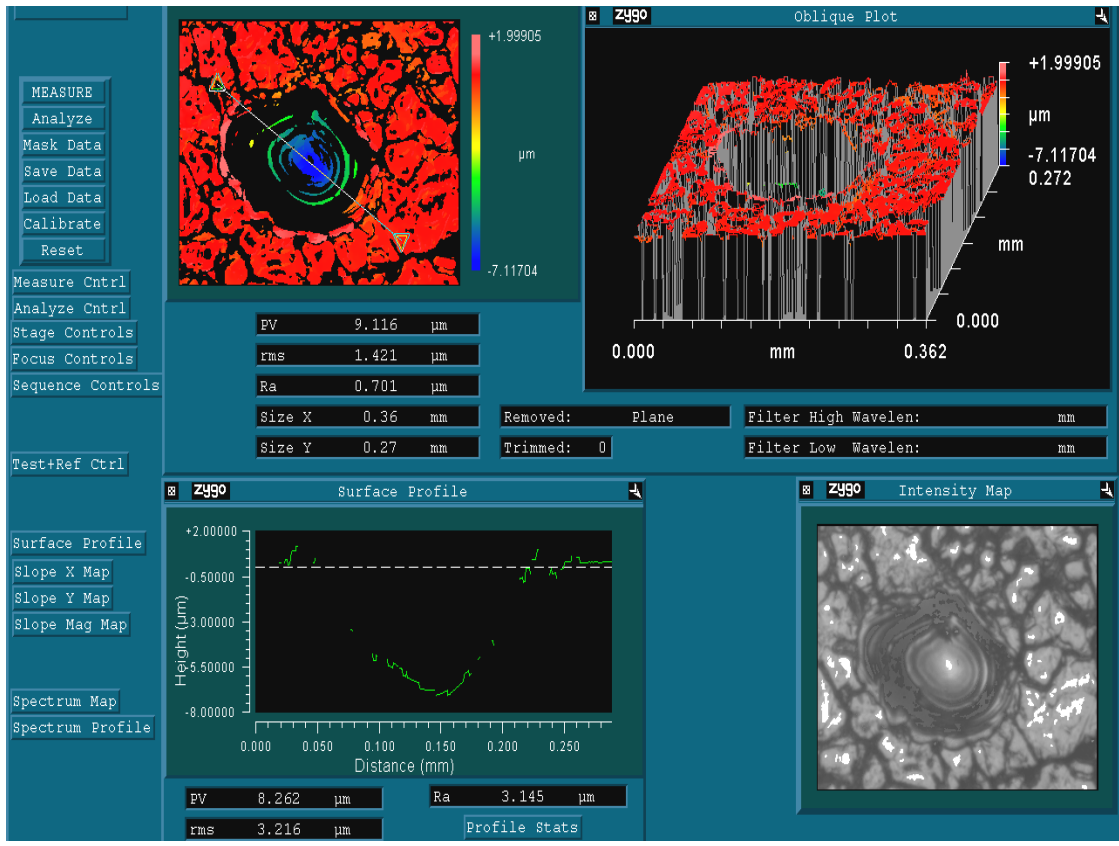


Figure 10.34: Depth Measurement for 15µs Pulse Test

Figure 10.35 shows a summary of the measurements for the holes.

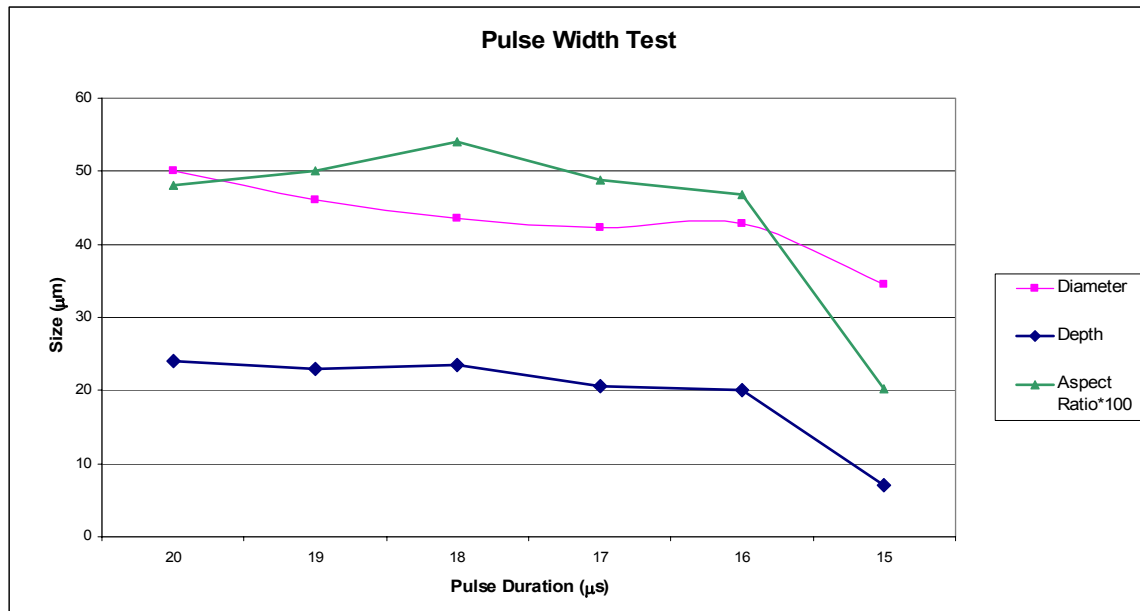


Figure 10.35: Plot of Hole Characteristics for Various Pulse Widths

From the plot it shows that both the diameter and the depth of the blind holes tend to decrease in size with lowering pulse width. It was hoped that decreasing the pulse width further would decrease the amount of melting due to the lower power density at 300W, and therefore would increase the depth of the indentation. Since this was not the case, and the depth significantly decreased at 15µs and no mark is noticed beyond that suggests that the form of the enhanced pulse may be slightly different than originally thought. Instead of what is shown in figure 10.36 the enhanced pulse may look more like figure 10.37. Since no mark is produced for pulse durations under 15µs it appears that there is a ramping up of the power, thus at 14µs there is not enough power density to cause a mark.

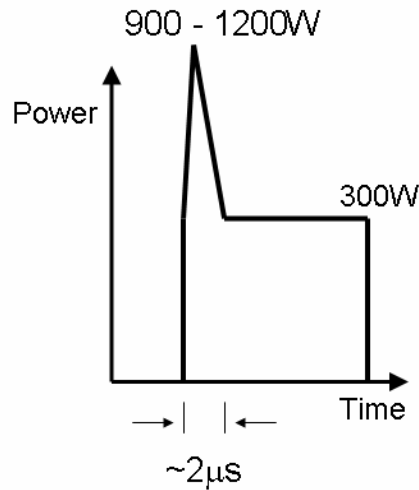


Figure 10.36: Original Form of Enhanced Pulse (IPG)

At $15\mu\text{s}$ however the spike is rapidly starting to generate and there is sufficient power to create a hole. Increasing the pulse duration further allowed for more of the spike to be established, thus causing more ablation resulting in a deeper hole.

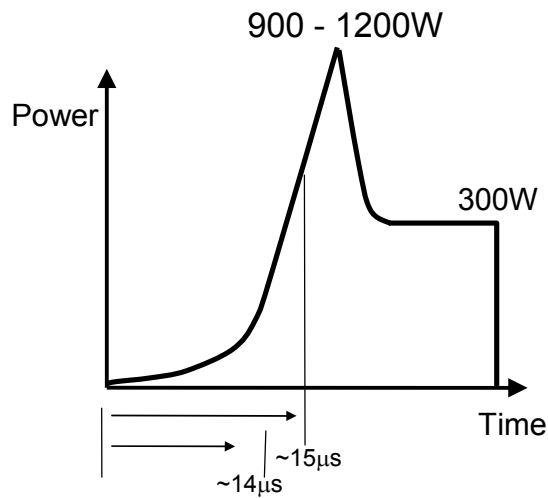


Figure 10.37: Predicted Form of Enhanced Pulse from Experimentation

Though the highest depth was achieved at a $20\mu\text{s}$ pulse, the highest aspect ratio from figure 10.35 was found to be at $18\mu\text{s}$. This pulse width had only slightly less depth than the larger pulse widths, but had a significant reduction in diameter which helped to increase the aspect ratio.

10.6 Results comparison

From the results given in this thesis it was determined that the spot size and pulse width can greatly effect the outcome. With a spot size of $10.8\mu\text{m}$ and a pulse width of $50\mu\text{s}$, it was not possible to produce holes with the available power. Changing the lens allowed for a smaller spot size which in turn raised the power density, a key factor when trying to create ablation. Finally, lowering the pulse width increased the prominence of the spike in power from the enhanced pulse and also reduced the conduction through the material.

	Normal YLR-300 100mm lens	Enhanced YLR-300 100mm lens	YLR-300 60mm lens	Nd: YAG Nano	Ti:Sapphire Pico	Ti:Sapphire Femto
Pulse Width (sec) :	1.80E-05	1.80E-05	1.80E-05	3.80E-08	3.50E-11	1.30E-13
Energy (J) :	5.40E-03	6.60E-03	6.60E-03	6.00E-04	1.00E-04	7.50E-04
Peak Power (W) :	300	1200	1200	15,789	2,857,143	5,769,230,769
Spot Size (μm) :	7.2	7.2	4.32	30	40	150
Fluence (J/cm^2) :	13,263	16,210	45,028	85	150	0.5
Power Density (GW/cm^2) :	0.737	2.947	8.187	2.23	227.4	32,647
Removal Rate :	N/A	24 μm /pulse	?	1.5 μm /pulse	0.3 μm /pulse	0.1 μm /pulse
Repetition Rate :	15kHz	15kHz	15kHz	10 kHz	100 kHz	5 kHz

Table 10.3: Typical parameters for different laser systems

Changing both of these parameters allowed for the creation of a crater with less than $50\mu\text{m}$ in diameter. As desired the resulting hole also contained a very small heat affected zone even though the pulse time was substantially larger than that of ns, ps, and fs-short pulse lasers. Table 10.3 shows the typical parameters for the 300W Fiber laser along the parameters for the 3 classes of short pulsed lasers.

The addition of the 100mm lens and the enhanced pulsed allowed for the power density to approach that of the typical nanosecond laser. Because they have higher order modes, or lower beam qualities, the short pulsed lasers minimum spot size is much larger than the fiber laser. This can limit the size of the holes that they can create. The MMR produced for the single pulse of $20\mu\text{s}$ was very high at a value of $24\mu\text{m}$. The typical MMR for short pulse lasers is two orders magnitude smaller than the value obtained with the CW laser. Though the pulse times are much smaller for the short pulse lasers, the rest

time needed in between pulses is larger than what is needed for the CW laser. Therefore since the MMR is so much lower for the short pulsed lasers, it would take somewhere around 100 pulses to create the same depth as 1 pulse from the CW laser. The off time needed for these short pulsed lasers creates a bottleneck making the overall process take longer.

10.7 *Benchmark Revisited*

Earlier in section 7 of this paper a benchmark using a picosecond laser drilled specimen was discussed. The 137 μm thick specimen was drilled using a 13ps pulse which created an exit hole 100 μm in diameter. Using the typical removal rate for a picosecond laser, this would mean that well over 300 pulses were needed to create this through hole. With one 18 μs pulse of the fiber laser a blind hole was created with half the diameter of the benchmark specimen and a depth of about 24 μm . This could possibly mean that only about 6 pulses from the fiber laser would be needed to produce a through hole in the same specimen. Of course this would have to be verified by further tests using multiple pulses.

11 CONCLUSIONS

The results show that laser ablation occurs when a 100mm lens is used with pulse durations at 40 μ s or below. At 20 μ s pulse duration, a blind hole of 42.8 μ m diameter and 24 μ m depth can be created with little heat affected zone. This performance is comparable to nanosecond, but with much higher hole depth per pulse. It was also found that the pulse duration must be less than 50 μ s so that the ablating effect of the initial spike of an enhanced pulse is not nullified. At longer pulse durations (50 μ s or more), raised surfaces are created instead of holes.

From the results and future testing it is therefore possible that this laser could be used for multiple types of material processing with decent results compared to of the application specific lasers used. Besides some of the benefits listed earlier such as the small spot size, high MRR, and versatility of the fiber laser, there are additional advantages that it possesses over ultra-short pulse lasers. For one the initial cost of a fiber laser of this kind is less than 1/8th the cost of a ultra-short pulse laser. It also demands less electrical power, one reason being that its wall plug efficiency is on the order of 20-25% where ultra-short pulse lasers tend to be around 5%. The footprint of this fiber laser is around 4 sq.ft. where many of the other laser systems can be over 30 sq.ft. Finally there is practically no maintenance needed for the fiber laser unlike ultra-short pulse lasers that have mirrors that need to be aligned and replaced, or diodes that need replacing because they have less than 1/5th the life of the fiber laser's diodes.

12 FUTURE WORK

Though the research performed yielded valuable results there are several aspects that were either not examined or could be bettered. One clear improvement that can be made is the implementation of a new fixture for holding the piece. A fixture that could hold the piece more uniform and straight would greatly help the repeatability of the tests and would allow for less retesting.

Another fairly obvious inquiry would be to perform drilling tests using the 60mm focusing optic since it would more than double the current power density. However this is very dependent on having a good fixture due to the high sensitivity of focusing.

Now that ablation was proved possible with the fiber laser a study of the optimal operating parameters could be undertaken to produce desired characteristics such as minimum diameter, maximum penetration depth, roundness, hole quality etc. Some of these parameters include assist gas pressure, assist gas angle, and pulse time. The implantation of coatings on the material such as mentioned in the literature section could help with certain characteristics.

Finally since focusing is so important it would be possible to look into applying an active focusing scheme. A better fixture may allow for the errors in the part to be minimized, however errors in the surface can still exist. This can also be applied to a manufacturing situation where everything being worked on is the same shape and size. Some possibilities for measuring surface deviations would be laser interferometry where the guide beam could possibly be used as the source laser. Servo motors using feedback from the measurement system could reposition the part or optics assembly to the needed height. Piezo actuators could be used in instances where very small height changes were needed with high response time.

These results and future testing will possibly show how low power CW single mode fiber lasers can provide results on par with nanosecond and picosecond short pulsed lasers

when producing micro holes. However there still may be limitations that have not yet been discovered. If this proves to be true then this laser system could provide a good alternative to the very expensive short pulse laser systems on the market. The higher average power of this laser system may also prove to be beneficial for macro processing of materials, thus making it not only a cheaper alternative, but a versatile one at that.

13 REFERENCES

- 1) Andrews, J.G. and Atthey, D.R., 1975, "On the motion of an intensely heated evaporating boundary," *Journal of the Institute of Mathematics and Its Applications*, **Volume 15**:p.59-72.
- 2) Charschan, S.S., 1993, *Guide to Laser Materials Processing*, 1st Edition, Laser Institute of America, Orlando, p.40-41.
- 3) Corcoran, A., Sexton, B., Seaman, B., Ryan, P., and Byrne, G., 2001, "The laser drilling of multi-layer aerospace material systems," *International Journal of Material Processing Technology*, **Volume 123**:p.100-106.
- 4) Crafer, R.C., Oakley, P.J., 1993, *Laser Processing in Manufacturing*, 1st Edition, Chapman & Hall, London.
- 5) Domankevitz, Y., Kwok, H.S., and Copley, J.A, 1995, "A laser device for perforating materials," *Review of Scientific Instruments*, **Volume 66** no. 12:p.5642-5643.
- 6) Feifer, A., 1989, "A Drilling micro-size deep holes," *Tooling and Production*, **Volume 55** no. 7:p.58-60.
- 7) Friedrich, C., 1998, "Laser Micromachining – Laser Ablation," Michigan Technology University Notes
- 8) Ganesh, R.K., Faghri, A. and Hahn, Y., 1997, "A generalized thermal modeling for laser drilling process-I. Mathematical modeling and numerical methodology," *International Journal of Heat and Mass Transfer*, **Volume 40** no. 14:p.3351-3360.

- 9) Ganesh, R.K., Faghri, A. and Hahn, Y., 1997, "A generalized thermal modeling for laser drilling process-II. Numerical simulation and results," *International Journal of Heat and Mass Transfer*, **Volume** 40 no. 14:p.3361-3373.
- 10) Ghoreishi, M., Low, D.K.Y, and Li, L., 2002, "Comparative statistical analysis of hole taper and circularity in laser percussion drilling," *International Journal of Machine Tools & Manufacture*, **Volume** 42:p.985-995.
- 11) Guo, D., Cai, K., Yang, J., and Huang, Y., 2002, "Spatter-free laser drilling of aluminum ceramics based on gelcasting technology," *Journal of the European Ceramic Society*, **Volume** 23:p.1263-1267.
- 12) Kleine, K.F., Whitney, B., and Watkins, K.G., 2002, "Use of Fiber Lasers for Micro Cutting Applications in the Medical Industry," *Proceedings of ICALEO*
- 13) Low, D.K.Y, Li, L., and Byrd, P.J., 2003, "Spatter prevention during the laser drilling of selected aerospace materials," *Journal of Materials Processing Technology*, **Volume** 139:p.71-76.
- 14) Low, D.K.Y, Li, L., Corfe, A.G., and Byrd, P.J., 2000, "Spatter-free laser percussion drilling of closely spaced array holes," *International Journal of Machine Tools & Manufacture*, **Volume** 41:p.361-377.
- 15) Modest, M.F., Abakians, H., 1986 , "Evaporative cutting of a semi-infinite body with a moving CW laser," *ASME Journal of Heat Transfer*, **Volume** 108:p.602-607.
- 16) Modest, M.F., 1996 , "Transient model for CW and pulsed laser machining of ablating/decomposing materials-approximate analysis," *ASME Journal of Heat Transfer*, **Volume** 118:p.774-780.

- 17) Murayama, R., Ohmura, E. and Miyamoto, I., 1998, "Thermohydrodynamic Analysis for Bump Formation in Laser Texturing," *Proceedings of ICALEO*
- 18) Ng, G.K.L., and Li, L., 2002, "Repeatability characteristics of laser percussion drilling of stainless-steel sheets," *Optics and Lasers in Engineering*, **Volume** 39:p.25-33.
- 19) Ohmura, E., Fukumoto, I., 1996, "Molecular Dynamics Simulation on Fusion and Vaporization of Metals and Silicon Due to Laser Irradiation," *Seiken Symposium*, **Volume** 18:p.255-265.
- 20) Ready, J.F., 1997, *Industrial Applications of Lasers*, 2nd Edition, Academic Press, San Diego, p.387-395.
- 21) Rodden, W.S.O., Kudesia, S.S., Hand, D.P., and Jones, J.D.C., 2002, "A comprehensive study of the long pulse Nd:YAG laser drilling of multi-layer carbon fibre composites," *Optics Communications*, **Volume** 210:p.319-328.
- 22) Sohn, A., *Metrology in Precision Manufacturing: Laboratory Notebook*, 2005
- 23) Solana, P., Kapadia, P., Dowden, J.M. and Marsden, P.J., 1999, "An Analytical Model for the laser drilling of Metals with Absorption within the Vapour," *Journal of Physics D: Applied Physics*, **Volume** 32 no. 8:p.942-952.
- 24) Steen, William M., *Laser Material Processing*, 3rd Edition, Springer, Lond, 2003, p.335-341.
- 25) Tu, J, *Laser Drilling of Holes: A literature review*, Notes, Purdue University
- 26) Van Dyke, M., 1964, *Perturbation Methods in Fluid Mechanics*, Academic Press, New York.

- 27) Verhoeven, J.C.J., Jansen, J.K.M., Mattheij, R.M.M., 2002, "Modelling Laser Induced Melting," *Mathematical and Computer Modeling*, **Volume** 37:p.419-437.
- 28) Yilbas, B.S. and Sami, M., 1997, "Liquid ejection and possible nucleate boiling mechanisms in relation to the laser drilling process," *Journal of Physics D: Applied Physics*, **Volume** 30:p.1996-2005.
- 29) Yashikar, Y., 2002, "Laser Micromachining with Passively Q-switched Intracavity Harmonic Generator," *SPIE TD01*, p.462-466
- 30) Yilbas, B.S. and Sami, M., 1997, "Models for Solidification and Splashing in Laser Percussion Drilling," *SIAM Journal on Applied Mathematics*, **Volume** 62 no.6:p.1899-1923.
- 31) Zhang, Y., and Faghri, A., 1999, "Vaporization, melting and heat conduction in the laser drilling process," *International Journal of Heat and Mass Transfer*, **Volume** 42:p.1775-1790.
- 32) Zhigilei, L.V., Kodali, P.B.S, and Garrison, B.J., 1998, "A Microscopic View of Laser Ablation," *Journal of Physical Chemistry*, **Volume** 102:p.2845-2853.
- 33) Zweig, A.D., 1991, "A thermo-mechanical model for laser ablation," *Journal of Applied Physics*, **Volume** 70 no.3:p.1684-1691.

14 APPENDICES

14.1 *Connecting Gemini Servo Drives, Linear Motors and PCI Motion Controller*

Parts Needed:

2 : Gemini GV U3/6/12 Servo Drives

2 : GEM-VM50 Breakout Modules

2 : 404LXR Linear Slides

1 : DMC-1832 PCI Motion Controller

1 : ICM-2900 Interconnect Module

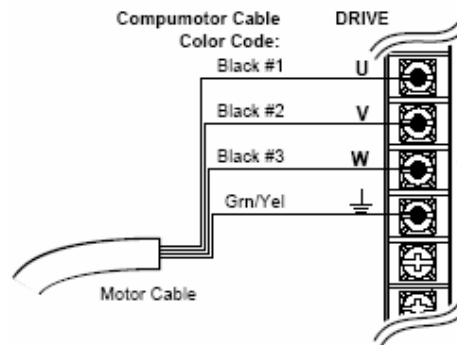
1 : Project Box labeled “Servo Drive Fuse Box”

1 : Necessary Cables (i.e. motor, encoder, limit switch, motion controller, ethernet)

Process:

Step 1 - Connecting the Motor Cable

- 1) Connect the motor cable to the X-axis linear motor, connect the opposite end to the Servo Drive labeled X-axis as shown in the diagram below.
- 2) Do the same for the Y-axis Servo Drive and Y-axis linear motor as well.

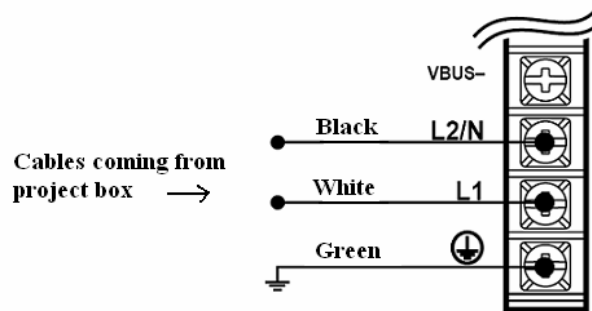


Step 2 - Connecting the Motor Feedback Cable

- 1) Connect the cable labeled “Enc./Hall” to the mating connector on the X-axis motor.
- 2) Connect the opposite end of the cable to the “Motor Feedback” connector on the X-axis drive.
- 3) Loosen the R-clamp located on the bottom side of the Servo Drive, place the exposed braided portion of the motor cable into the clamp and tighten down.
- 4) Repeat for the Y-axis

Step 3 - Connecting AC Power

- 1) Connect the beige X-axis cable coming from the project boxed labeled “Servo Drive Fuse Box” to the power terminals on the X-axis drive in the following fashion:



- 2) Repeat for the Y-axis as well.
- 3) Verify that there is no cable attached to the DRIVE I/O connector.
- 4) Apply power to the drives by plugging in the “Servo Drive Fuse Box” cables into the wall outlet. After the power up sequence, the LED’s should display the following state:

Left LED	Right LED
Red	off

- 5) If this is not the case, go back and check the connections.
- 6) Once finished, disconnect the power.

Step 4 – Configuring the Drive (if only connecting hardware, skip to Step 7)

- 1) Verify that a cable is still not attached to the DRIVE I/O connector.
- 2) Using the 3 meter length black “null modem” cable (it has 9pin serial connector ends) connect one end the computer’s serial port and connect the other end to the X-axis servo drive RS-232 port.
- 3) Apply power to the drive.
- 4) Launch Motion Planner on the computer and do the following (repeat procedure for Y-axis too):

(Directions from Gemini GV Hardware Installation Guide, pg 19)

1. When the product selection dialog appears, select a Gemini GV6 drive and select the COM port to which

the drive is connected.

2. To verify communications with the drive, click the "Terminal" tab on the bottom of the screen to enter terminal mode. Issue the following command:
TREV (transfers the drive's revision level)
Revision level information for your drive should appear on the screen.
To solve communication problems: see RS-232/485 Communications in Chapter 4 – Special Features.
3. In the Editor window, click on the Gemini button at the top of the window to launch the setup wizard.
4. Select "Express Setup", and select "Initialize wizard with factory defaults". (If you wish to keep the existing drive configuration, you should upload it and then initialize from the editor.)
5. Click the "Next" button to proceed with the wizard. Fill in the dialogs as prompted, including choosing a motor series, frame size, and part number. At the end of the wizard, click the "finish" button; this creates the setup code and places it in the Editor window. (See labels on linear motors for model number, this will tell you the parameters you need to enter here)
6. Select File/Save to save the setup code to a file (*.prg) on your hard drive.
7. Select Communications/Download to download the setup code (contents of the Editor window) to the Gemini drive. When the download is complete, choose to "Reset" the drive.
Drive setup is complete. All of the setup parameters (command values) are stored in the Gemini drive's EEPROM and are automatically recalled when you cycle power or reset the drive.
8. Click the "Terminal" tab on the bottom of the screen to enter terminal mode.
9. Issue a DMODE13 command. This configures the drive for autorun mode, in which the motor runs open loop in the clockwise direction at 1 rps. (The motor will not begin turning, though, because you have not yet enabled the drive.)

Step 5 – Verifying Correct System Operations

- 1) Connect the Drive I/O cable to the X-axis servo drive and connect the other end to the GEM-VM50 breakout module.
- 2) Center the linear slides.
- 3) Apply power to the drive if not on already.
- 4) Short pins 1 & 2 on the breakout module to see if the axis moves. (the motion will not be smooth)
- 5) If the system does not behave properly, find and correct the problem before proceeding.
- 6) Repeat for the Y-axis.

Step 6 – Reconfiguring the Drive

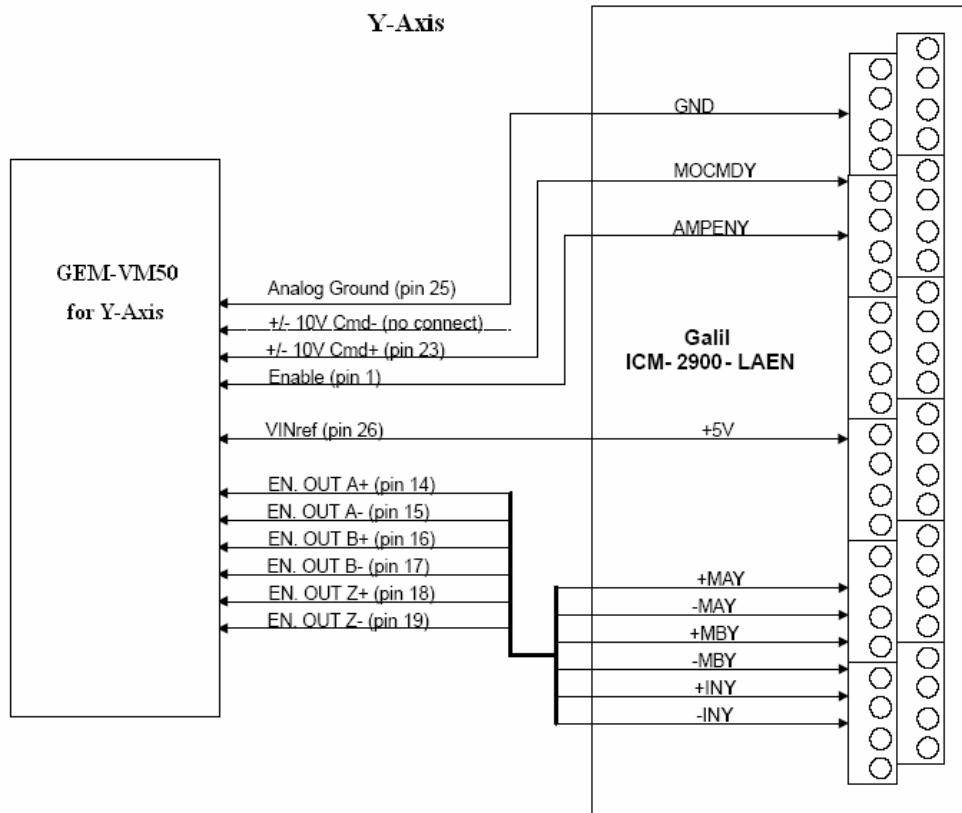
- 1) Connect the null modem cable as was done before.
- 2) Apply power to the drive.
- 3) In Motion Planner, establish communications with the drive:
 - a. Select File/New/Terminal Emulator/OK
 - b. Under Communications/Settings, select the GV.
- 4) Issue the command DMODE2 to configure the drive for Torque Mode.
- 5) Repeat for Y-axis.

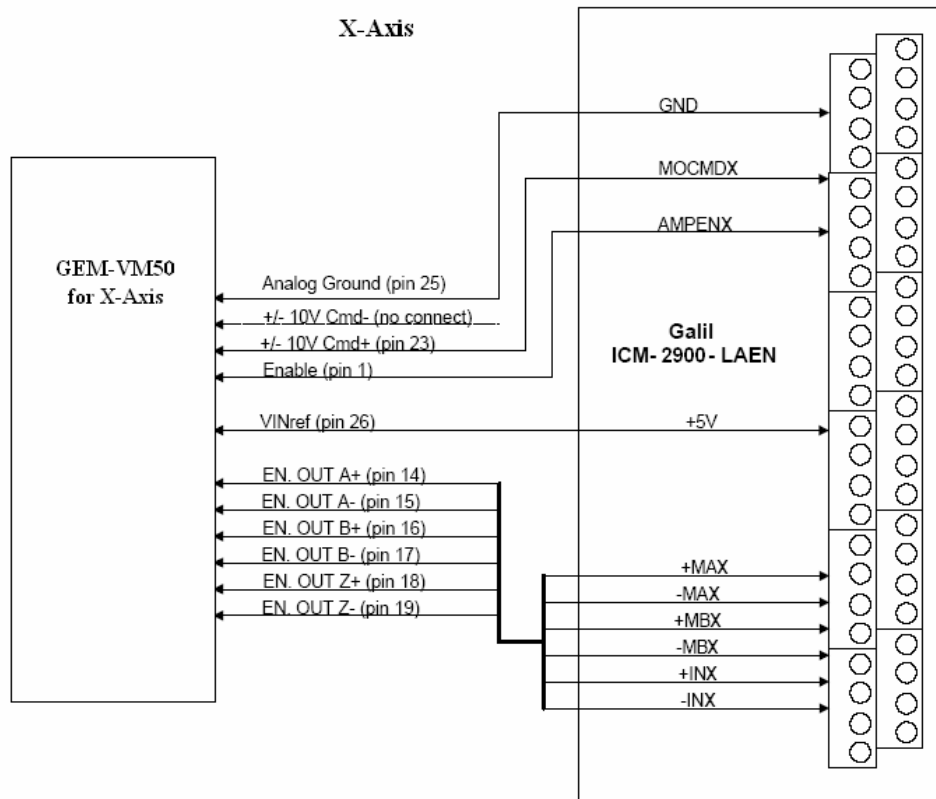
Step 7 – Connecting to Motion Controller

- 1) Disconnect power from the drives.
- 2) Connect a limit switch cable to each of the linear motors and connect the bare ends to the ICM-2900 in the following manner:

Wire Color	Function	Pin (from X-Axis)	Pin (from Y-Axis)
RED	+5 to +24V DC	+12V	+12V
BLUE	Negative Limit	RLSX	RLSY
ORANGE	Positive Limit	FLSX	FLSY
GREEN	Home	HOMEX	HOMEY
BLACK	Ground	GND	GND
Green w/ Yellow Stripe	Shield	No connection	No connection

- 3) Using ethernet cable, strip the ends of the wires and connect each axis to the ICM-2900 as shown in the figures below.





Step 8 – Communicating with Motion Controller

- 1) Install and launch the WSDK software.
- 2) At the bottom of the Servo Design Kit window it should say
Status:Connected with Galil DMC-1832...

If it does not say this, go through the WSDK16 & WSDK32 manual and read how to register the controller under windows.

- 3) Click the “Set-up and Configuration” button.
- 4) On the “Motor State” row, turn the X,Y and Z axis settings to “OFF”.

Verify that the left LED on the Servo Drives is RED and the left LED is off. This indicates the drives are disabled.

- 5) If the motors need to be retuned set the Derivate Constant, Proportional Constant and Integrator Constant rows all to zeros.
- 6) Set the Configure Limit Switch, Configure Home Switch and Configure Latch Input rows to “Active High”.
- 7) Click Edit/Set Parameters and then wait for a window to come up indicating the parameters have been set.

Step 9 – Verify Motion

- 1) First each of the axis must be tested to see if they are working properly. To do this open the WSDK software and click Terminal at the top of the window.
- 2) Make sure that each of the axis are centered physically.
- 3) If the PID gains have been set to zero go back into Set-up and Configuration and set the KP and KD to small numbers, such as KD=2, KP=.2 for each axis otherwise there will be no motion in the system. Then set the controller again as was done in the end of Step 8.
- 4) In the top left area of the Terminal window type in the following (See command reference manual for more info on commands):

SP 299772,299772	then hit enter	(this sets the speed of each axis to about 0.15m/s)
AC 3921012,3921012	then hit enter	(this sets the acceleration to about 0.2g's)
DC 3921012,3921012	then hit enter	(this sets the deceleration to about 0.2g's)
PR 299770,299770	the hit enter	(this sets the travel distant to about 15cm)

Next type in SH to enable to motors

To start the X-axis motion type in BGX (**read note below first)

To start the Y-axis motion type in BGY

*****If anything goes wrong at any time you can type MO for motors off. Whenever you are done testing you should always type in MO to turn the motors off for safety reasons.

If the motors move properly then you may proceed to tuning the motors, otherwise check connections and lookup any errors you may have received. (Use command reference manual to lookup errors)

Step 10 – Verify Motion

- 1) Open a terminal window along with the Set-up and Configuration window.
- 2) Use the right side of the window to create a DMC program file that will make the motor move back and forth in a repetitive motion so that the smoothness of the system can be determined. One example of how to do this is given below:

SP 314063,314063	(Sets both motors to run at about 0.16 m/s, max speed is 1.5m/s)
AC 5881518, 5881518	(Sets the acceleration to 0.3g, max is 2g)
DC 5881518, 5881518	(Sets the deceleration to 0.3g, max is 2g)
PR 603807,603807	(Sets the travel length to 30cm, max is 40cm)
BGX	(Starts the x-axis moving)

AMX (Won't allow the next lines to execute until motion is done)
PR -603807,-603807 (Resets the travel length to go back 30cm)
BGX
AMX
PR 603807,603807
BGX
AMX
PR -603807,-603807
BGX
AMX
MO (Will turn motors off when finished)

This code can be stretched out further to provide more passes and allow more time for observation. Do not max values out until you become more familiar with the system. It is suggested though that you change speeds during the tuning process to see if there are any instabilities in the system with your new PID gains which you will obtain below. Conversion factors for these values are shown on the last page.

- 3) Save the DMC file to the hard drive and then click File/Download to Controller.
- 4) Make sure the x-axis is all the to the right side but not too far so that it activates the limit switch.
- 5) Turn the x-axis on by typing SHX.
- 6) To execute the program type XQ
 - a. If there are any problems at anytime you can type AB and then MO to turn the motors off
- 7) Now you should be able to adjust the gains in the Set-up and Configuration window while the motor is going back and forth. To do this start raising the KD value in short increments say starting from 2 and incrementing by 1 to see the effect on the system. If there begins to be any audible warnings such as loud vibrations from the motor then decrease the current value by about 25% and make sure not to go any higher than this new value.
- 8) Once an acceptable value has been reached (can be changed later if need be) proceed to increase the KP gain, but do this in small increments as it has a greater effect on the system than KD and can easily cause instabilities. Make sure that the KP value stays lower than the KD value since this usually causes the system to become unstable. Raising KP can be done in the same fashion as KD and as a side note, KP is usually no more than half of the KD value.
- 9) Once an acceptable KP has been reached click "Set Parameters" in the Set-up and Configuration window under the edit menu. This will burn the new values into the controller so that the next time the computer is restarted they will not be cleared. Now the KI value may be raised slightly, but be careful since this has a great effect on stability and must be incremented very slowly. Usually KI will be less than 2, so use small increments such as tenths. To numerically see the effect that raising the KI value has on the system type TEX in the terminal window to show the positional error of the system. The error will fluctuate, but raising the KI should help to manage it. (Do not push KI to the limit though) Raising KI will help to push the values towards zero while raising the KD somewhat should help the fluctuation. Read "Manual Tuning Methods" from Galil Application note #3413 to get a better understanding of the gains and their effects:

<http://www.galilmc.com/support/appnotes/optima/note3413.pdf>

- 10) Experimenting with different speeds and accel/decel can help to achieve a good combination of gains for the system. It would be best to tune the motors at the desired speed or speed range you would like to run at. It is almost impossible to achieve the most optimal gains for the system so

take your time and experiment with the system to achieve the best performance you can. When the gains are set the way you like make sure to burn the new values into the controller. Then repeat this procedure for the Y-axis.

Distance

1 cm = 19984.77 (max travel length = 40cm)

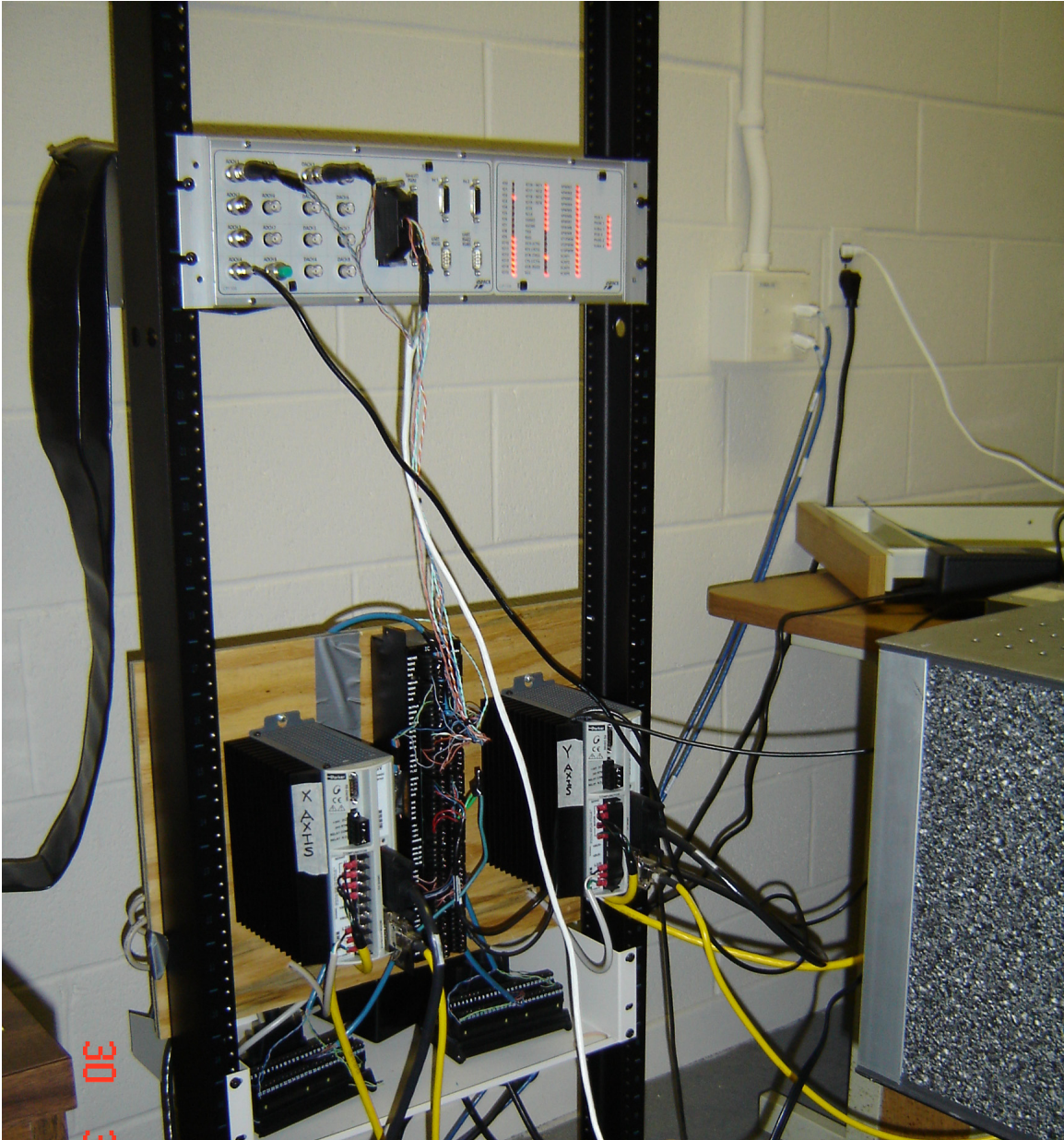
Speed

1 m/s = 1998477 (max speed = 1.5 m/s)

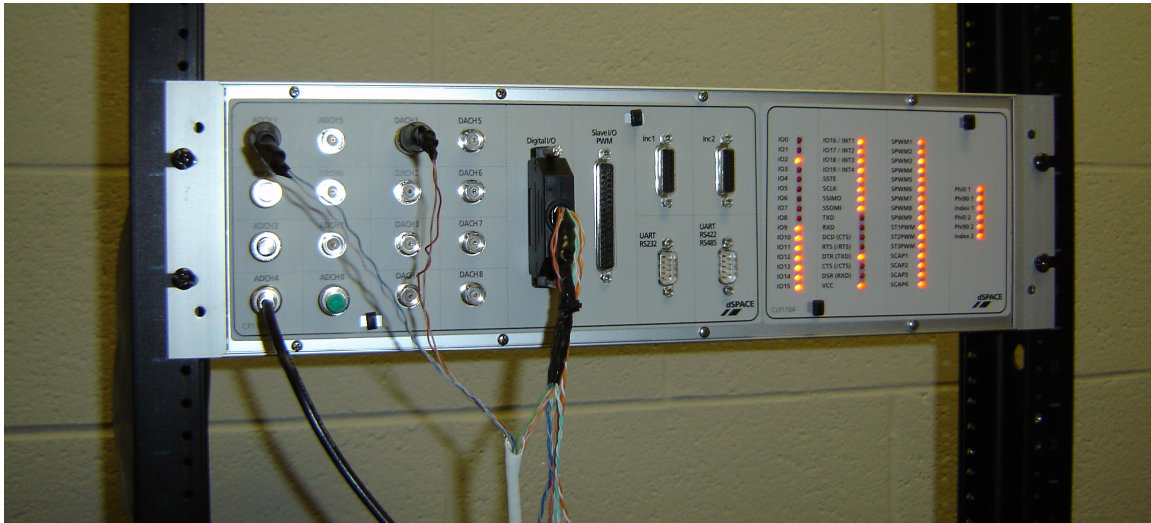
Acceleration and Deceleration

1 g = 19605059 (max repetitive accel/decel = 2 g)

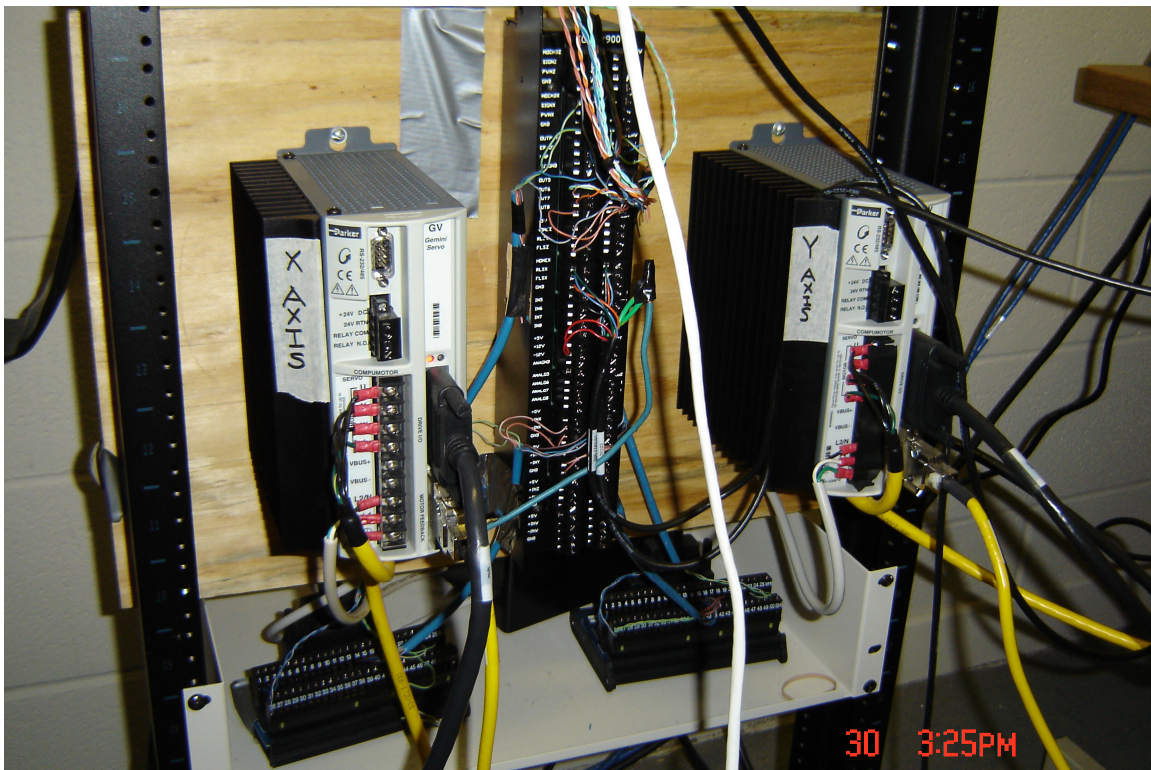
14.2 Equipment Connection Images



This is the instrument rack that contains the servo drives, motion controller breakout box, servo drive breakout boxes, and the Dspace control panel.



Enlarged view of the Dspace control panel. A/D and D/A BNC connectors are located on the left while the large parallel cable is for digital inputs and outputs. The LED's on the right indicate when the digital I/O's are active.



X and Y axis servo drives are located on right and left with the breakout modules located directly beneath them. Motion controller breakout module is located in the center.

14.3 Laser Images and Procedure



The 300W IPG Single Mode, CW Ytterbium Fiber laser. Below is the handheld unit used to control it.



Laser Experiment Operating Procedures:

The laser operator is the **ONLY** person who can ensure the safety of everyone in and outside the lab. The laser operator should follow **ALL** the procedures below so that no one is harmed.

Safety Setup:

1. Put up safety signs on doors and deadbolt all entrances.
2. Before turning laser on: Make sure the following bits on the D-Space control panel are cleared (not lighted):
IO0, IO1, & IO3 to IO8
3. Turn key on laser and **wait 3 minutes** before turning on power supply (green start button)
4. Make sure “Modulation” and “External Control” settings on the handheld unit are set to “Disabled.”

Laser Setup:

5. Upload any necessary D-space and Motor Control programs to respective units.
6. Set up work-pieces, test samples, and necessary equipment in work area.
7. Make sure there are no flammable materials near work area.
8. Make sure **EVERYONE** in the room is wearing eye protection and make sure everyone is clear of the work area. Say:
 - a. “Glasses ON!”
 - b. “Clear work area!”
9. **FIRST** Enable the “Modulation,” and **THEN** Enable “External Control” via the handheld unit. Say:
 - a. “Modulation and External Control enabled!”

Experimentation:

10. Conduct a test run without use of laser to make sure experiment is set up properly.
11. Before anyone is allowed in the work area, make sure bits: IO0, IO1, & IO3 to IO8 are cleared.
12. Once those bits are cleared work area is now accessible. Say:
 - a. “Work area is now safe.”
13. Make any necessary adjustments and then clear everyone out of work area. Say:
 - a. “Glasses ON!”
 - b. “Clear work area!”
14. Conduct actual experiment.
15. Repeat steps 10 through 13 until all experiments are completed

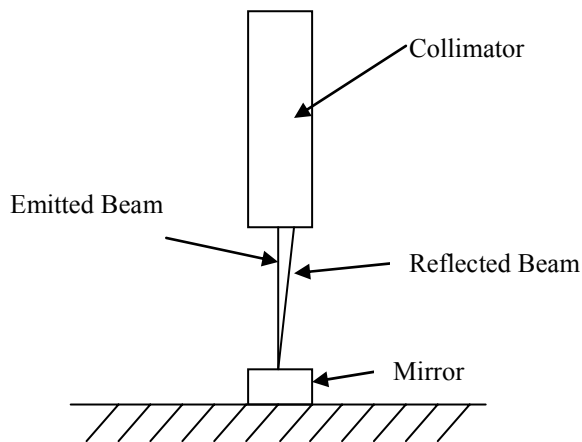
Shut Down:

16. Once ALL experiments are done, make sure bits: IO0, IO1, & IO3 to IO8 are cleared.
17. **FIRST** Disable the “External Control,” and **THEN** Disable “Modulation” via the handheld unit. Say:
 - a. “Modulation and External Control disabled!”
18. Then turn laser off by turning the key on the laser.

* These procedures **MUST** be followed even when turning on **ONLY** the guide beam.

14.4 Laser Alignment Procedure

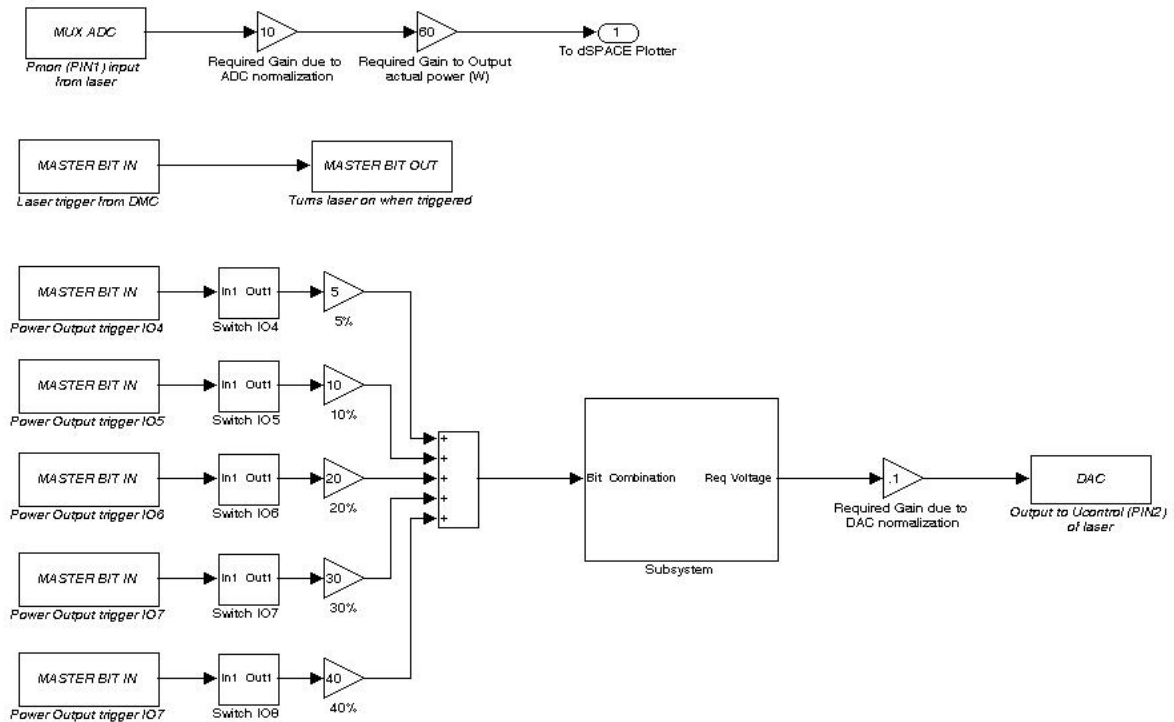
The laser alignment is a critical issue that should not be overlooked. It is vital that the laser be aligned properly with the workpiece and optics to be sure that the laser impact is under optimum conditions. When discussing the laser alignment, we are talking about the alignment of the collimator. Since the laser is delivered through a fiber, it is necessary to align the collimator. First, the laser should be aligned with the optic table. This table serves as a reference for everything else. To align the collimator with the table, a mirror is placed on the table and used to reflect the guide beam that comes from the collimator. Using a piece of paper to see the reflection of the guide beam, the collimator can be adjusted until the reflected beam is collinear with the emitted beam.



The collimator must also be aligned with the platform that sits atop the linear motors. This is difficult because the platform moves and must be aligned at all possible positions. This is done similarly to the procedure to align the collimator to the optical table. A

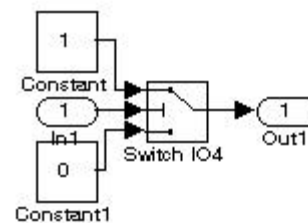
mirror is used to reflect the guide beam and then adjustments are made to align the reflected and emitted beam. Finally the collimator should be aligned with the beam expander and focusing lens. The mirror is placed on top of the beam expander and the beam expander is adjusted until the beam reflects back to the collimator. A target of some sort is used to aim the beam through the center of the expander. The target is placed on top of the expander and the expander moved horizontally until the beam strikes the center of the target. The focusing lens now should be aligned. A target roughly the same diameter of the lens is used and the lens holder is moved back and forth until the beam out of the expander is centered on the target. A collar of some sort is placed on the lens holder post to set the spot because the next step will involve rotating the lens and putting a collar on the holder post will give a reference point. The focusing lens is rotated back and forth. A spot is formed on the platform that moves back and forth with the lens. The lens is rotated so the spot is aligned with the beam on the platform.

14.5 Simulink Models

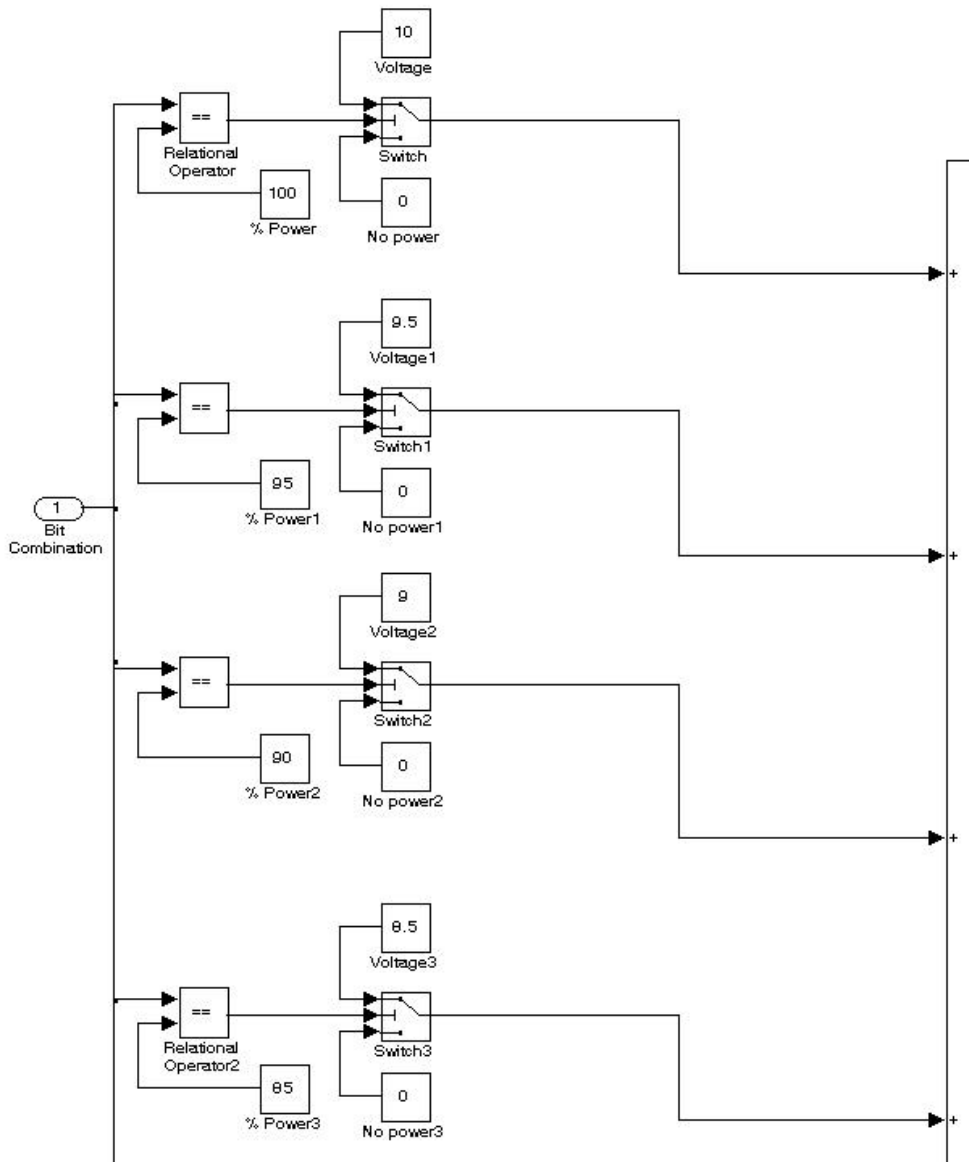


This was the first Simulink model (*modified_multi_modulation.mdl*) created to produce different powers depending on the combination of bits sent from the motion controller.

The switches as below just sent a value of 1 to the appropriate gain.



The gains were then summed and sent the subsystem (partially shown below) where depending on the combinations of bits that were sent, would produce the desired voltage being sent to the laser's power control input.



The table below shows the proper bits to set corresponding to the desired power.

Power Settings (for modified_multi-modulation.mdl)

IO3 = 2.5% (Not currently used)

IO4 = 5%

IO5 = 10%

IO6 = 20%

IO7 = 30%

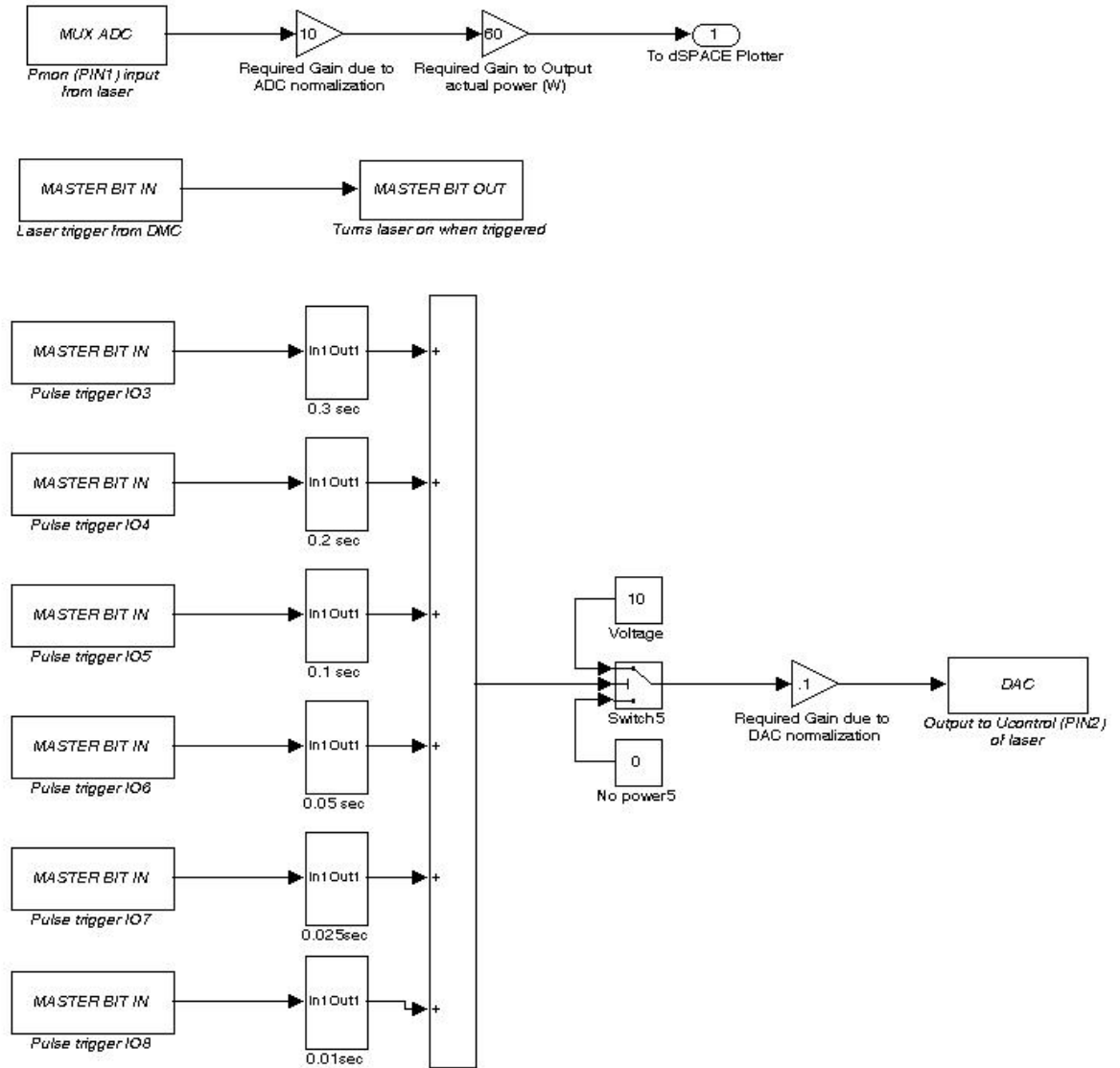
IO8 = 40%

Desired Power	Dspace LED's	DMC Commands
5 %	IO4	SB 4
10 %	IO5	SB 5
15 %	IO4+IO5	SB 4 + SB 5
20 %	IO6	SB 6
25 %	IO4+IO6	SB 4 + SB 6
30 %	IO7	SB 7
35 %	IO4+IO7	SB 4 + SB 7
40 %	IO8	SB 8
45 %	IO4+IO8	SB 4 + SB 8
50 %	IO5+IO8	SB 5 + SB 8
55 %	IO4+IO5+IO8	SB 4 + SB 5 + SB 8
60 %	IO6+IO8	SB 6 + SB 8
65 %	IO4+IO6+IO8	SB 4 + SB 6 + SB 8
70 %	IO7+IO8	SB 7 + SB 8
75 %	IO4+IO7+IO8	SB 4 + SB 7 + SB 8
80 %	IO5+IO7+IO8	SB 5 + SB 7 + SB 8
85 %	IO4+IO5+IO7+IO8	SB 4 + SB 5 + SB 7 + SB 8
90 %	IO6+IO7+IO8	SB 6 + SB 7 + SB 8
95 %	IO4+IO6+IO7+IO8	SB 4 + SB 6 + SB 7 + SB 8
100 %	IO5+IO6+IO7+IO8	SB 5 + SB 6 + SB 7 + SB 8

SB1 -> turns laser on

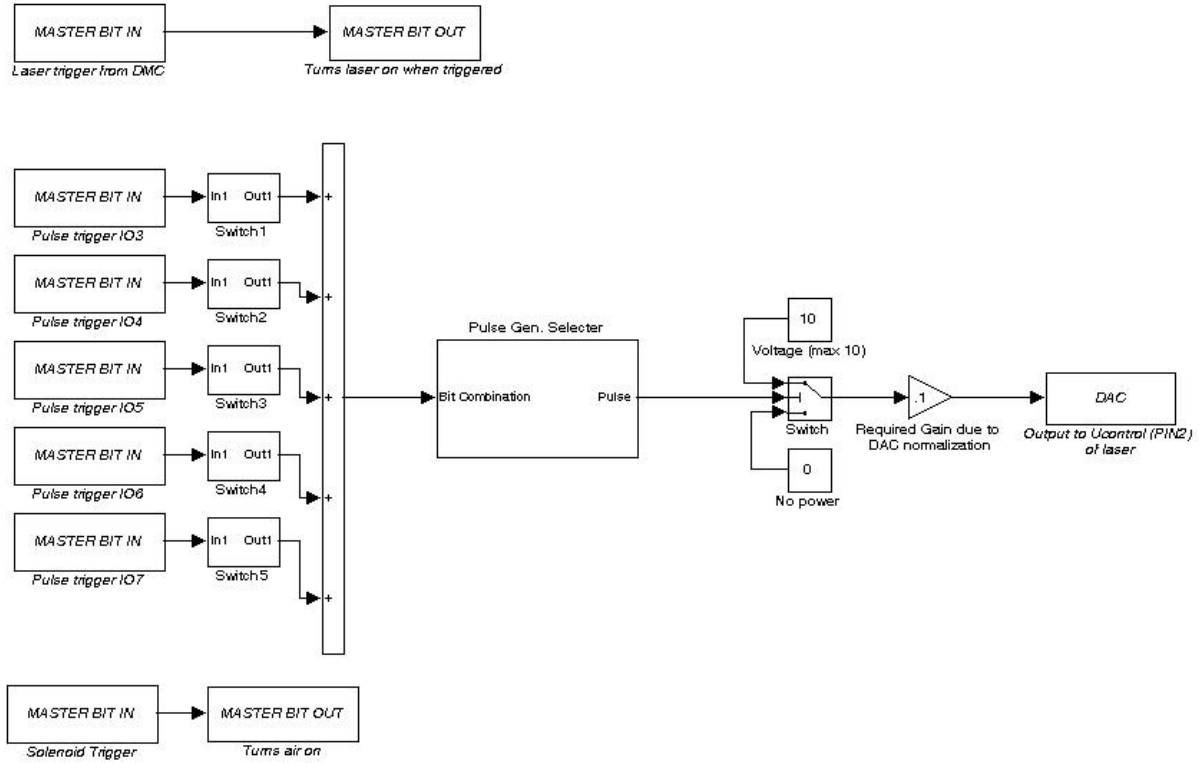
SB2 -> turns guide laser on

The next Simulink (jason_power_schemes.mdl) model was the first attempt at pulsing

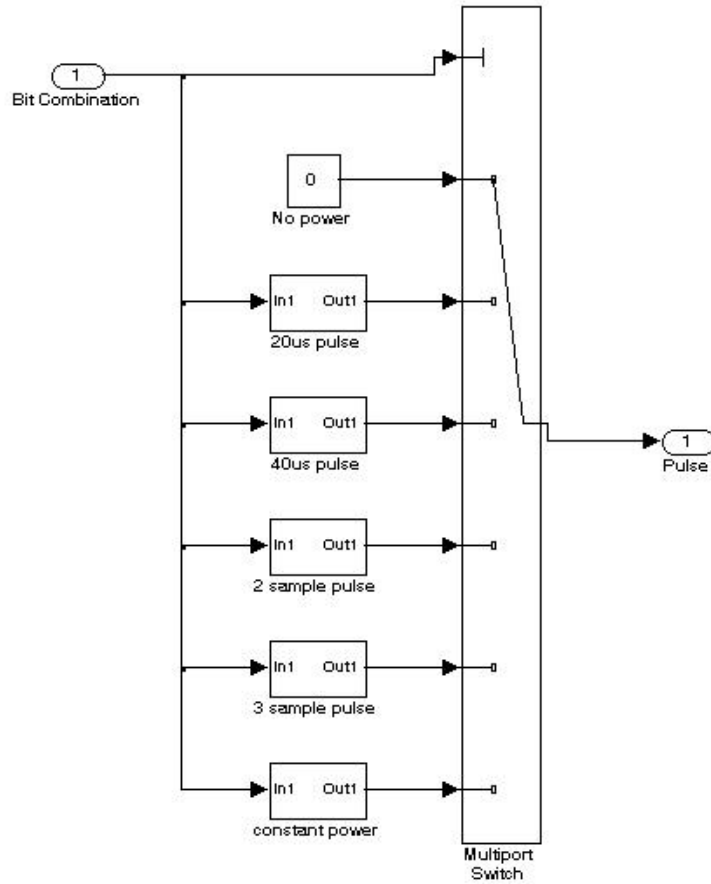


The subsystems just before the summer are simply switches which have the desired repetitive pulsing signal for an output.

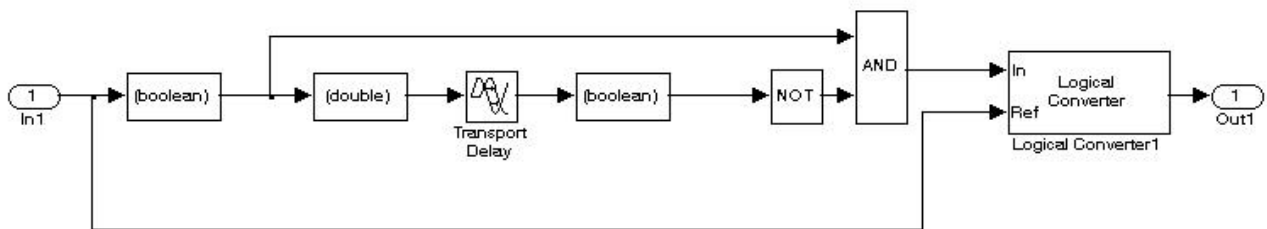
The model below (single_pulsing_air_new.mdl) is the final model that was used to produce the microsecond pulses.



The switches before the summer simply output an integer corresponding to the position on the multiport switch in the next image. For example when bit 3 was set it would output a 1 and would correspond to the 20 μ s block on the multiport switch.



The subsystems connected to the multiport switch were actually modified edge detectors.



The desired single pulse would then be sent to the laser at full power.

14.6 Example DMC Script

```
CB1
CB3
CB4
CB5
CB6
CB7
CB8
REM ##### 20 MICROSECOND PULSING #####
COUNT1=0

REM TURN ON AIR
AI -5
SB8

#SPOT
REM BEGIN MOVE AND PULSE
AI -5 //This waits for the external input button to be depressed
CAS
VMXY
VS 10063,10063 //Sets Speed
VD 5060505,5060505 //Sets Deceleration
VA 5060505,5060505 //Sets Acceleration
VP 0,5085 //Sets x and y movement distance
VE
BGS //Begins Sequence
AMS //After sequence is complete
SB1 //Enables the laser
COUNT=0

AT 0
AT 500 //Waits 0.5seconds

#PULSE
REM SETTING BIT 3 WILL CREATE 20US PULSES FROM DSPACE
SB3
AT 0
REM ALLOWS FOR CONSERVATIVE 1MICROSECOND TIME FOR PULSE TO COMPLETE
AT 1
CB3
COUNT=COUNT+1
JP #PULSE, COUNT<1 //Count to produce multiple or single shot

CB1
MG "SPOT COMPLETE"
COUNT1=COUNT1+1

REM ##### MAKE SURE TO CHANGE LOOPING NUMBER IF NEEDED#####
JP #SPOT,COUNT1<10 //Count for total number of locations
CB8
MG "PROGRAM COMPLETE"
SB2
EN
```

This example program will create a 20 μ s pulse if used with the `single_pulsing_air_new` model.

14.7 Microscope Operation & Details

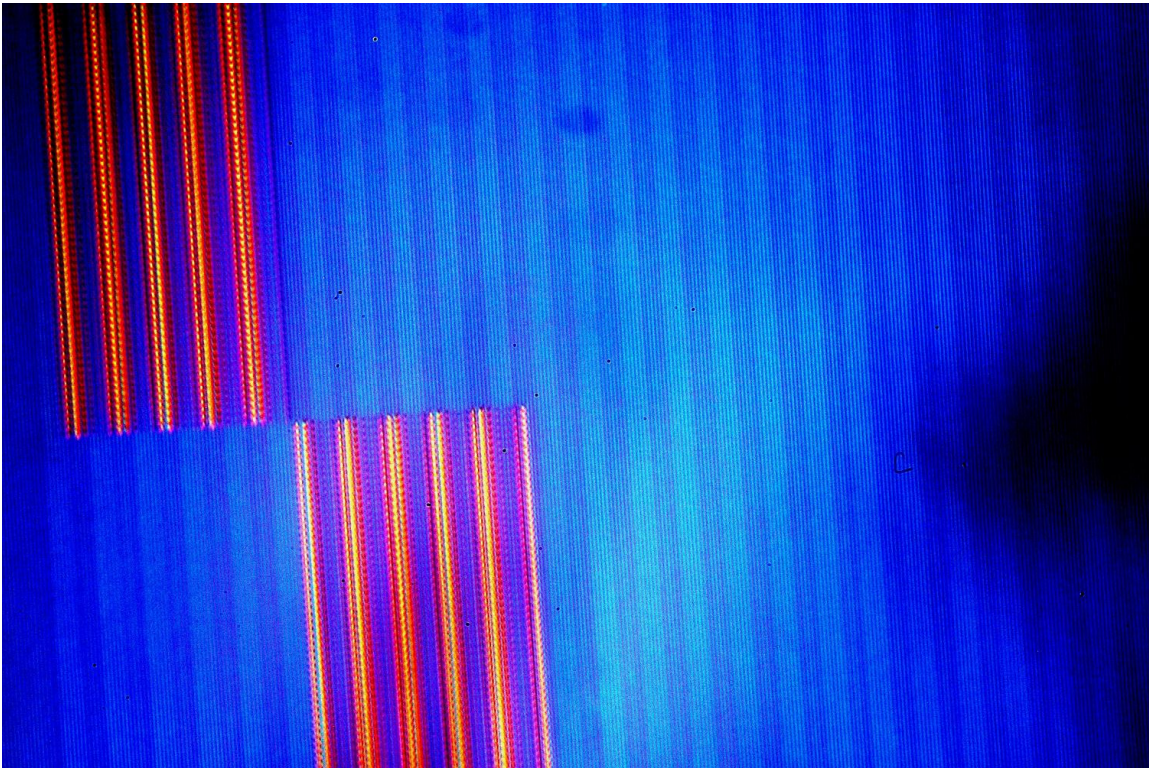
Specimens were examined using an inverted Zeiss microscope. The microscope contained 2.5x, 8x, 16x, 40x, and 80x objectives. All but the 2.5x objective contained DIC filters which would alter the colors of the area being viewed depending on the height of the surface.



Pictures at 3008 X 1200 pixels were taken with a Nikon D70 digital camera using the lower adapter of the microscope. The microscope camera shutter was controlled using the device below(left). The device was powered on and righthand knob was rotated to 120 and the exposure button was then depressed to open the shutter for several minutes. The power supply on the bottom right was turned on to 12V to supply the correct voltage to the microscope lamp.



The microscope was calibrated by examining a CD under the 16x objective. Knowing that the spacing between a CD's tracks is $1.6\mu\text{m}$ an image was taken of the CD tracks and



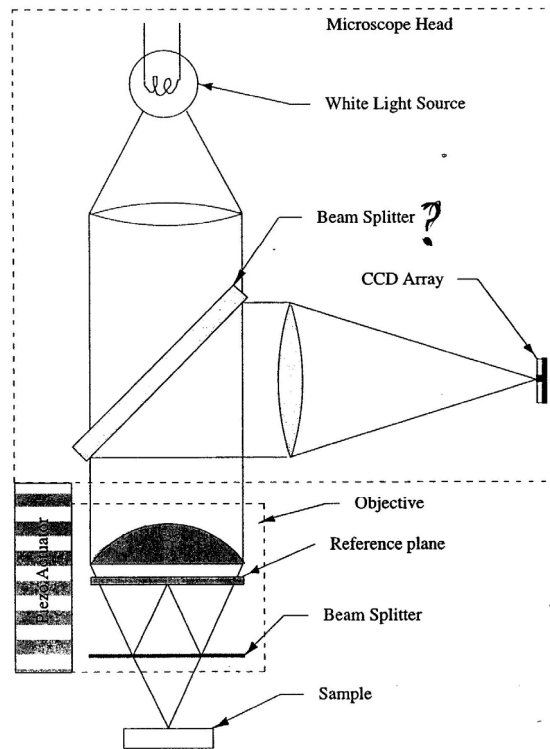
was then enhanced to make the tracks more visible. The image was then input into the Motic Camera Software package where the measurement tools were calibrated by this known spacing of $1.6\mu\text{m}$. The other objectives were then calibrate using the conversion factor corresponding to the difference in magnification of the lenses.

14.8 Zygo NewView 5000 Interferometric Microscope Details



Zygo NewView 5000 Interferometric Microscope

- Noncontact 3D Profilometry
- Vertical: 0.1 nm resolution/ 5 mm Range
- Horizontal: 0.5 μm resolution/ 50 mm Range



Schematic of the Interferometric Microscope

Laboratory Notebook for *Metrology in Precision Manufacturing*

1. Level the sample stage using the tip/tilt knobs
2. Raise the coarse focus adjustment and retract motorized adjustment if necessary to clear the sample and objective.
3. Place the sample on the stage and install the objective
4. Place the "Focus" knob in the focus (in) position
5. Adjust the light level by pressing the F5 function key on the computer keyboard.
6. Adjust the equal path ring until the image on the fringe monitor has a focused edge.
7. Adjust the coarse (manual) focus wheel to slightly above the recommended distance for that particular objective as shown on the chart attached to the microscope just above the objective.
8. Using the joystick control, adjust lower the microscope head until the surface comes into focus. Take care not to go past the focus and crash the objective into the part. The light level may have to be adjusted again several times with the F5 function key.
9. Adjust the tip/tilt knobs to minimize the number of fringes on the fringe monitor in the case of flat samples. In the case of spherical samples, center the interference pattern. The focus will have to repeatedly be adjusted during this time at a slow speed setting to keep the fringes on the screen.

II. Taking a Measurement

1. Select the objective installed on the microscope from the box in the upper right hand corner of the screen.
2. Open the "Measurement Controls" window and select the desired scan length and the zoom magnification set on the microscope. This scan range determines the range of motion of the piezo actuator and the maximum height that can be measured. Enter the name of the part being measured. Close the window.
3. Open the "Analyze Controls" window and select the desired filter options. Close the window.
4. Press the "Measure" button and wait for the microscope to complete the scan. Disrupting the machine while it is taking data can have a deleterious effect on the measurement.
5. Save the data or print it using the "Zygo" button in the desired widow.

Instructions for obtaining measurements on the Zygo NewView 5000 (Sohn, 2005)

14.9 Talysurf Stylus Profilometer Details



14.9.1 Form Talysurf Stylus Profilometer

- Contact 2D Profilometry
- 10mg stylus load
- Vertical: 5 nm resolution/ 6 mm Range
- Horizontal: 0.5 μm resolution/ 120 mm Range

Talysurf operating instructions

The Talysurf system consists of the specimen platform and height-positioning column, the horizontal traverse unit, the console, and the recorder. Note that the Talysurf's measurement unit is mounted on an air table to minimize vibration of the stylus and specimen.

The operation of the Talysurf can be described as follows. The Traverse Unit, mounted on the height-positioning column, provides the horizontal translation of the measurement probe, or stylus. The diamond-tipped stylus is traversed along a line on the surface of the specimen. The traverse speed is determined by the horizontal scale magnification selected via the selector knob on the front of the Traverse Unit. Horizontal magnification for this unit ranges from 2X to 100X. (At the 5X magnification, the traverse speed is 1 millimeter per second.) The horizontal range of travel for this unit is 120 millimeters or 4.8 inches.

The geometry of the stylus has a major impact on the measured profile. A large radius stylus can act as a low-pass filter, not detecting high-frequency valleys (see Figure 15). Measurements with a small radius stylus may suffer from measurement force distortions (see Figure 16). (Remember the significance of the probing or measurement force: small forces exerted over very small areas can result in pressures sufficient to cause appreciable distortion of the true surface profile.)

In this case, the stylus has a 6.5 micrometer (or 260 microinch) radius. The stylus lever arm deflects up or down with the topography of the specimen's surface (see Figure 17). A spring keeps the stylus in contact with the specimen's surface. The probing force for this unit is 100 milligrams force, or one thousandth of a Newton.

The vertical range of this stylus is .175 millimeters or seven thousandths of an inch. Measurements can be made with the stylus as shown in Figure 17, or with the stylus equipped with a skid. The skid rides along the surface of the part so that displacements of the stylus are made relative to the basic surface shape. In our measurements today, we will not use the skid.

An LVDT converts these vertical displacements of the stylus arm to signal voltages. These voltages are amplified according to the vertical magnification selected. For this unit, the vertical magnification range is 100X to 200,000X. Electronic filtering can be selected to separate roughness and waviness components. This voltage signal may be used to generate a trace of the surface profile as represented by the displacements of a recorder pen. From this trace, surface finish parameters, such as "Ra" and "PV", can be graphically determined. Signal voltages may also be processed to automatically determine these parameters. However, on this particular unit, only "Ra" determination is available.

To prepare the system for making measurements, power up the system by pressing the mains pushbutton. Allow time for electronic stabilization. Select inches or millimeters with the measurement unit switch beside the display. Remove the skid from the stylus arm. Ensure that the skid switch is set to “no skid”.

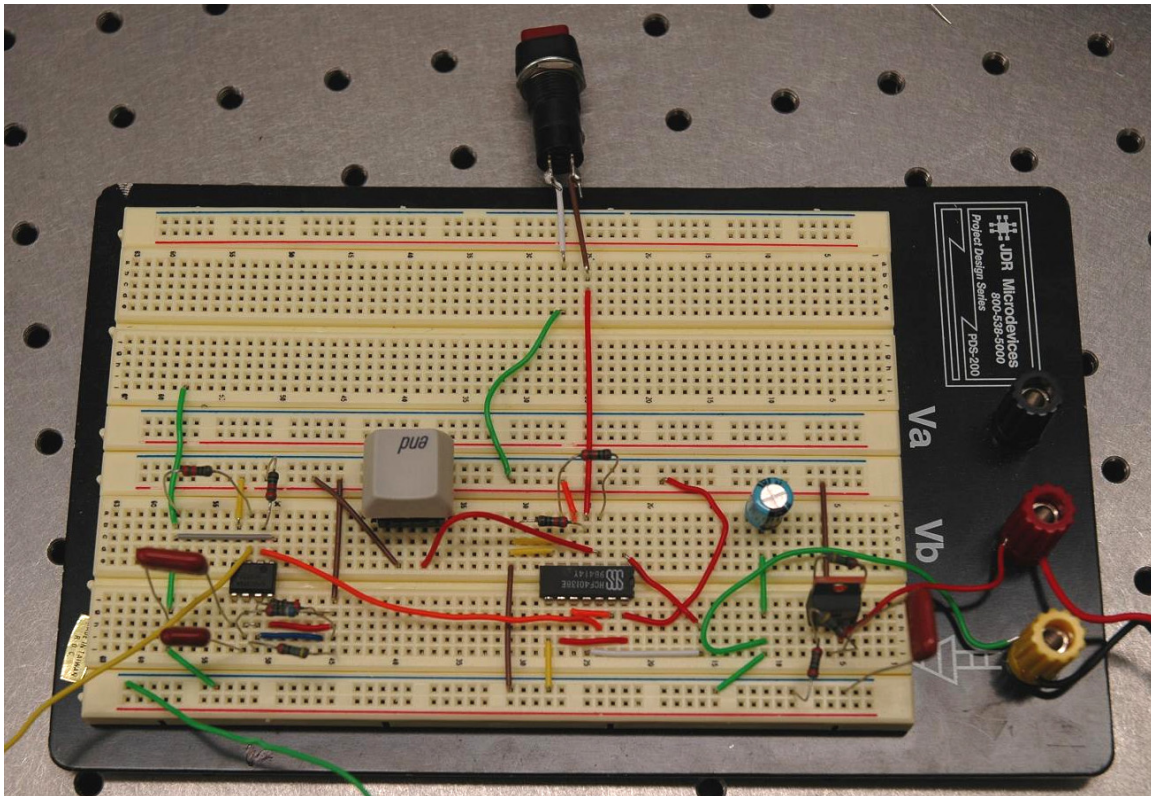
Vertical positioning via the motor-driven column is accomplished by pushing the vertical traverse toggle switch to raise the stylus, and pulling the switch to lower the stylus. The vertical traverse has a two speed motor: after initially jogging at the lower speed, it will shift to the higher speed after 5 seconds. The vertical drive motor will automatically shut off when the stylus engages the specimen. Try to be moving at the low speed when contact with the surface is made. The unit can also be vertically positioned via the manual adjust knob at the top of the column. Counterclockwise rotation results in upward movement and clockwise rotation results in downward movement.

Bring the stylus down to contact the specimen’s surface. The amount of stylus arm deflection is displayed by the console’s pickup position indicator. The “+” end of the pick-up position indicator designates the direction of greater upward displacement of the stylus. The “-” end

(Sohn, 2005)

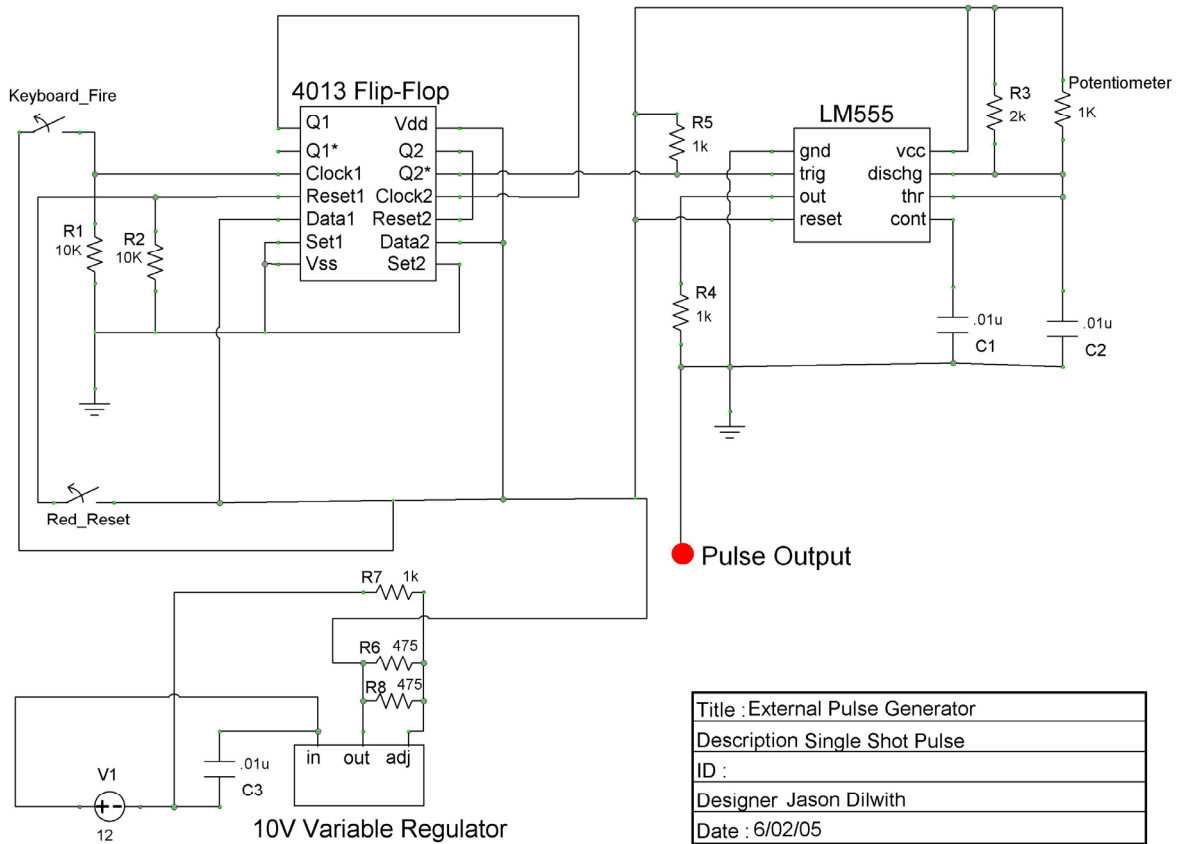
14.10 External Pulse Generator

To generate pulses smaller than $20\mu\text{s}$ the external pulse generating circuit shown below was constructed.



The circuit consists of a LM555 Timer, LM317 adjustable voltage regulator, 4013 Dual D-type flip-flop, 2 pushbuttons, and various resistors and capacitors.

The circuit schematic for the single shot pulse generator that was constructed is shown below.



Title : External Pulse Generator
Description Single Shot Pulse
ID :
Designer Jason Dilwith
Date : 6/02/05

Note: Grounding Symbols Denote
Negative Side of Power Supply